DESIGN OF A TI-6AL-4V HEAT EXCHANGER USING DIMENSIONAL ANALYSIS FOR USE IN AERONAUTICAL TURBOSHAFT ENGINES

by

Paul Michiel Bester

Dissertation submitted in fulfilment of the requirements for the degree

Master of Engineering

in

Mechanical Engineering

Department of Mechanical and Mechatronics Engineering

Faculty of Engineering and Information Technology

Central University of Technology, Free State, Bloemfontein

Supervisor: Dr. F.C. Aggenbacht, D.Tech

Co-supervisor: Mr. Imdaadulah Adam, M.Eng

March 2025

© Central University of Technology, Free State

DECLARATION WITH REGARD TO

INDEPENDENT WORK

I, Paul Michiel Bester, identity number _____ and student number _____, do hereby declare that this research project submitted to Central University of Technology, Free State for the degree Master of Engineering in Mechanical Engineering (M_ENGM), is my own independent work; and complies with the Code of Academic Integrity, as well as other relevant policies, procedures, rules and regulations of Central University of Technology, Free State; and has not been submitted before to any institution by myself of any other person in fulfilment (or partial fulfilment) of the requirements for the attainment of any qualification.

21/04/2025

_____ _____

SIGNATURE OF STUDENT **DATE**

© Central University of Technology, Free State

Acknowledgements

I would like start by thanking the friends and family who supported me through the trials and tribulations involved in getting this project to its completion. Without their support and encouragement, it is unlikely that it would ever have come to fruition.

Secondly, I would like to express my gratitude to my primary supervisor Dr. F.C. Aggenbacht for taking me as a student when no other supervisors were available, and I would also like to specifically thank my co-supervisor Mr. Imdaadulah Adam for his continued support and technical expertise in the field of additive manufacturing.

Additionally, I would like to thank and highlight the contributions made by the Centre for Rapid Prototyping and Manufacturing (CRPM) and the Product Development Technology Station (PDTS) in Bloemfontein throughout the development of the project.

© Central University of Technology, Free State

Abstract

While post-compression intercooling is a commonly utilised method to increase or optimise the performance of traditional turbocharged internal combustion engine layouts, there exists a potential in installing similar modifications in aeronautical turboshaft engines. The rise of additive manufacturing (AM) techniques now offers the potential for lighter and more compact heat exchangers to be designed and manufactured. To this end, a theoretical intercooler system was designed to cool the charge air supplied by the compressor stages of a turboshaft engine to increase the performance of the engine. With cooler air supplied by the compressor stage theoretically having the capacity to reduce the amount of work required by the compressor stages as well as benefiting the containment effects inside the combustor unit.

A benchmark engine was selected and characterised by a simple Brayton gas cycle, which indicated that there was an overall temperature increase of 234.710 °C across the compression process due to the heat of compression. Using the Kays and London method for a full-sized multi-pass heat exchanger, a heat exchanger was successfully designed, which would fulfil all the requirements to evaluate the feasibility of the concept. A test piece was then extracted from the design and successfully manufactured at half scale using Ti-6Al-4V titanium alloy. The theoretical intercooler unit consisting of two full-size multi-flow heat exchangers was able to cool air supplied at a mass flow rate of 1.638 kg/s by an estimated 28.542 °C. Dynamic similarity constraints obtained via dimensional analysis techniques were then successfully applied to determine the experimental testing conditions required to verify the full-scale design. An experimental test bench was designed and fabricated to simulate the required testing conditions to attain dynamic similarity. A series of six tests, consisting of eight readings each, were performed over a time span of two weeks, where exact measurements were taken of the heat transfer across the test piece heat exchanger. The results recorded from the experimental testing phase of the project indicated that the process whereby a portion was extracted from a heat exchanger and verified using dynamic similarity was not only viable but yielded much better results than expected. The experimental results showed a substantial correspondence to the theoretically expected calculations. The outcome of this research aims to clarify the suitability of a heat exchanger manufactured using AM techniques for use in aeronautical turboshaft engines.

© Central University of Technology, Free State

Publications emanating from…

P. M. Bester, F. C. Aggenbacht, and I. Ada. *"Design and additive manufacturing of TI-6AL-4V test-piece for use in aeronautical turboshaft engine heat exchanger,"* presented at 2025 RAPDASA-RobMech-PRASA-AMI Conference, MATEC Web of Conferences 406, 07005 (2024). eISSN: 2261-236X. https://doi.org/10.1051/matecconf/202440601002

© Central University of Technology, Free State

TABLE OF CONTENTS

© Central University of Technology, Free State

© Central University of Technology, Free State

© Central University of Technology, Free State

List of figures

© Central University of Technology, Free State

© Central University of Technology, Free State

© Central University of Technology, Free State

List of tables

© Central University of Technology, Free State

List of Equations

© Central University of Technology, Free State

© Central University of Technology, Free State

© Central University of Technology, Free State

List of symbols

A	Cross-sectional area	m^2
A_f	Free flow area	m^2
A_{fr}	Frontal area	m^2
$A_{transfer}$	Heat transfer area	m^2
A_f/A	Fin area to total area ratio	ratio
b	Plate spacing	mm
B	Transfer area to volume ratio	ratio
C_{max}	Maximum heat capacity rate	W/K
C_{min}	Minimum heat capacity rate	W/K
c_p	Specific heat capacity	kJ/kgK
C_r	Heat capacity rate ratio	ratio
C	Heat capacity rate	W/K
D_h	Hydraulic diameter	m
f	Air to fuel-ratio	ratio
g_c	Gravitational constant	n/a
G	Mass velocity	kg/m^2s
h	Heat transfer coefficient	W/m^2K
j	Colburn factor	n/a
K_c	Contraction pressure loss coefficient	n/a
K_e	Expansion pressure loss coefficient	n/a
l_f	Fin length	m
l_s	Strip length	m
L_1	HX hot side passage length	m
L_2	HX cold side passage length	m
L_3	HX tile width	m
$\dot{m}_a$	Mass flow rate of air	Kg/s
m	Fin parameter	n/a
M	Mach number	n/a
η_b	Combustor efficiency	%
η_f	Fin efficiency	%
η_{ft}	Free power turbine efficiency	%

© Central University of Technology, Free State

η_{gt}	High power turbine efficiency	%
η_m	Mechanical efficiency	%
η_o	Overall fin efficiency	%
N_P	Number of parallel passages	n/a
NTU	Number of heat transfer units	n/a
P	Pressure	Pa
P_{rotor}	Shaft power output	W
p	Wetted perimeter	m
Pr	Prandtl Number	n/a
$\dot{q}$	Heat transfer rate	W
Q_R	Fuel calorific value	kJ/kg
r_h	Hydraulic radius	m
R_w	Wall resistance	m
R	Universal gas constant	kJ/kgK
Re	Reynolds number	n/a
SF	Scale factor constant	n/a
St	Stanton Number	n/a
T_m	Mean temperature	K or C
T	Temperature	K or C
UA	Overall thermal conductance	W/K
V_p	Passage volume	m^3
y	Specific heat ratio	ratio
δ_{fin}	Fin thickness	m
δ	Wall thickness	m
ε	Heat exchanger effectiveness	n/a
μ	Fluid viscosity	Pa * s
ρ	Density	kg/m^3
σ	Heat transfer ratio	ratio
$\dot{VOL}$	Volumetric flow rate	m^3

© Central University of Technology, Free State

List of abbreviations

AM	Additive Manufacturing
CRPM	Centre for Rapid Prototyping and Manufacturing
CFD	Computational Fluid Dynamics
DA	Dimensional Analysis
DS	Dynamic Similarity
DMLS	Direct Metal Laser Sintering
EOS	Electro-Optical Systems GmbH
EBM	Electron Beam Melting
ε -NTU	Effectiveness Number of Transfer Units
FEA	Finite Element Analysis
FPT	Free Power Turbine
HPT	High Power Turbine
HP	High Pressure
ICAO	International Civil Aviation Organization
ISO	International Organization for Standardization
LPBF	Laser Bed Powder Fusion
LP	Low Pressure
NTU	Number of Transfer Units
OEM	Original Equipment Manufacturer
PDTS	Product Development Technology Station
SLS	Selective Laser Sintering
SFC	Specific Fuel Consumption

© Central University of Technology, Free State

CHAPTER 1

Introduction

This chapter aims to provide the background and supporting information to communicate the purpose of the study.

There has been a notable trend in the aeronautical industry to implement more efficient forms of propulsion with the objective of reducing pollution, the emission of greenhouse gases, and the reliance on traditional fossil fuels [1], with promising sources aiming to use renewable fuel sources such as biofuel or biogas to generate power [2]. However, these technologies are still in their infancy and are not yet applied on a commercial scale. Most aircraft gas turbines continue to rely on conventional fossil fuels, which are expected to remain a critical part of the aeronautical industry until these new technologies have been further developed. Therefore, research into improving the performance of existing engines is of great importance, with a potential method to reach this goal concerning the development and application of post-compression intercooling systems in aeronautical turboshaft engines. This approach aims to reduce the temperature of charge air supplied via the compressor stages of a turboshaft engine, which has the benefit of improving the density of the air before it is supplied to the combustion chamber [3]. A reduction in the temperature of charge air is theorized to lead to an increase in the density of the charge air, as is the case in traditional automobile engines fitted with intercooler turbochargers [4]. Despite conventionally manufactured heat exchangers already having an substantial presence in the fields of aeronautics, the rapid advancement of additive manufacturing (AM) techniques, such as laser bed powder fusion (LPBF), now presents the opportunity to create metallic components with complex geometries, which leads to the potential of processing materials such as Ti-6Al-4V (Ti64) using LPBF to create effective yet lightweight heat exchangers [5]. The introduction of these new AM techniques into conventional heat exchanger design processes may lead to beneficial developments.

© Central University of Technology, Free State

1.1 Problem statement

Elevated temperatures in turboshaft engines caused by the rapid compression of atmospheric air during the compression stage of the engine cycle result in hotter air being used for cooling and dilution within the combustor lining of the engine. This increase in temperature negatively affects the power output of the engine while remaining within the stringent temperature limitations of the engine. A reduction in the temperature of charge air before being supplied to the combustor unit may result in improved performance in pre-existing engines.

1.2 Aim of the study

The aim of the study is to design a theoretical system that will use a Ti64 heat exchanger produced using LPBF to remove excess heat from air supplied by the compressor stage of a benchmark turboshaft engine.

1.3 Objectives

The research objectives of this study are as follows:

1. Characterisation of a benchmark turboshaft engine using a Brayton gas cycle.
2. Design and implementation of a heat exchanger capable of functioning as an intercooler system for the benchmark turboshaft engine.
3. Design and fabrication of a scaled test-piece heat exchanger manufactured using Ti64.
4. Experimental verification of the test piece using dimensional analysis (DA) and dynamic similarity (DS) techniques.
5. Analysis of potential benefits and drawbacks to installing the designed intercooler in turboshaft cycles.
6. Hypothesis for an optimised modification using the data obtained that could be applied to turboshaft engines.

© Central University of Technology, Free State

1.4 Concept

The overarching concept for this project is that the installation of an intercooling system of similar design to those commonly implemented in traditional automobile engines in turboshaft engines could lead to increased performance. A fundamental mechanism in the operation of turboshaft engines is the principle of cooling and dilution within the combustor unit by charge air supplied via a compressor stage [6]. Due to the lightweight nature of turboshaft engines, turboshaft combustor units contain and manage the exceptionally hot exhaust gases created during the combustion process by using a large portion of the air supplied by the compressor stage to contain, cool, and dilute the working gas before it is supplied to the power turbine stages [6]. To accomplish this, turboshaft engines commonly operate at very high pressure ratios, with one or more compressor stages providing the necessary airflow to supply the combustor unit [6]. However this rapid compression of atmospheric air by the compressor stages is also accompanied by a direct increase in the temperature of the charge air. This rise in temperature is primarily caused by the compression work performed on the gas increases the internal energy of the charge air [7], which leads to an increase in temperature. And since it is known that temperature plays an important role in the density of a gas, a reduction in the temperature of the air supplied by the compressor stages could potentially benefit the cooling effects within the combustor unit as well as increasing the amount of oxygen present during the combustion process. Additionally this could theoretically reduce the amount of work required by the compressor stages alongside a reduction in the running temperature of the turboshaft engine, which would yield an increase in power output.

The challenge of implementing this concept lies in the complexity of modifying existing turboshaft engines without compromising their performance characteristics. For instance, the installation of an intercooler into a Brayton gas cycle will result in a reduction in the thermal efficiency of the engine and an increase in the specific fuel consumption [3]. Thus, it is essential for this study to remain unbiased and examine all potential benefits and limitations with the aim of encouraging or discouraging future research on the topic.

© Central University of Technology, Free State

1.5 Approach

Because turboshaft engines are complex machines with precise performance characteristics that are closely guarded by OEMs, a generalised approach will be followed. A simple Brayton gas cycle will be utilised to obtain the performance characteristics of a benchmark engine based on a typical reverse flow annular layout commonly applied in commercial helicopters to develop a heat exchanger that functions as the desired intercooler system. The theoretical design of the intercooler system will be validated by using a test piece produced using LPBF. The experimental test piece will then be experimentally evaluated using DA and DS techniques to draw conclusions on the effectiveness of the full-scale design. The experimental results will be used to draw conclusions on the effects that the intercooler will have on the performance characteristics of the benchmark engine.

1.6 Delimitations

- This study will primarily focus on the manufacture of a Ti64 test piece segment designed using traditional design methods, namely the Keys and London method.
- Neither finite element analysis nor computational fluid dynamics analysis was considered during this study, with the verification of heat exchangers relying on experimental testing via the test piece segment and DA techniques.
- The completed and functional prototype of the intercooler system was not built or applied to a turboshaft engine in a real-world setting.

1.7 Chapter summary

This chapter introduced the problem statement and aim of the study, which is to investigate the feasibility of using AM techniques such as LPBF to manufacture heat exchangers for use in turboshaft engine intercooling.

© Central University of Technology, Free State

CHAPTER 2

Literature review

This chapter aims to identify the crucial aspects required to address the objectives of the study by investigating existing literature.

2.1 Turboshaft engines

Overview

Turbomachines can be defined as a family of devices that utilise the transfer of energy of a working fluid via the dynamic action of one or more moving blade rows [8]. This process is performed by exploiting the stagnant enthalpy, commonly accompanied by pressure, of a working fluid to perform positive or negative work depending on the application [8], [9], [10]. Common turbomachines include but are not limited to pumps, fans, compressors, and turbines [8], [9]. Various layouts of turbomachines have been developed to best exploit traits of a specific working fluid with the goal of maximising the efficiency of the application [10]. These turbomachine subtypes are commonly categorised according to the relative flow of the working fluid as having axial flow, radial inflow, or radial outflow characteristics [8].

A turboshaft engine, by definition, is a turbomachine subtype that employs a compressor stage, a combustion chamber, and a turbine stage in series to produce rotational kinetic energy using a combustible air-fuel mixture as the working fluid [11], [12], [13]. Turboshaft engines utilise the same principles as turbofan and turbojet engines but differ in that instead of producing thrust, turboshaft engines convert the energy produced by the combustion process into rotational kinetic energy via the use of a power turbine stage [6]. In a standard turboshaft layout, the rotational energy supplied by the turbine is then transferred to a geared transmission, which provides the required torque to the machine [11], [12], [14]. Common turboshaft applications include but are not limited to helicopters, electrical generators, compressors, pumps, tanks, hovercrafts, and hydrofoils [11]. A diagram of a traditional twin-spool turboshaft engine layout is shown in Figure 1,

© Central University of Technology, Free State

which illustrates the process by which air is taken in from the atmosphere and passes through the various stages of the engine.

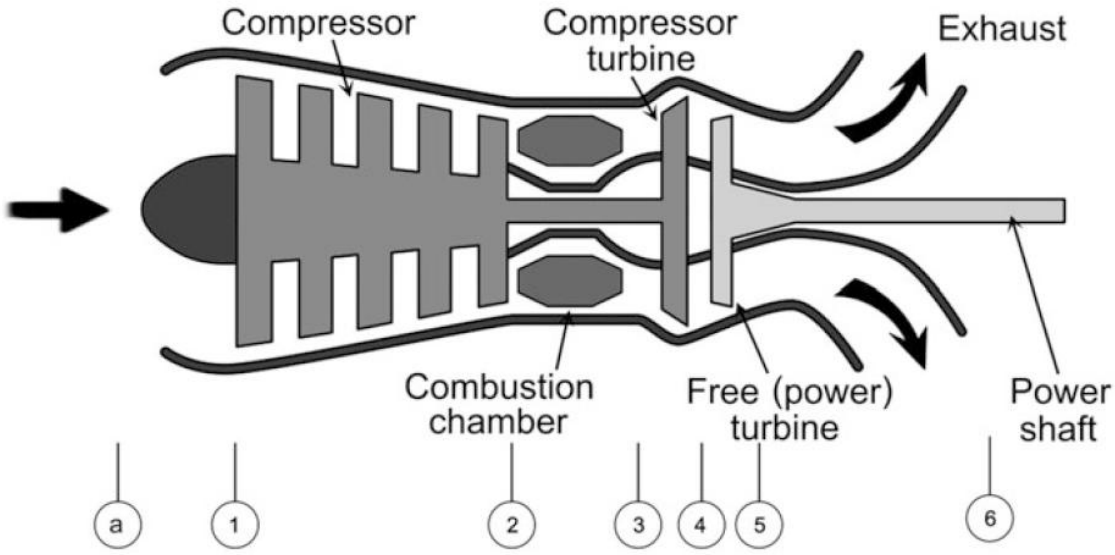

Figure 1: Twin-spool free power turbine turboshaft layout [11]

Combustor unit

The combustion chamber, typically referred to as a combustor unit, is used to mix and ignite the air-fuel mixture in a turboshaft engine, as well as regulate the emissions of the engine [15], [16]. Combustors used in turboshaft engines are designed to be lightweight and cannot directly sustain the heat created by the combustion process for an extended period of time [6]. This issue is circumvented by using the air supplied via the compressor stage, not only as the medium to ignite the fuel but also to manipulate and control the exhaust gases to protect the combustor lining of the engine [6]. In this process, pressurised air is injected via a series of holes in the combustor lining to generate a protective film of air to prevent the combustion flame from making direct contact with the internal walls of the combustor unit [6]. A common combustor type utilised in turboshaft engines is the can-annular layout, shown in Figure 2, which uses a cylinder with holes to direct and control the flow of air.

© Central University of Technology, Free State

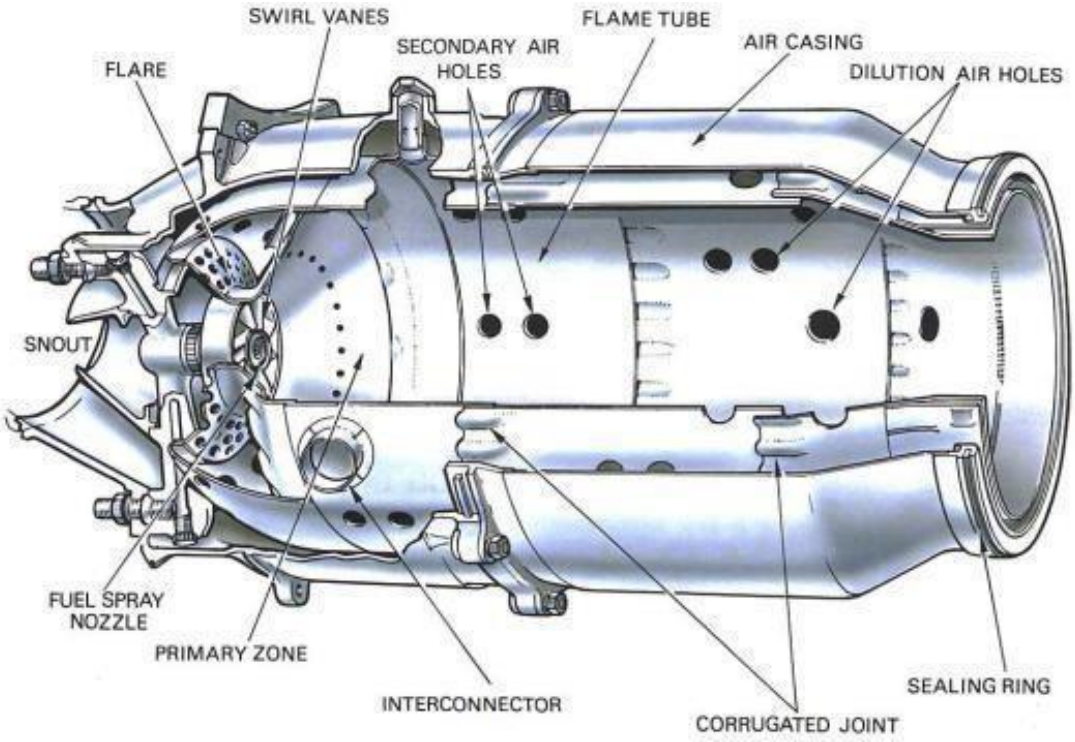

Figure 2: Reverse flow can-annular combustor [6]

This cylinder, often referred to as the combustor lining, serves to divide the air supplied by the compressor stage into different channels which perform individual operations within the combustor [6], [15], [17], [18]. Figure 3 illustrates this process wherein the charge air supplied by the compressor is split into ignition, cooling, and dilution air supplies. The combination of these operations results in a contained combustion process that allows the turboshaft engine to operate continuously without the exhaust gases directly contacting the walls of the combustor lining [6].

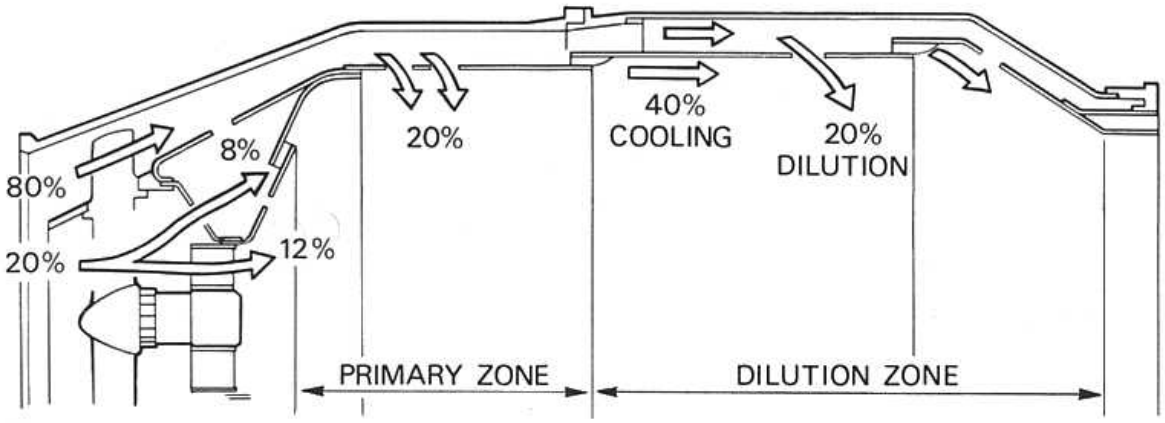

Figure 3: Internal cross section of can-annular combustor unit lining [6]

© Central University of Technology, Free State

Spool layout

Unlike turbojet engines, which produce thrust, turboshaft engines use turbine stages to convert the energy produced by the combustor unit into rotational kinetic energy [6]. This is achieved by using multiple high and low pressure turbine stages, which are assembled in series to maximise the power output from the system. An important aspect that influences the operation of the turbine stages is the spool layout of the turboshaft engine, with the spool layout referring to the number of shaft connections inside the engine. The most common turboshaft engine layouts utilise single-spool and twin-spool configurations [6], [19].

In a single-spool layout, the compressor and turbine stages are all connected by a single concentric shaft which leads directly to the geared transmission [11], [19]. In this layout, the overall power output from the engine directly influences the behaviour of the compressor and the turbine stages, greatly limiting the flexibility of the system [6]. In a twin-spool layout, the compressor stages are connected to a dedicated turbine stage known as a high power turbine (HPT), which delivers the necessary energy needed to drive the compressor. A second dedicated turbine stage known as the free power turbine (FPT) connects to a geared transmission, which results in an output of rotational power from the engine [20].

2.2 Brayton gas cycle

The Brayton gas cycle is an idealised model of the behaviour and properties of a certain mass of a working fluid, commonly a gas, as it flows through an open-cycle turboshaft engine [21]. Figure 4 describes the operating procedure of the Brayton cycle, where:

1. Air enters the compressor stage at atmospheric conditions (1).
2. Air passes through the low pressure (LP) compressor, which reduces the volume and increases the pressure of the air (1–2).
3. Air passes through the high pressure (HP) compressor, which reduces the volume and increases the pressure of the air further (2–3).
4. The combustor unit injects fuel and ignites the air-fuel mixture, causing an isobaric gas expansion (3–4).

© Central University of Technology, Free State

5. Gas expands through the HPT, which drives the high and low pressure compressors (4–5).
6. Gas expands through the FPT, which provides the rotational kinetic energy output from the system (5–6).
7. Waste gas is expelled into the atmosphere (6).

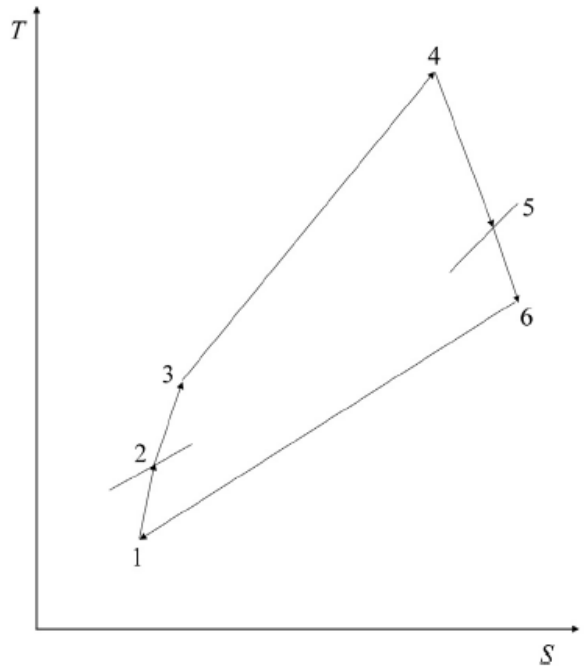

Figure 4: Temperature-entropy diagram of twin-spool turboshaft engine [20]

Please note that for the aforementioned Brayton gas cycle, all expansion and compression processes are assumed as isentropic in nature with the energy loss across these processes being represented as an isentropic efficiency.

2.3 Heat exchangers

Heat exchangers refer to a category of devices which aim to facilitate heat transfer between one or more working fluids which is commonly accompanied by a change in temperature [22]. Recuperative heat exchangers constitute the most common type utilised in industry, wherein a set of working fluids continuously exchange heat via a series of dividing walls and are commonly divided according to their working principles as either direct or indirect contact configurations [22], [23]. Direct contact refers to the layout in which the two working fluids come into direct contact and mix with one another during the heat transfer process [23], [24]. Indirect contact refers

© Central University of Technology, Free State

to a layout in which working fluids are completely separated via a dividing wall during the heat transfer process [23].

Recuperative heat exchangers can be further divided by the particular flow configuration of the system, as shown in Figure 5, with the prominent ones being co-current flow, where the working fluids flow in the same direction; con-current flow, where the fluids cross in opposite directions; cross flow, where the fluids flow in a perpendicular fashion; and hybrid flow, where the fluids cross one another multiple times in succession [22], [25].

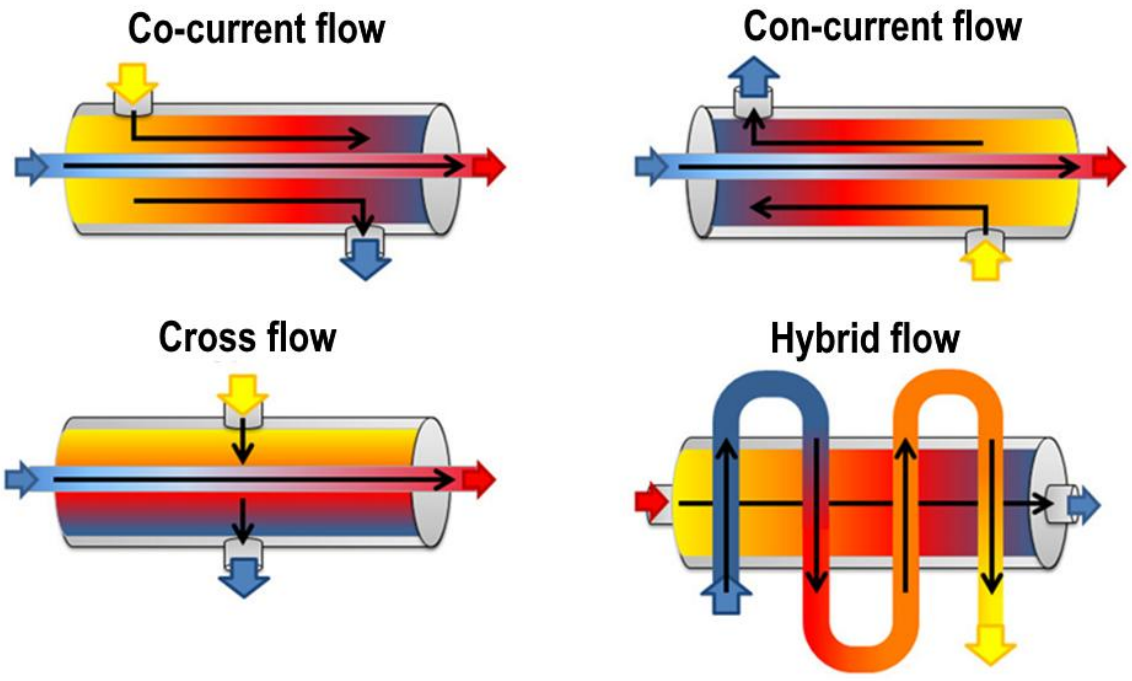

Figure 5 Common recuperative heat exchanger flow configurations [25]

Heat exchangers are then further characterised by the physical characteristics of the heat exchanger, with primary examples being the shell and tube and compact heat exchanger layouts. The shell and tube refers to a layout in which a hot fluid passes through one or more pipes placed inside a shell containing a cold working fluid, as seen in Figure 6 [23], [26].

© Central University of Technology, Free State

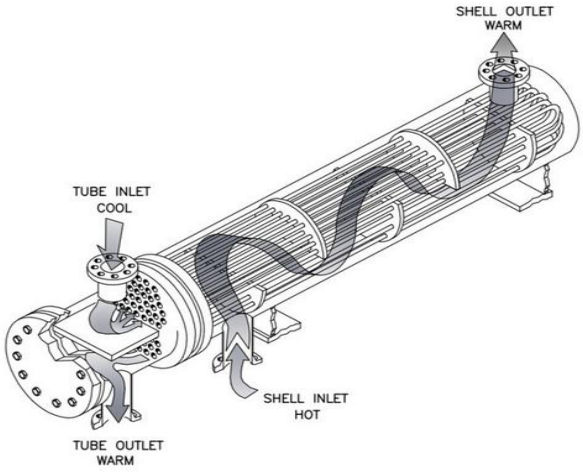

Figure 6: Shell and tube recuperative heat exchanger [26]

Compact heat exchangers, commonly known as just cross-flow heat exchangers, refers to a layout which aims to maximise the heat transfer area per volume [7]. The most widely utilised compact heat exchangers are the finned-tube and compact arrangements, as shown in Figure 7. The finned-tube layout uses a series of heat conducting pipes connected to metal plates which serve to increase the heat transfer area of the heat exchanger, indicated in Figure 7 a). The plate-fin configuration, on the other hand, uses a series of metal fins situated between dividing walls to facilitate the transfer of heat between the working fluids, as indicated in Figure 7 b).

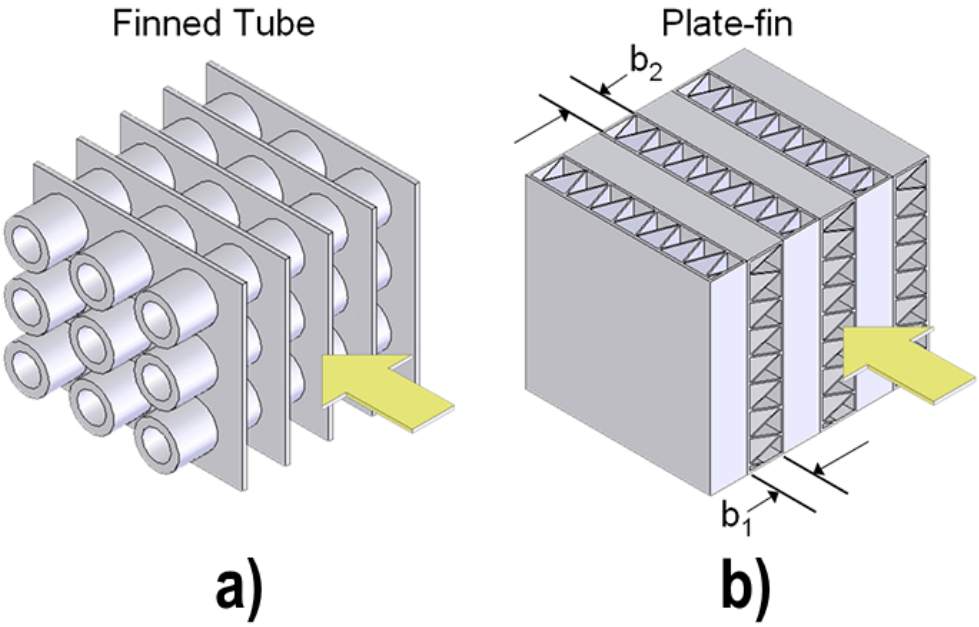

Figure 7: Finned-tube a), and plate-fin b) heat exchanger layouts [27]

© Central University of Technology, Free State

2.3.1 Recuperation in turboshaft engines

Gas cycle recuperation, also referred to as regeneration, is the process of implementing heat exchangers in a gas cycle to recover the thermal energy expelled from the cycle by the exhaust gas to preheat the air supplied to the combustion chamber [3], [20], [28]. Such a system is applied in a gas cycle by installing a heat exchanger that transfers heat from the engine exhaust gas to the air intake of the combustion chamber [20]. When applied to turboshaft engines, recuperators are usually installed with the hot side of the heat exchanger downstream of the FPT, which serves to transfer waste heat back into the system [12], [20]. An illustrative diagram of this configuration is shown in Figure 8, as provided by Fakhre et al. [12].

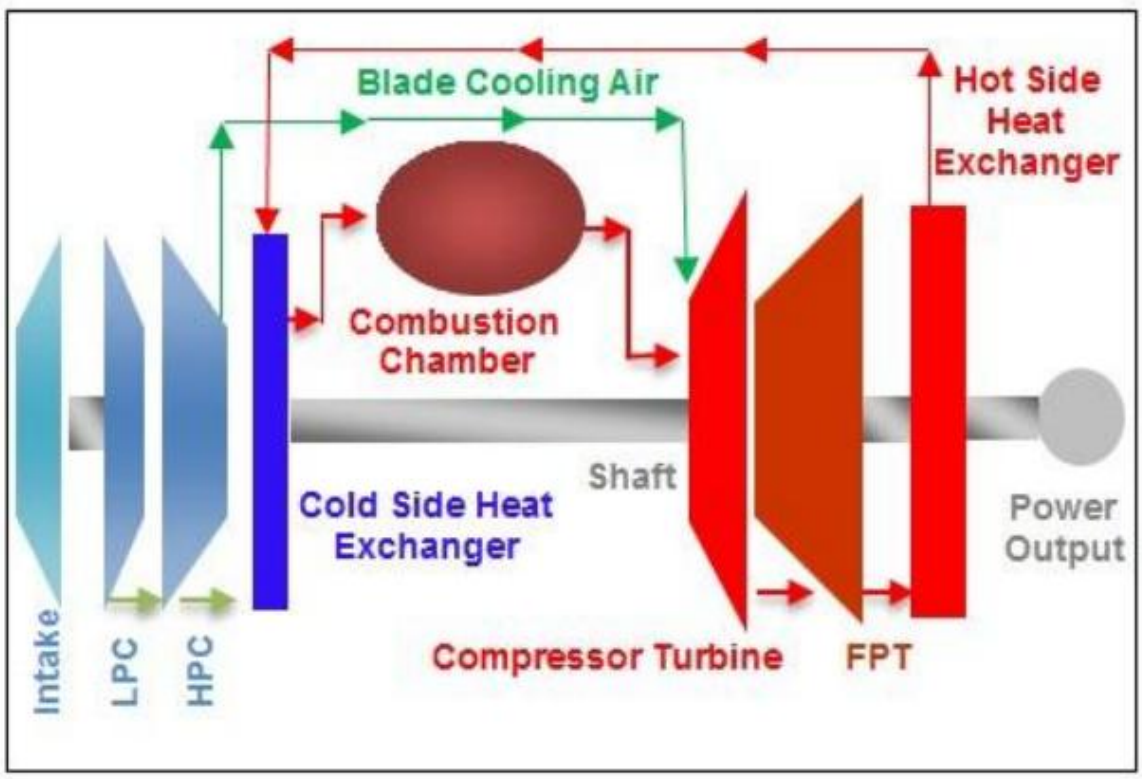

Figure 8: Single-spool recuperated turboshaft engine layout [12]

The effects of such a system result in an increase in the thermal efficiency of the engine caused by the reintroduction of waste heat back into the system, which is commonly accompanied by an improvement in the specific fuel consumption (SFC) of the engine [29].

© Central University of Technology, Free State

2.3.2 Intercooling in turboshaft engines

Intercoolers refer to a wide variety of devices commonly used in gas cycles to reduce the temperature of a working fluid after compression has occurred [22], [30]. An intercooler operates on the principle that for a perfect gas, temperature and density are inversely proportional when the pressure remains constant [22]. This means that reducing the temperature of a gas at constant pressure will results in a direct increase in the density of the working gas.

When applied to turboshaft engines, intercoolers are utilised in the form of stage intercooled gas cycles, in which air passing through the compressor stages is successively cooled down to inlet conditions [31]. An illustrative diagram of this configuration is shown in Figure 9, as adapted from the work of Lebre and Brojo [14], which indicates how an intercooler unit may be placed between the compressor stages of a turboshaft engine.

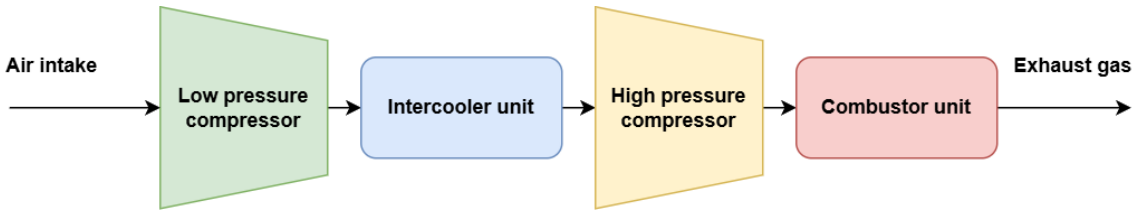

Figure 9: Common stage intercooled layout, (illustration by author)

The process of cooling charge air to initial starting conditions can directly reduce the amount of work required by the compressor stages which leads directly to an increase in the net-specific work of the system [32]. This effect can be observed in Figure 10, which shows the increase in both net-specific work and efficiency of a stage intercooled turboshaft engine when compared to the simple unmodified engine.

© Central University of Technology, Free State

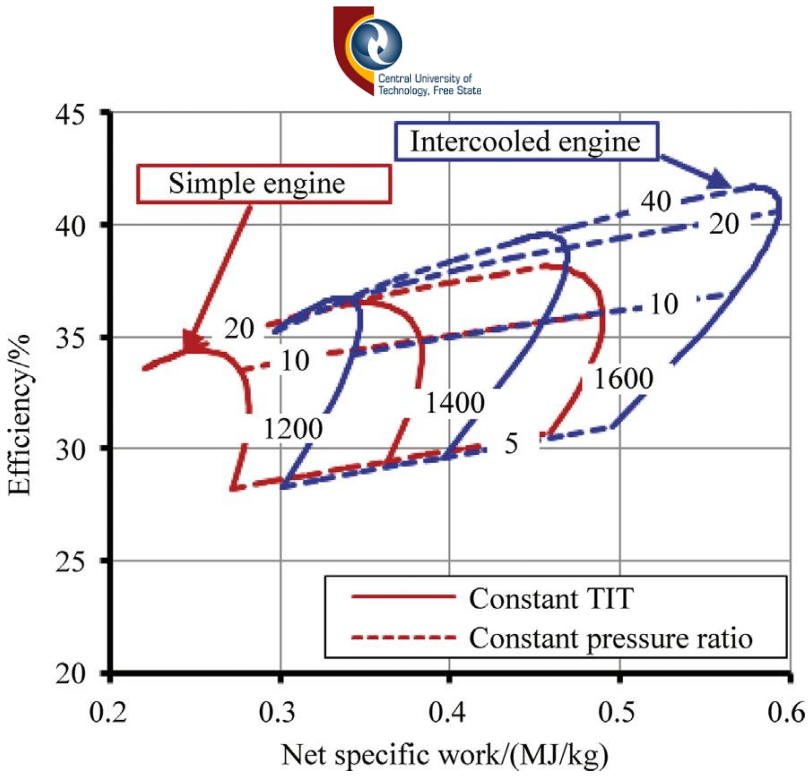

Figure 10 Simple vs intercooled turboshaft engine performance [32]

Since the pressure is kept constant across the intercoolers, the subsequent reduction in air temperature results in an indirect rise in the density of the air supplied by the compressor stages. However, due to pressure drops that occur in reality across an intercooler, the system's performance will be negatively affected in thermal efficiency and fuel consumption [30].

2.3.3 Combined intercooling and recuperation in turboshaft engines

A generally accepted viewpoint is that a combination of both intercooling and recuperation principles leads to a more efficient form of Brayton gas cycle when applied to turboshaft engines [3], [20], [30], [32]. In this layout, an intercooler is installed between the compressor stages, and a recuperator is installed in front of the combustion chamber [20]. Figure 11 shows an example of a stage intercooled gas turbine layout with a waste heat recuperator, as presented by Ariemma et al. [33].

© Central University of Technology, Free State

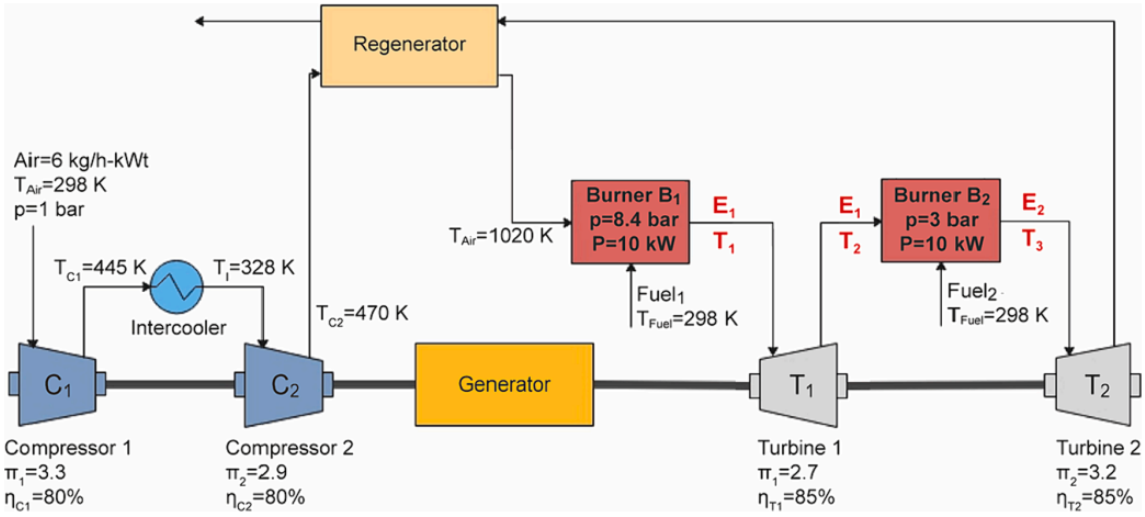

Figure 11: Intercooled-recuperated gas turbine layout [33]

In this layout, the intercooler stages serve to reduce the work input required by the compressor stages, while the recuperator offsets the thermal efficiency losses caused by the intercoolers [30]. This effect can be observed in Figure 12, as presented by Nada [32], which displays the efficiency increase relative to net-specific work obtained by adding a waste heat recuperator to a stage intercooled turboshaft engine.

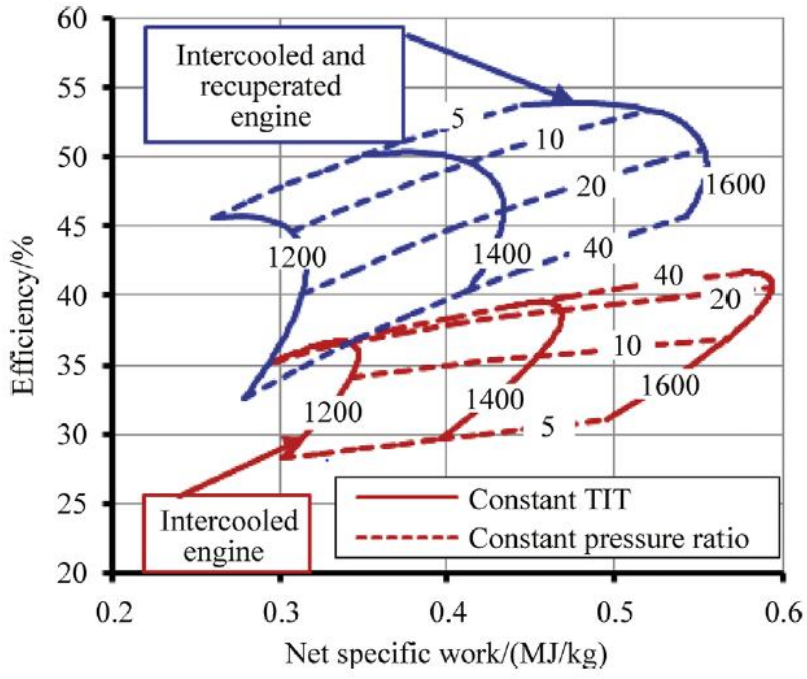

Figure 12: Intercooled vs intercooled-recuperated turboshaft engine [32]

© Central University of Technology, Free State

A combined intercooler-recuperator system will show notable improvements in the net-specific work, indicated power, thermal efficiency, and specific fuel consumption (SFC) when compared to an unmodified system [12], [20], [32].

2.3.4 Heat exchanger design techniques

In the field of thermodynamics, there are numerous techniques that can be utilised to develop heat exchangers, either using standardised or custom layouts, with one of the most common and reliable methods to develop heat exchangers being the effectiveness number of transfer units (ε-NTU) method [7]. This technique estimates the heat transfer capacity of a heat exchanger by characterising the relationship between the number of transfer units (NTU) (Eq. 2.1) and the effectiveness (Eq. 2.2) of a heat exchanger, commonly provided in the form of charts and tables obtained from experimental data [34]. An example of such a relationship for a compact cross-flow heat exchanger, as presented by Holman [7], is described in Eq. 2.3,

$$NTU = \frac{UA}{C_{min}} \quad \text{Eq. 2.1}$$

$$\varepsilon = \frac{q_{actual}}{q_{maximum}} \quad \text{Eq. 2.2}$$

$$\varepsilon = 1 - exp\left[\frac{exp(-NTU * C_r(NTU^{-0.22}) - 1)}{C_r * NTU^{-0.22}}\right] \quad \text{Eq. 2.3}$$

where the actual heat transfer across the heat exchanger is defined as the heat transfer across either the hot or cold side working fluids, indicated in Eq. 2.4.

$$q_{actual} = C_{hot}(T_{h,i} - T_{h,o}) = C_{cold}(T_{c,i} - T_{c,o}) \quad \text{Eq. 2.4}$$

The maximum heat transfer across a heat exchanger is defined as the heat transfer between the hot and cold side working fluids, indicated in Eq. 2.5.

$$q_{maximum} = C_{min}(T_{h,i} - T_{c,i}) \quad \text{Eq. 2.5}$$

The overall heat transfer coefficient (U) is then used to represent various resistances present during the heat transfer process, namely the convective and conductive resistances [7], [34]. These resistances can be quantified by adding them together in series, as seen in Figure 13.

© Central University of Technology, Free State

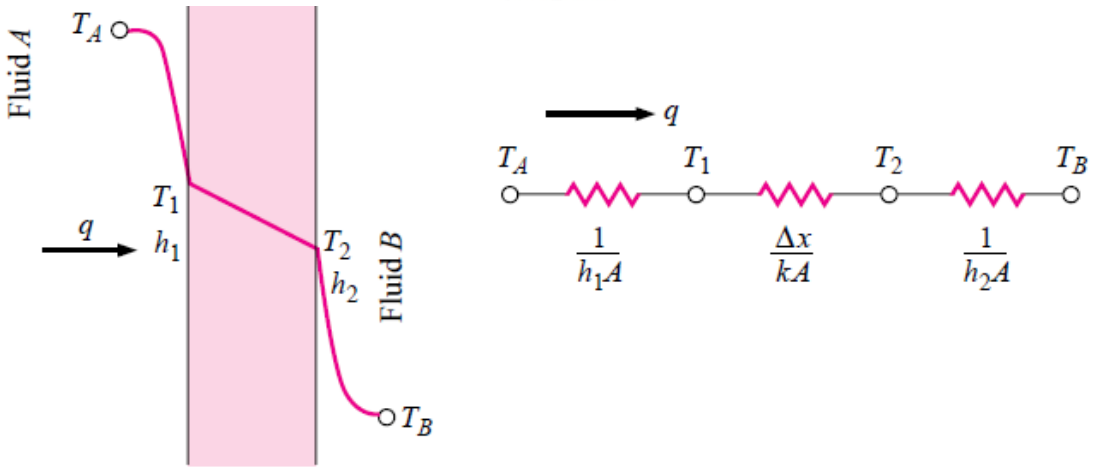

Figure 13: Convective and conductive resistances across a metal plate [7]

Eq. 2.6, presented by Kays and London [34], may then be used to add together the individual convention and conduction resistances to calculate the overall thermal conductance (UA) for a given material.

$$\boldsymbol{U_i A_i = \frac{1}{\frac{1}{h_i A_i n_i} + R_{wall} + \frac{1}{h_o A_o n_o}}} \qquad \text{Eq. 2.6}$$

Kays and London [34] extensively studied various types of compact heat exchanger layouts during their research, and quantified the relationships between the Reynolds number (Re), fanning friction factor (f), Stanton number (St), and Prandtl number (Pr) for numerous compact heat exchanger layouts. The resulting data was compiled into surface heat transfer diagrams, with the necessary data to design a heat exchanger for a particular layout [23], [34], [35]. An example of such a diagram for a finned-tube heat exchanger is seen in Figure 14, as presented by Holman [7], which shows the relationship between the Colburn (j or $StPr^{2/3}$) and fanning friction (*f*) factors against the Reynolds number (Re) of the working fluids.

© Central University of Technology, Free State

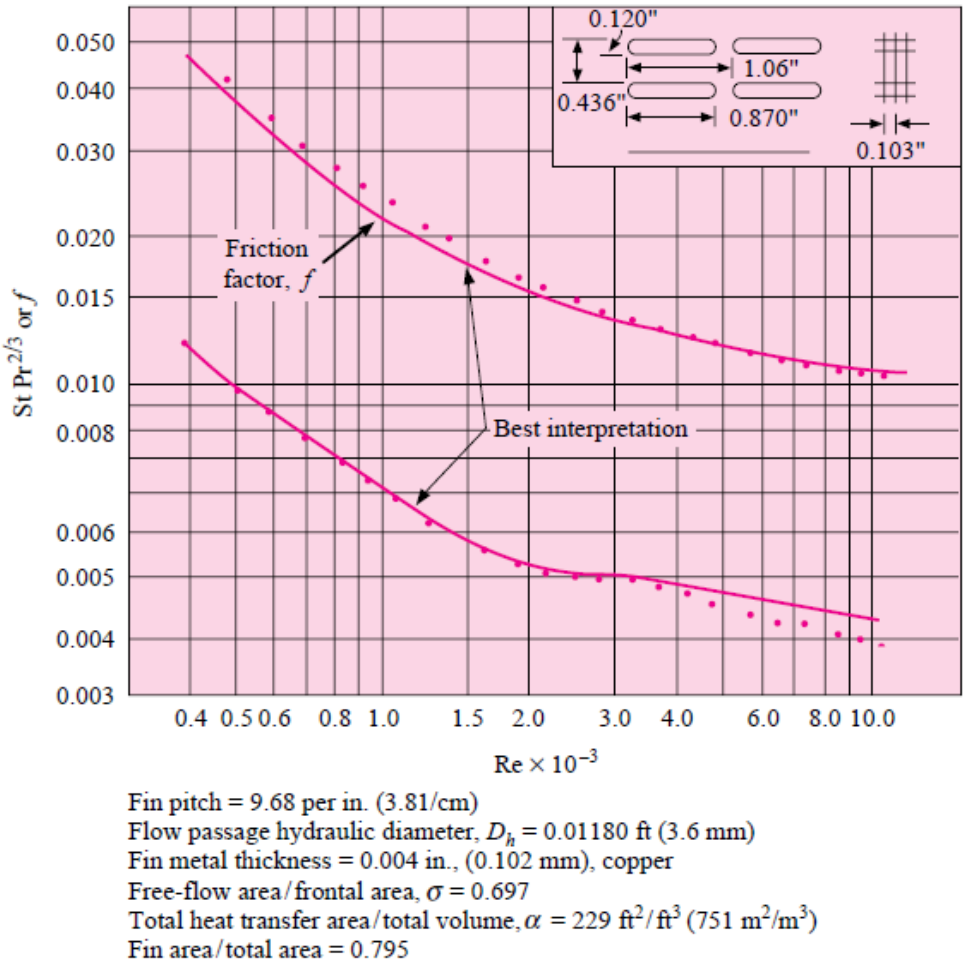

Figure 14: Heat transfer diagram for heat exchanger [7]

An important consideration in the design of a heat exchanger is the pressure drop across the hot and cold sides. This effect can be quantified with the following formula, originally derived by Kays and London [34] and corroborated by Shah and Sekulic [35].

$$\frac{\Delta P}{P_i} = \frac{G^2}{2g_c\rho_i P_i}\left[(1-\sigma^2+K_c)+2\left(\frac{\rho_i}{\rho_o}-1\right)+f\left(\frac{l}{r_h}\right)\left(\frac{\rho_i}{\rho_m}\right)-(1-\sigma^2+K_c)\left(\frac{\rho_i}{\rho_o}\right)\right] \qquad \text{Eq. 2.7}$$

Heat exchanger effectiveness

Due to heat exchangers being exceptionally complex devices, numerous methodologies have been developed to closer simulate real-world behaviours. One of these methodologies is an iterative methodology proposed by Shah and Sekulic [35] using the research originally performed by Kays and London [34]. This methodology was found to be of particular importance to this study since it can be

© Central University of Technology, Free State

utilised to size and estimate the performance characteristics of heat exchanger with little starting information. This methodology initially estimates the effectiveness of the heat exchanger which is then used to calculate the actual efficiency of the heat exchanger [35]. The estimated and actual effectiveness of the heat exchanger are then compared, and if the actual effectiveness differs for the first data set, a subsequent data set is calculated using the effectiveness values from the previous iteration [35]. Convergence occurs when the estimated and actual effectiveness arrive at the same value. A simplified flow chart of this process is shown in Figure 15.

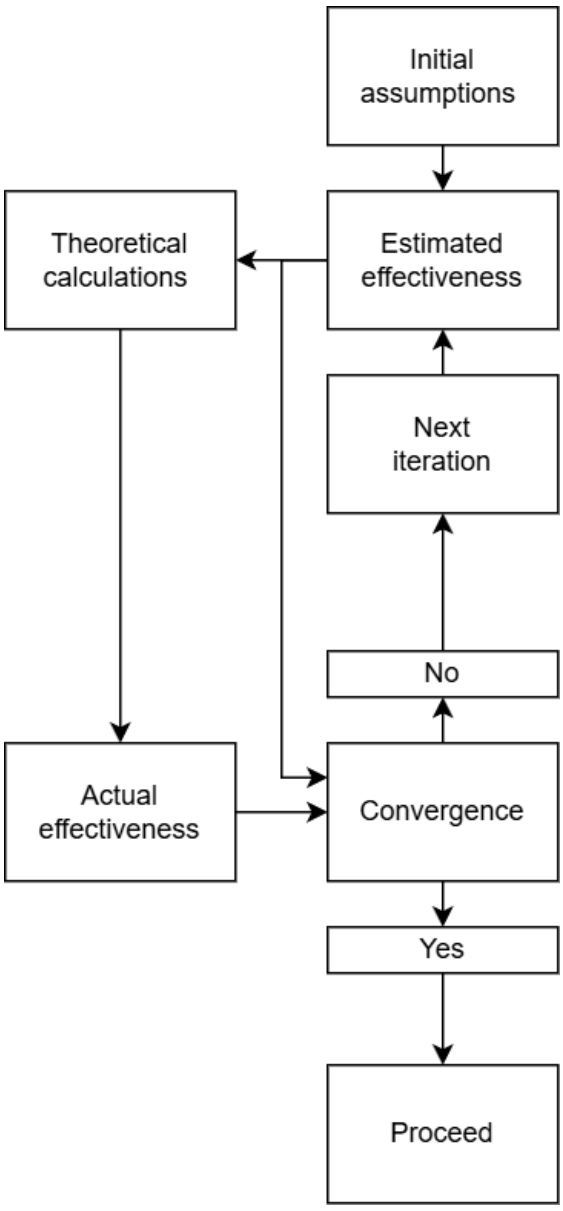

Figure 15: Simplified heat exchanger design process

© Central University of Technology, Free State

2.4 Dimensional analysis and similarity

As it is not always feasible to manufacture and test a full-scale design of a device or system, DA and the concept of similarity may be applied to create scaled models that can be produced and tested at reduced size and cost [8]. DA refers to the process by which nondimensional parameters are derived for use in design and experimental testing, with the most common application being in the form of similarity [8], [36]. By applying similarity laws and nondimensional parameters during the design process of a prototype, a scaled model can be created that, when tested under experimental conditions, will be capable of verifying the prototype [36]. Using the principles of DA for a model and a prototype to share similarities, the following conditions need to be met [8], [36]:

1. The independent Pi groups for the model and prototype must match, as indicated in Eq. 2.8.

$$\Pi_{2,m} = \Pi_{2,p}, \Pi_{3,m} = \Pi_{3,p}, \ldots \Pi_{k,m} = \Pi_{k,p} \quad \text{Eq. 2.8}$$

2. There must be a geometric similarity between the model and prototype. The model must be of a similar shape to the prototype but may be scaled according to a constant scale factor.
3. Kinematic similarity must exist between the model and the prototype, with the velocity at any point within the model being proportional to the velocity at the corresponding point in the prototype, according to a constant scale factor.
4. Dynamic similarity should exist between the model and prototype. To achieve complete dynamic similarity, both geometric and kinematic similarity conditions are necessary, along with ongoing force-scale equivalence between the model and prototype.

If all four requirements are met, the dependent variable will share similarity between the model and the prototype, Eq. 2.9 can be used to predict the experimental performance of the prototype:

$$\Pi_{1,m} = \Pi_{1,p} \quad \text{Eq. 2.9}$$

© Central University of Technology, Free State

2.4.1 Dimensional analysis as applied to heat exchangers

Using the research performed by Sánchez-Escalona et al. [37], the Buckingham pi method of dimensionless numbers may be applied to the principles of the ε-NTU method to obtain the dimensionless Pi groups as stated in Eq. 2.10 and Eq. 2.11,

$$\Pi_1 = \frac{T_{c,o} - T_{c,i}}{T_{h,i} - T_{c,i}} \quad \text{Eq. 2.10}$$

$$\Pi_2 = \frac{\dot{m}_h}{\dot{m}_c} \quad \text{Eq. 2.11}$$

where the relationship between the two pi groups is determined by Eq. 2.12.

$$\Pi_1 = f(\Pi_2) \quad \text{Eq. 2.12}$$

Thus, the heat transfer characteristics of the heat exchanger can be considered as a factor of the ratio of the mass flow rates of the hot and cold side fluids indicated in Eq. 2.13.

$$\frac{T_{c,o} - T_{c,i}}{T_{h,i} - T_{c,i}} = f\left(\frac{\dot{m}_h}{\dot{m}_c}\right) \quad \text{Eq. 2.13}$$

Sánchez-Escalona et al. [37] did not use the aforementioned DA expression for the testing of a scale model, but instead for making an explicit expression to gauge the performance of an existing heat exchanger using experimental data and linear regression analysis. However, the underlying principles remain the same for DS constraints and can be used in the testing of a scale model. Thus, if geometric, kinematic, and DS conditions are applied to the model, similarity between the dependent variable of the model and the prototype may also be established in the form of Eq. 2.14.

$$\left(\frac{T_{c,o} - T_{c,i}}{T_{h,i} - T_{c,i}}\right)_{Test-Piece} = \left(\frac{T_{c,o} - T_{c,i}}{T_{h,i} - T_{c,i}}\right)_{Single-Passage} \quad \text{Eq. 2.14}$$

Having obtained the necessary dimensionless number groups, DS conditions can be used to evaluate experimental data against theoretical calculations [36], thereby verifying the model which will approximate the performance of the heat exchanger.

To ensure that the similarity requirements are as close as possible between the theoretical and experimental data, a series of calculations must be performed to ascertain the exact conditions required during experimental testing to match the DS constraints.

© Central University of Technology, Free State

2.4.2 Effect of gas temperatures on emissions

It is accepted that a combination of the combustor temperature and pressure, fuel to air ratio, and atomisation of fuel primarily influence the emissions generated by turbojet engines [38]. In the report 'Scheduled Civil Aircraft Emission Inventories for 1999: Database Development and Analysis' by Sutkus et al. [39] for NASA, it was concluded that carbon monoxide and unburnt hydrocarbon emissions for turbojet engines were the highest under low power conditions, where the temperature of the air leaving the combustion chamber was the lowest. Thus, when a combustor runs at a lower temperature, the fuel might not undergo a complete combustion process, which can result in the generation of additional carbon monoxide as well as an increase in unburnt hydrocarbons, leaving the engine [40].

A significant point of this study is the potential impact that lowering the temperature in a combustor unit, due to the installation of an intercooler, could have on the emissions produced by such a system.

2.5 Additive manufacturing

2.5.1 Overview

AM has been integrated into Industry 4.0 as a functional manufacturing technology, and since 2016, ASTM International has been working in collaboration with the International Organization for Standardization (ISO) to develop standards applicable to AM-fabricated parts with the goal of further developing the rapidly growing AM industry [41]. AM refers to a process in which a three-dimensional (3D) object is manufactured in a layered fashion [42], [43] and can be categorised according to the ISO/ASTM 52900 standard into seven main categories:

- Material extrusion
- Material jetting
- Binder jetting
- Sheet lamination
- Vat polymerization
- Powder bed fusion
- Directed energy deposition

© Central University of Technology, Free State

Despite utilising different technologies, all AM techniques follow a similar approach to building physical objects. Firstly, a layer of the desired material is deposited onto a build plate at a certain layer height, and thereafter, a subsequent layer of material is deposited on top of the previous layer. The process is repeated until the object has been successfully printed [42]. A fundamental part of the AM process is part slicing, which refers to the act of taking a 3D computer-aided design (CAD) model and converting it into numerous 2D cross sections in the horizontal (X-Y) plane. When subsequently layered on top of one another in the vertical (Z) plane, these sections will result in a physical 3D model of the original CAD model [44]. An illustration of this process, as provided by Palmer and Laliberte [45], is seen in Figure 16, which displays how a vertical shape can be created using individual layers.

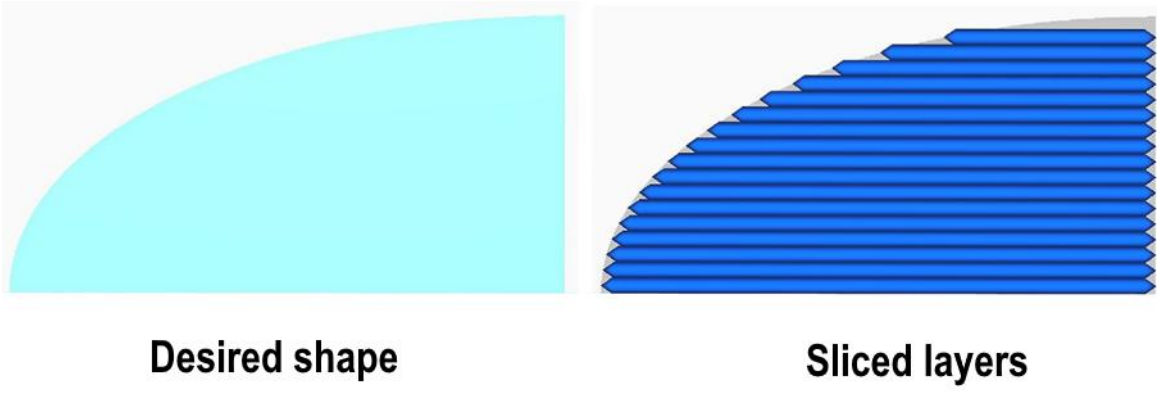

Figure 16: Illustration of slicing process [45]

The slicing process considers numerous parameters, such as layer height, infill patterns, density, supporting structures, and operating dimensions, which can be adjusted to help improve the quality of the final print. The sliced CAD model is then exported in the form of a G-code file, which comprises the commands that the 3D printer needs to create the object [46]. Another design input that is vital to AM processes is support structures. Support structures act as scaffolding for the addition of new layers that would normally not be able to be built, such as overhangs or cavities [42], [47]. Support structures are commonly found in most AM processes; however, they play a critical role in metallic 3D printing techniques by serving to anchor the part onto the build plate, acting as heat sinks for heat dissipation, and assisting in stress-relief heat treatments [48], [49].

© Central University of Technology, Free State

2.5.2 Powder bed fusion (PBF)

Powder bed fusion (PBF) refers to a number of AM processes where a heat source is used to fuse or sinter material in the form of a powder [50]. Processes that fall in this category are selective laser sintering (SLS), laser powder bed fusion (LPBF), and electron beam melting (EBM).

SLS

SLS is a process in which a carbon dioxide laser sinters powder into solid layers. The materials suitable for SLS are typically restricted to polymers and ceramics, as the lasers used in the SLS process cannot completely melt the printed material; instead, they sinter the particles together. This is a contributing factor to the lower strength of SLS compared to parts manufactured using SLM [51].

EBM

EBM is an AM process similar to LPBF, but instead of using a laser, it utilises an electron beam to impart the thermal energy required to melt the powder layers [52]. Unlike LPBF or SLS, the EBM process requires the build enclosure to be in a complete vacuum for the electron beam to function correctly [53]. Because of the enhanced power of the electron beam compared to a laser, the EBM process can produce high-density parts, enabling this technique to be utilised in the medical and aerospace industries [53].

LPBF

Laser powder bed fusion (LPBF) is an AM technique that uses laser beam thermal energy to melt fine metal powder completely [54], [55]. Since LPBF has the capacity to fully melt the particles of a metallic powder, it is considered a fast-welding process, which is applicable to a large array of metal powders, such as titanium-based alloys, nickel-based superalloys, aluminium-based alloys, cobalt-chrome alloys, stainless steels, gold, silver, platinum, refractory metals, copper-based alloys, intermetallic, and low-alloy steels [54].

The typical mechanical layout of an LPBF machine consists of a build plate and a powder plate capable of independently moving up or down in the vertical Z direction, a powder roller, which can disperse and level the powder across the build plate, a laser unit capable of sintering or melting the metallic powder, and a scanner head that can move freely in the horizontal X-Y plane, which can direct the light

© Central University of Technology, Free State

produced by the laser unit onto the build plate [48], [54], [56]. An illustration of this layout is set out in Figure 17.

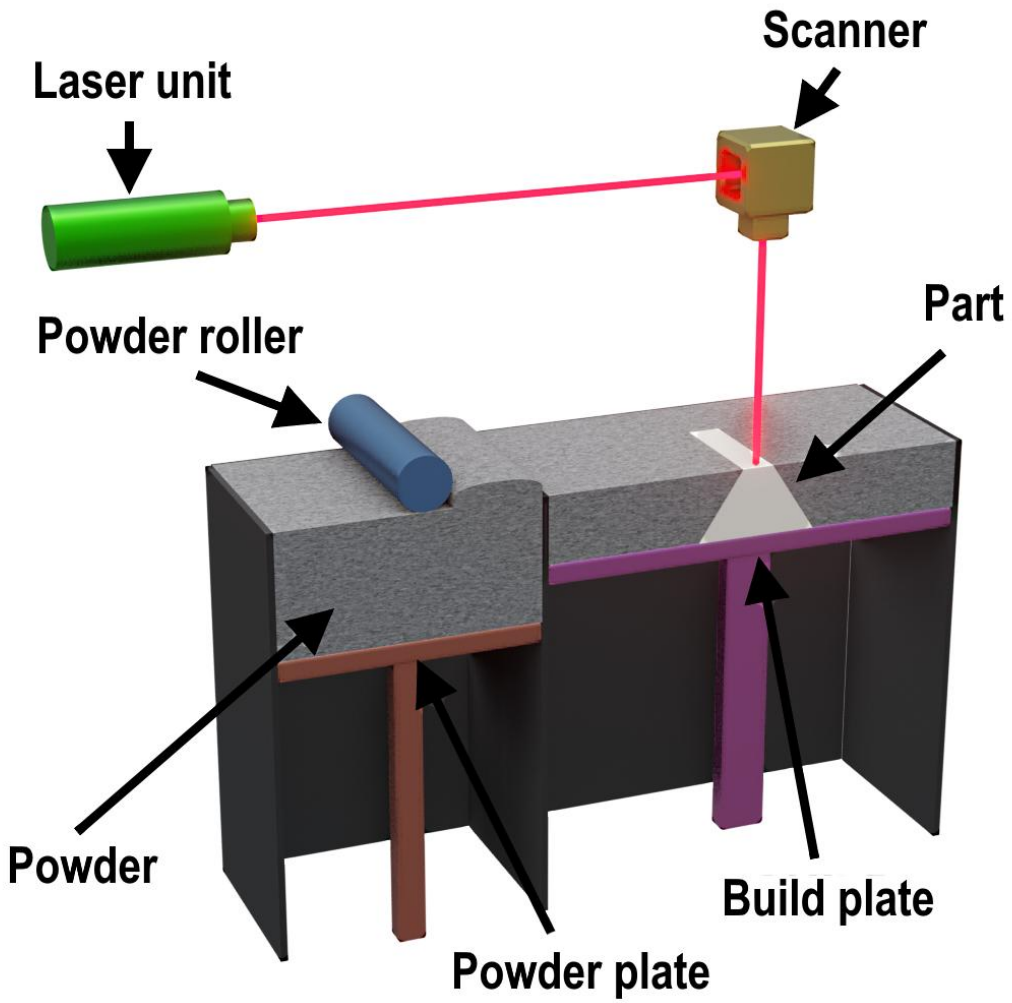

Figure 17: Cross-sectional layout of LPBF machine (illustration by author)

The operating procedure for an LPBF machine begins with the build plate being levelled and metallic power loaded onto the powder plate. The powder roller evenly deposits a layer of material onto the build plate. The scanner head then directs the laser beam towards the build plate, where the metal powder is selectively melted. The build plate is lowered, and the powder roller deposits a new powder layer onto the build plate, which is subsequently fused by the laser beam. The process is then repeated until the object has been successfully manufactured [48], [54], [56]. Figure 18 shows the individual steps involved in the LPBF process.

© Central University of Technology, Free State

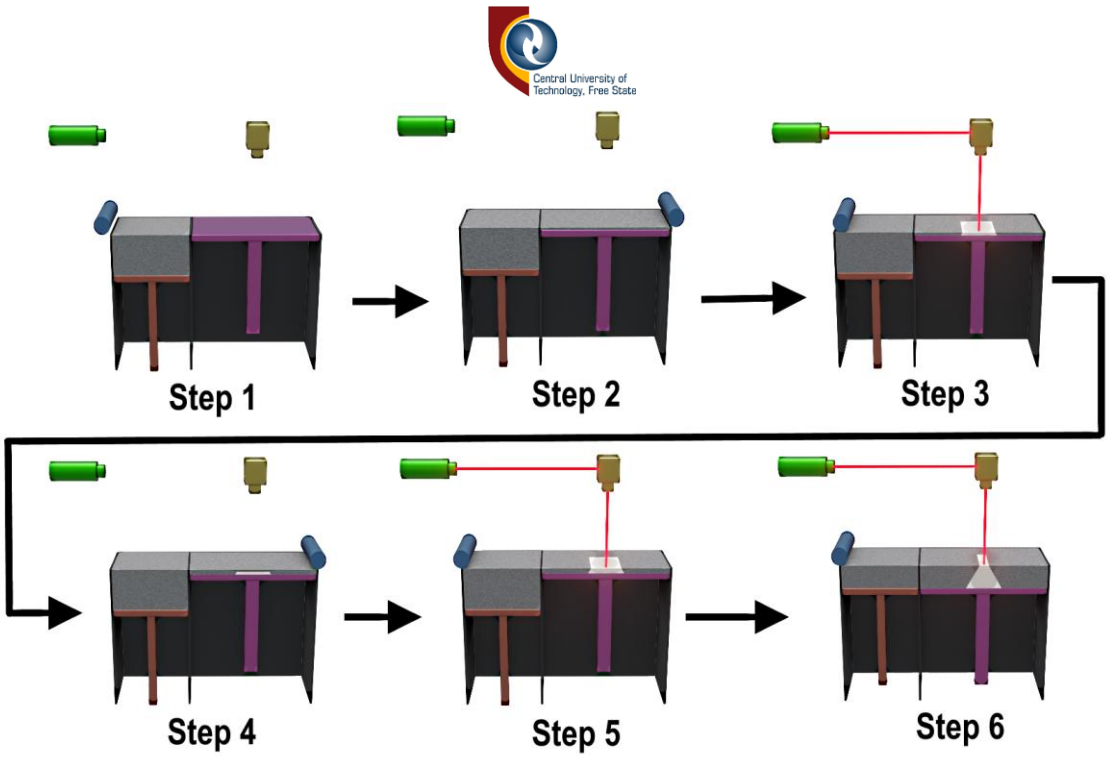

Figure 18: Operation of LPBF machine (illustration by author)

Patterson et al. [56] refers to the LPBF process as one comparable to a fast welding process, which means that parts typically experience high internal stresses caused by temperature gradients present during the building process. These stresses are referred to as residual stresses and can be defined as the stress present in an object without the influence of any external forces [57]. The largest contributing factor to residual stresses in LPBF parts is the interaction between new and underlying layers in the fabrication process [56]. Residual stresses arise when underlying layers that are in the process of cooling have a new molten layer added on top, the effect of which is an uneven stress gradient due to the individual layers undergoing uneven expansion and contraction [56]. Figure 19, adapted from Patterson et al. [56], displays how the heating process causes compressive stresses in subsequent layers, while the cooling process results in tensile stress in subsequent layers.

© Central University of Technology, Free State

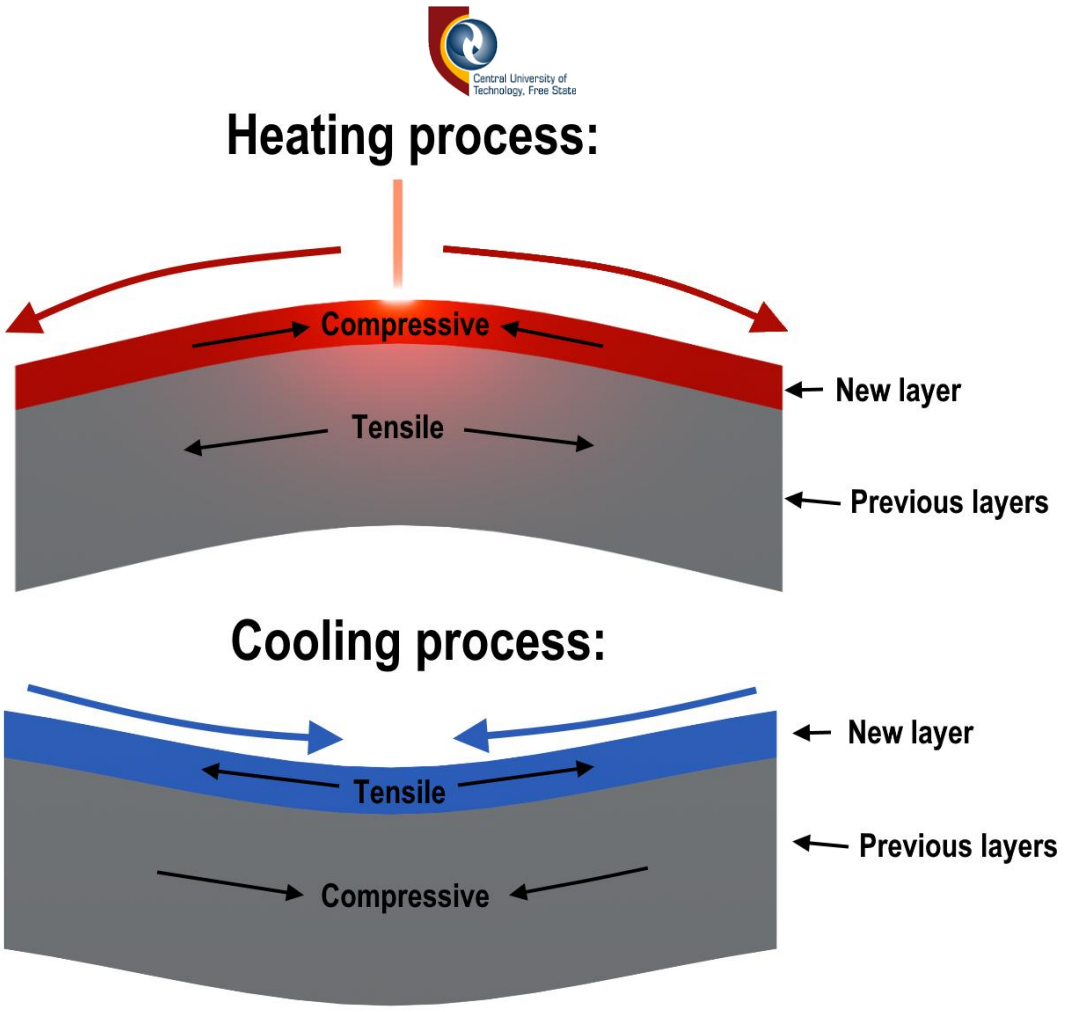

Figure 19: Interaction between layers during fabrication (illustration by author)

If left untreated, this inherent flaw in the LPBF process commonly leads to warping, reduced strength, surface cracking, delamination, and accelerated fatigue of AM parts [56], [58]. The commonly utilised method to address residual stresses in LPBF parts is the principle of stress-relief heat treatment, where fabricated objects, usually still attached to the build plate and support structures, are placed in a furnace and heated for a period of time and then allowed to uniformly cool [59]. This process aims to resolve the stresses between the individual layers of a part by allowing them to cool from the same starting temperature uniformly [56]. Depending on the application, the objects are then annealed, tempered, hardened, or age-hardened to achieve the desired mechanical properties [48], [58], [60].

2.5.3 Ti-6Al-4V

Ti-6Al-4V (Ti64) is a two-phase titanium-aluminium-vanadium alloy primarily consisting of close-packed alpha and body-centred cubic beta phases applied in aerospace, energy, and biomedical industries due to its excellent mechanical

© Central University of Technology, Free State

properties [61]. It has exceptional corrosion resistance, specific strength, ductility, and biocompatibility when compared to other AM materials [61], [62]. Ti64 can have several different microstructure shapes depending on the heat treatment and post-processing [63] and has a large array of applications [61]. This study made use of an Electro Optical Systems GmbH (EOS) Ti64-Grade 23 powder, which is an alloy produced by EOS and is typically processed in an EOS M290 direct metal laser sintering (DMLS) system. It is classified as a Grade 23 titanium alloy according to the ASTM B348, which governs annealed titanium as applied to bars and grills [64].

When a part is manufactured using the recommended process parameters on an EOS M290 DMLS system and heat-treated as recommended by the EOS Grade 23 material datasheet [64], the material will have a vertical yield strength of 1 020 MPa, and a horizontal yield strength of 1 000 MPa, as indicated in Table 1.

Table 1: Material properties of TI64-grade 23 [64]

	Vertical	**Horizontal**
Tensile strength	1 110 MPa	1 100 MPa
Yield strength	1 020 MPa	1 000 MPa
Elongation at break [%]	15	15
Reduction of area [%]	≥ 25	≥ 25

The heat treatment of Ti64 is important as the stress-relief process directly affects the α + β microstructure of the material which determines its mechanical properties. In the case study of Cao et al. [65], a series of Ti64 test pieces were heat-treated at various temperatures and soaking times. The progression of their sample microstructures at different temperatures in Figure 20, shows how the microstructure changed under various temperatures and the durations of their heat treatments.

© Central University of Technology, Free State

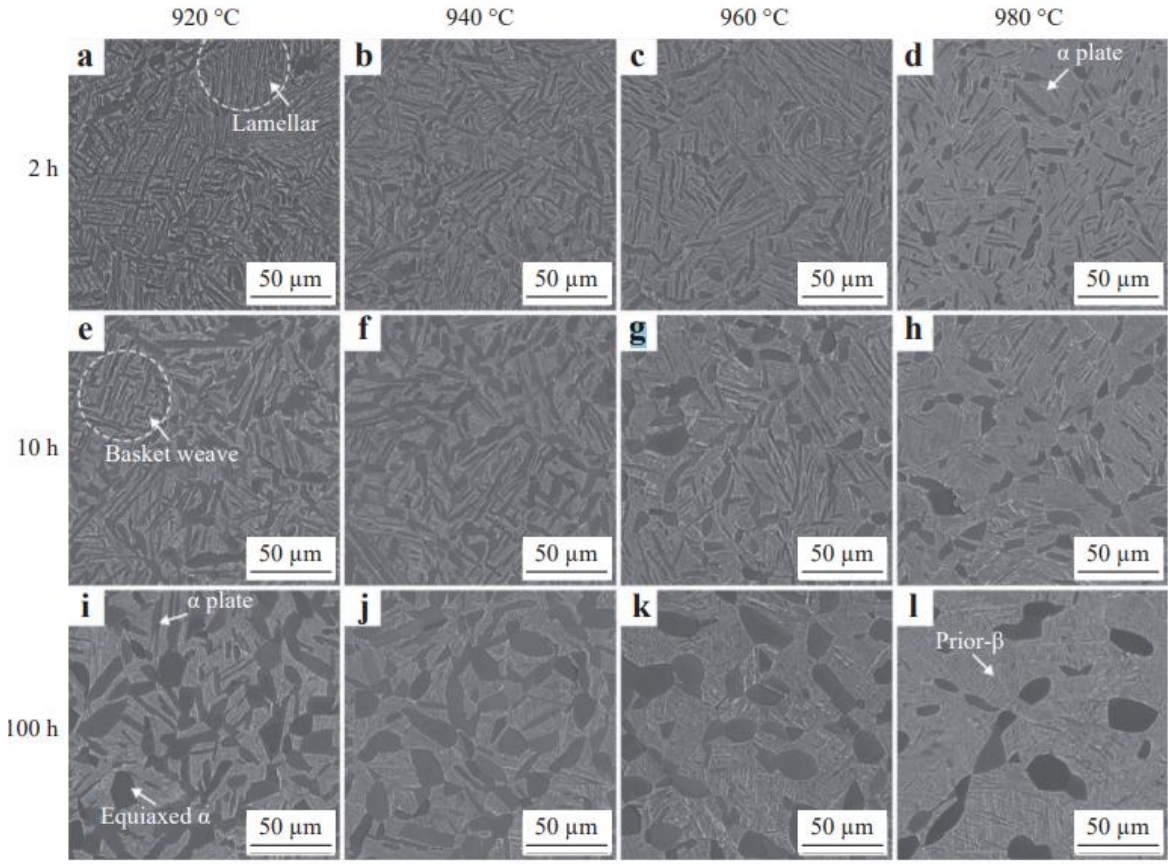

Figure 20: Heat-treatment effect on microstructure [65]

Cao et al. [65] concluded that a finer α microstructure resulting from a shorter period of heat-treatment processes, under 10 hours, generally showed an improvement in strength at the cost of low ductility and poor fracture resistance. Conversely, Cao et al. [65] also concluded that a coarser α + β microstructure resulting from longer periods of heat treatments, up to 100 hours, showed higher fracture toughness and creep resistance at the cost of strength. Therefore, due to the variable effect that heat treatments have on the properties of LPBF Ti64, standard heat treatments may not necessarily produce the desired microstructures as the LPBF process parameters affect the starting microstructures of the material [64]. To avoid this issue, it is highly recommended to consult the relevant material datasheets for both the specific LPBF system and material manufacturer for information on the correct processing parameters and the recommended heat-treatment process. EOS recommends that Ti64-Grade 23 powder undergo stress-relief heat treatment for 120 minutes at 800 °C in a partial vacuum, followed by cooling under vacuum or argon quenching to achieve the correct material properties.

© Central University of Technology, Free State

Another aspect that affects the quality and lifespan of AM parts is surface roughness, with as-built components manufactured using LPBF typically having a rough surface finish [65]. Figure 21 shows the side surfaces (a) and the top surfaces (b) taken with an electron microscope in the case study of Khalid Rafi et al. [66]. As can be seen in Figure 21, substantial balling is present on side surfaces due to unfused powder, and a notable staircase effect is visible on the upper surfaces [66].

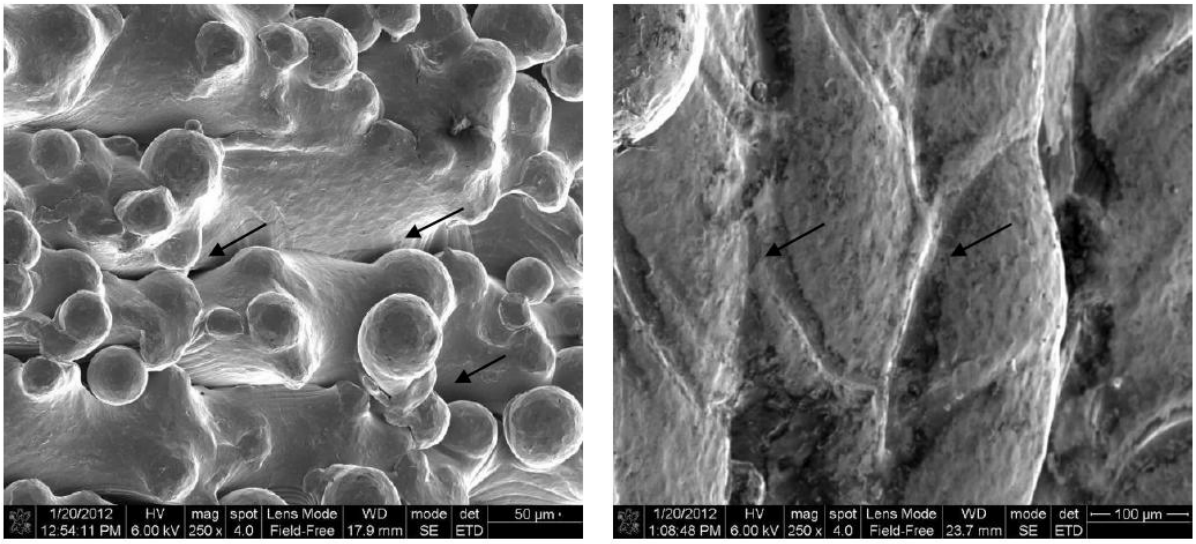

Figure 21: Side (a) and top (b) surfaces of as-built Ti64 sample [66]

To address these issues, a combination of surface treatments, including blasting, shot peening, machining, or electro-polishing, may be employed to reduce surface roughness [65].

© Central University of Technology, Free State

2.5.4 LPBF heat exchangers

During the case study of Venter and Jacobs [67], compact cross-flow heat exchangers, designed using the Kays and London method, were manufactured with the LPBF process. A primary example is a water-to-water heat exchanger (Figure 22), which was manufactured on an EOS M290 DMLS system utilising Ti64 as material.

Figure 22: Water-to-water Ti64 heat exchanger [67]

However, several points of interest were identified during their work, which is of importance to this study. First, the complexity of the internal structures within a heat exchanger could affect the quality of the LPBF process, with finer channels being prone to blockages or anomalies that were difficult to rectify [5]. A micro-CT scan of the internal channels of a heat exchanger manufactured using LPBF is indicated in Figure 23, showing powder blockages within the channels.

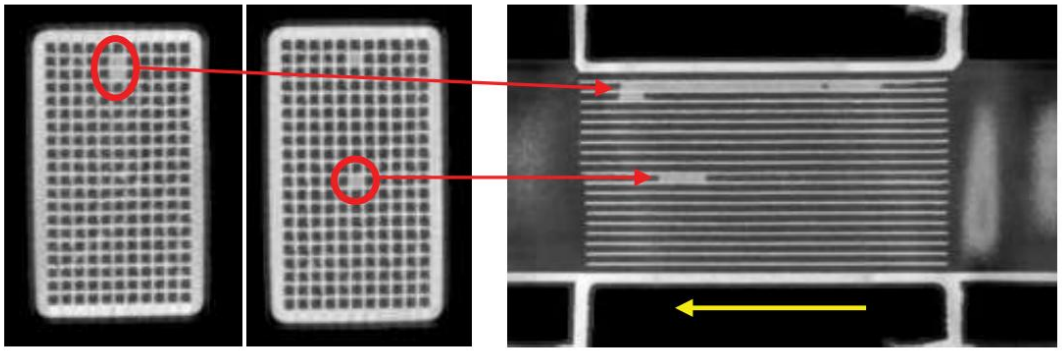

Figure 23: Top, bottom, and side micro-CT scans of fine heat exchanger channels

Second, straight channels showed high levels of stress build-up during the build process, which, when released during the stress-relief process, would undergo

© Central University of Technology, Free State

notable warping due to a lack of support [5]. An example of this effect can be clearly seen in Figure 24, where a set of straight channels underwent warping during the LPBF process due to a combination of factors, notably lack of support, build direction, and channel length [5].

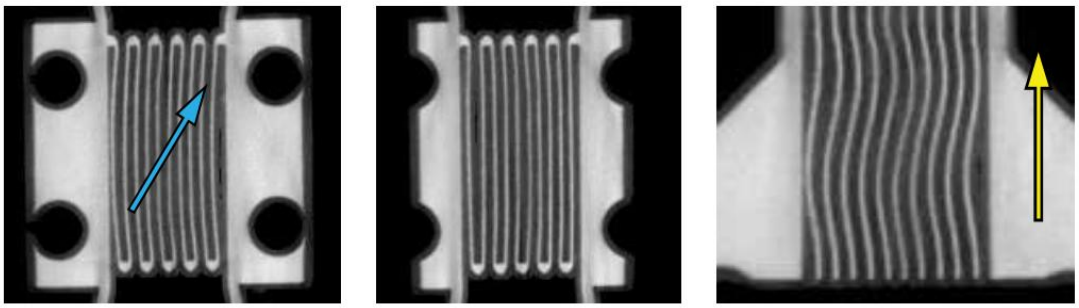

Figure 24: Bottom, top, and side micro-CT scans of long heat exchanger channels

It can be concluded that Ti64 heat exchangers can be produced on an EOS M290 DMLS system; however, the design and build orientation of any manufactured heat exchangers will be important. It is recommended to avoid fine passages, which could cause blockages or long unsupported channels that could distort during manufacturing.

2.6 Chapter summary

From the literature reviewed in the chapter, a wide variety of topics and concepts were covered relating to the installation of post-compression intercooling modifications in aeronautical turboshaft engines.

The following topics were addressed and reviewed:

- An understanding of the operating principles behind turboshaft engines and their applications in the realm of aeronautics.
- The design and manufacturing of heat exchangers based on the ε -NTU and Kays and London method.
- Principles behind DA and DS for use in experimentally verifying scale models.
- AM principles as applied to the LPBF printing of Ti64 parts and heat exchangers.

© Central University of Technology, Free State

From the literature reviewed, there may be benefits found in the installation of an intercooler system into a turboshaft engine with the aim of cooling charge air supplied by a compressor stage. Nada [32] found that the installation of an intercooler system into turboshaft engines generally showed an improvement in performance at the cost of a minor reduction in efficiency. Such modifications could enhance the overall power output from the system by increasing the density of air supplied by the compressor stages of the turboshaft engine. Additionally, colder air entering the combustor unit may improve containment and regulation of the combustion process within the combustor unit, leading to better engine temperatures. However, several drawbacks were also noted, as reviewed under 2.4.2, with the installation of the desired intercooler system directly affecting the thermal efficiency of the engine, which could result in an increase in the SFC. Of additional concern was the reduction in the temperature of air supplied to the combustor unit, which could negatively affect the gas emissions of the engine.

Venter and Jacobs [67] found that heat exchangers could be designed using Ti64 as a material if proper design considerations were made prior to manufacturing, with care taken to avoid powder blockages and warping during heat treatment. Sánchez-Escalona et al. [37] created dimensionless number groups via DA techniques, which can be used to experimentally verify a heat exchanger. It can be concluded that the concept of using Ti64 as a material in LPBF heat exchangers has merit and can be experimentally verified.

© Central University of Technology, Free State

CHAPTER 3

Methodology

The aim of this chapter is to address the methodology used to achieve the objectives of this study.

3.1 Research approach

To achieve the objectives listed in Chapter 1, the following research approach was followed:

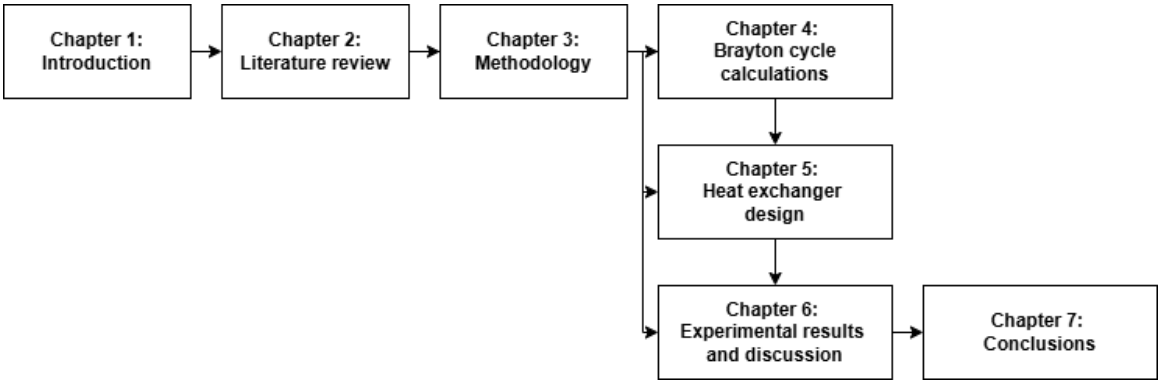

Figure 25: Research approach utilised in this study

3.2 Benchmarking

To achieve realistic results in this study, the starting benchmark engine is assumed to be approximate to the performance specifications of a commercial Robinson R66 helicopter. Robinson [68] states that the R66 Turbine helicopter uses a reverse flow can-annular turboshaft engine, where the compressor and combustor unit are separated by connecting air ducts (Figure 26).

© Central University of Technology, Free State

Figure 26: Robinson R66 turbine helicopter turboshaft engine [68]

The benchmark engine for the study is classified as a twin-spool free power turbine consisting of a single-stage centrifugal compressor, a reverse flow can-annular combustor, a two-stage HPT, and a two-stage FPT, capable of a continuous power output of 224 kW at a pressure ratio of 6.2 [13], [68], [69]. The technical specifications for the baseline engine are set out in Table 2, showing the characteristics of the engine as well as the continuous power output and pressure ratio.

Table 2: Benchmark engine specifications [13], [69]

Power (kW)	224 continuous
Pressure ratio	6.20
Length (m)	0.955
Basic weight (kg)	91.63
Compressor	1 centrifugal high pressure compressor
Turbine	2-stage high power turbine, 2-stage free power turbine

A breakdown of the individual components used in the benchmark engine is shown in Figure 27 a) and b) [13].

© Central University of Technology, Free State

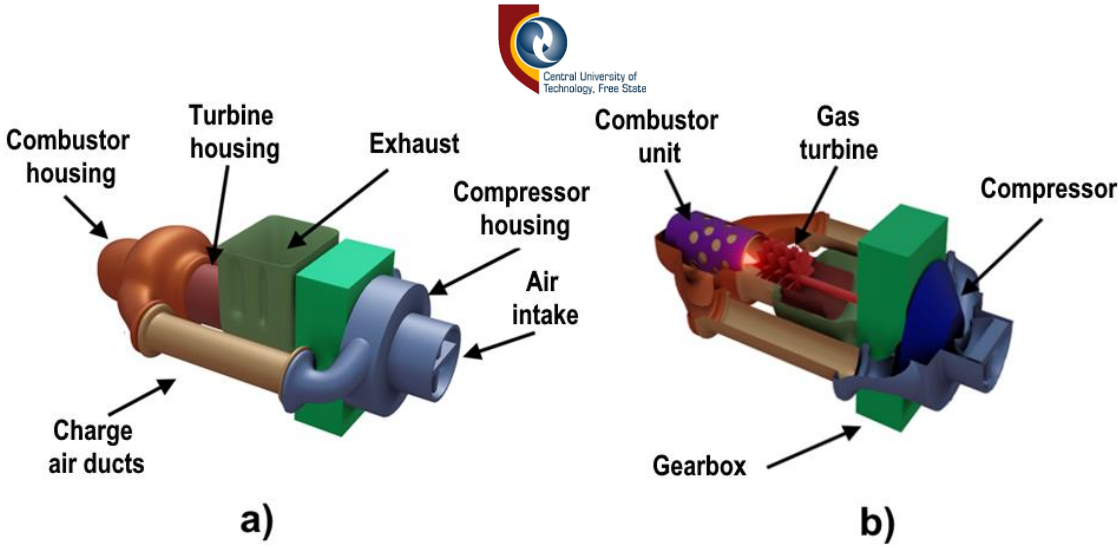

Figure 27: a) Simplified turboshaft model, b) cross-sectional view (illustration by author)

The air ducts in indicated in Figure 27 a) and b) serve to redirect and reverse the direction of the air supply as it is directed from the compressor stage to the combustor unit (Figure 28).

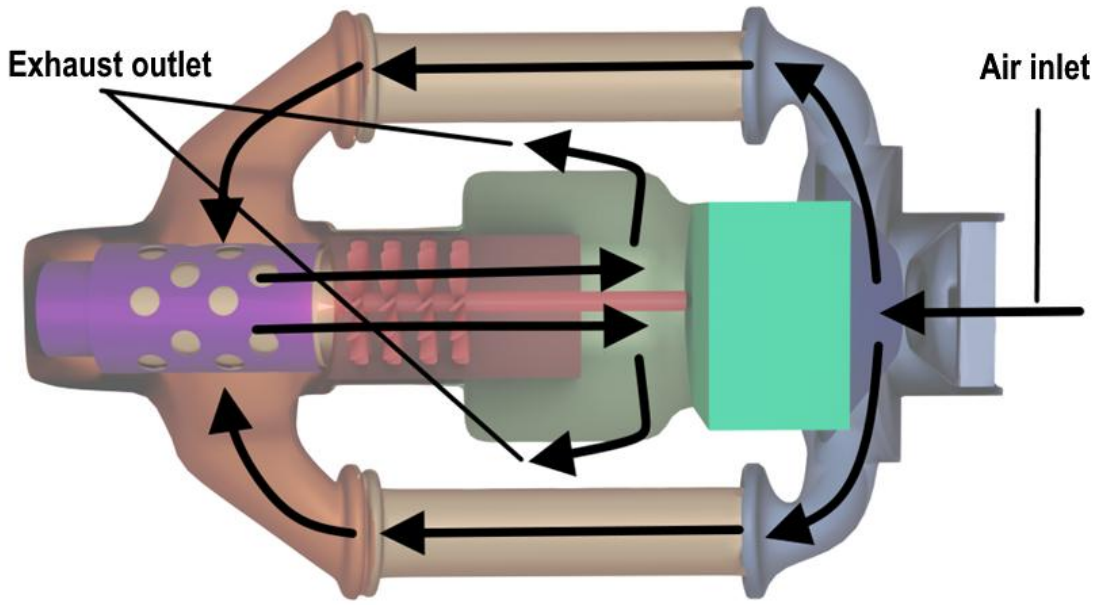

Figure 28: Airflow diagram (illustration by author)

A possible method to implement the hypothesised system is to replace the air ducts, which supply charge air to the combustor unit, with two heat exchangers capable of fulfilling the roles of the intercooler, as proposed in Figure 29.

© Central University of Technology, Free State

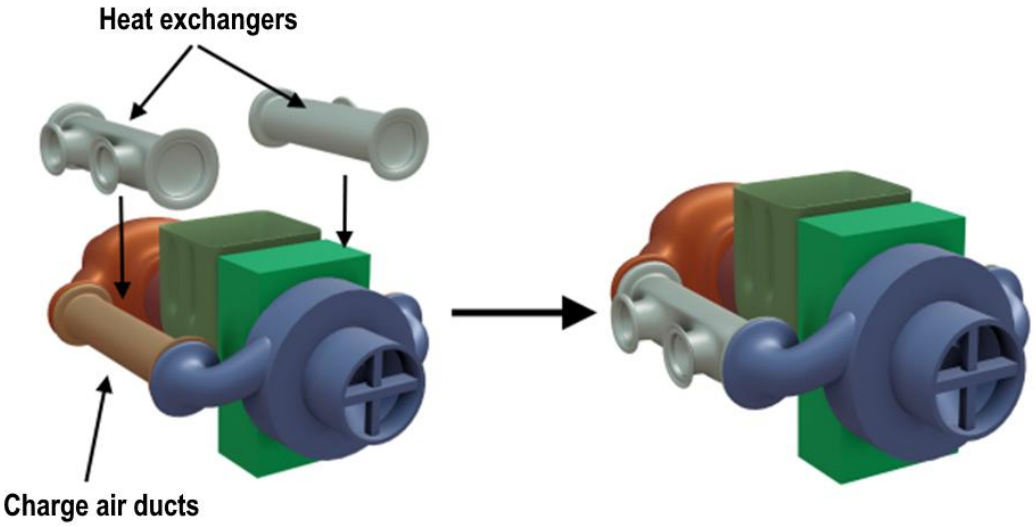

Figure 29: Installation of heat exchangers into the engine (illustration by author)

The following assumptions were then made to aid in the development of the mathematical model of the selected benchmark engine:

- The benchmark engine for this study was based on a purely theoretical model.
- The external atmosphere was assumed to be the International Standard Atmosphere model wherever applicable.
- The Brayton cycle assumes a steady one-dimensional compressible flow, that the working fluid is a perfect gas, and that the gas expansion and compression processes are isentropic in nature.

The Brayton cycle model this study used was obtained from El-Sayed [11] and was verified using Dixon & Hall [8]. This cycle could be used to calculate the pressure and temperature of the working gas as it passes through each of the different stages of the benchmark engine, as well as the calculation of unknown variables such as the temperature and pressure of the air passing through the system and the mass flow rate of the engine. Implementing the assumptions, the Brayton cycle for the benchmark engine layout depicted in Figure 30 can be plotted on the Temperature-Entropy diagram depicted in Figure 31. This shows the process by which air passes through the air intake from the atmosphere, then through the compressor stage up to the pressure ratio of 6.2, undergoes combustion in the combustor unit, the exhaust gas passes through the HPT, which drives the

© Central University of Technology, Free State

compressor, and lastly, the gas passes through the FPT before being expelled into the atmosphere.

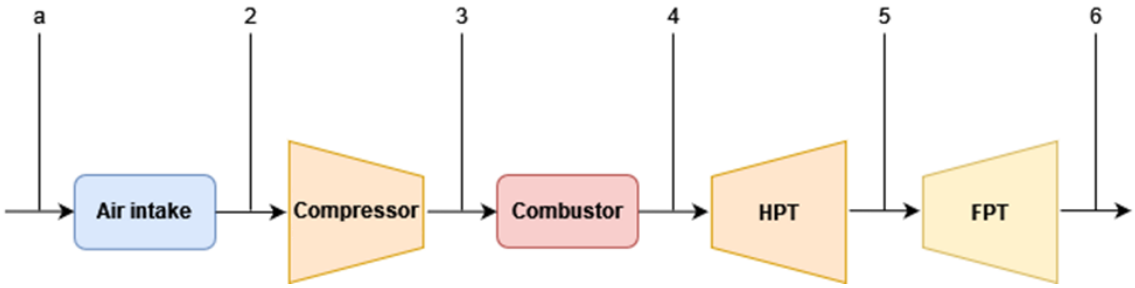

Figure 30: Benchmark engine layout (illustration by author)

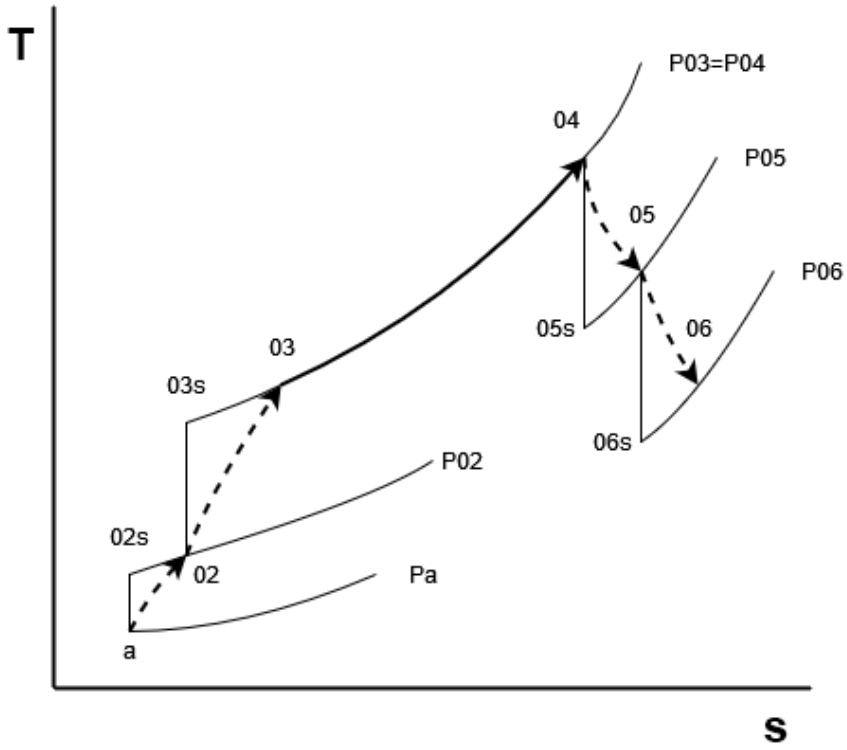

Figure 31: Temperature-Entropy diagram for benchmark engine (illustration by author)

Starting assumptions

Because there are numerous challenges involved in developing the theorised intercooler system, the following assumptions were made to assist in containing the scope of the study.

1. The intercooler system would consist of two separate heat exchangers replacing the two air ducts that lead air from the compressor to the combustor unit which would be cooled by two independent cooling fans, as indicated in Figure 32.

© Central University of Technology, Free State

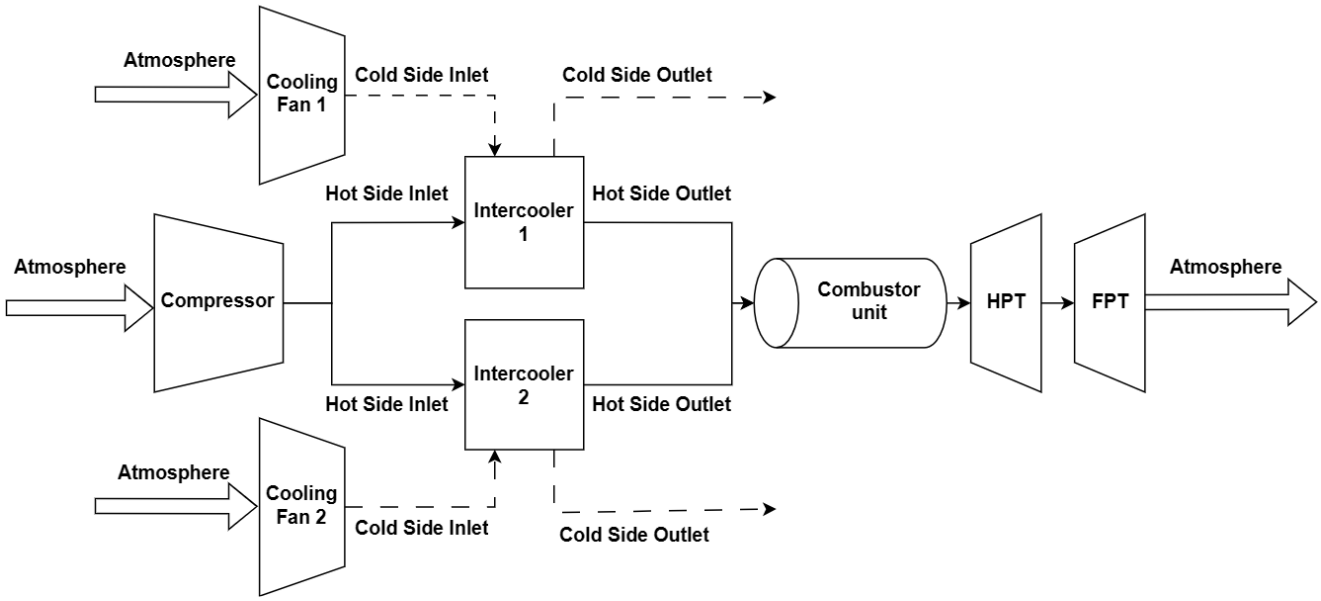

Figure 32: Proposed intercooler layout (illustration by author)

2. The volume of the heat exchanger units would be limited to the amount of space available between the air ducts.
3. The full-scale intercooler design would use Ti64 titanium alloy to ensure continuity with any test pieces manufactured via AM.
4. The geometry of the full-size heat exchanger would be scalable to allow for AM at half scale.
5. The overall pressure drop across the intercooler units would be minimised wherever possible because a substantial pressure drop could result in a choking effect, which could harm the performance of the benchmark engine.

Unknown variables

Before the intercooler system could be designed, several unknown variables were present at the beginning of the design phase which had to be addressed. These variables were:

1. The temperature and mass flow rate of the air passing through the compressor unit of the benchmark engine were unknown. Figure 33 indicates how a basic Brayton gas cycle is used to estimate the performance characteristics of the benchmark engine to calculate the inlet pressure, inlet temperature, and mass flow rate to fulfil the design requirements for the hot side of the heat exchanger.

© Central University of Technology, Free State

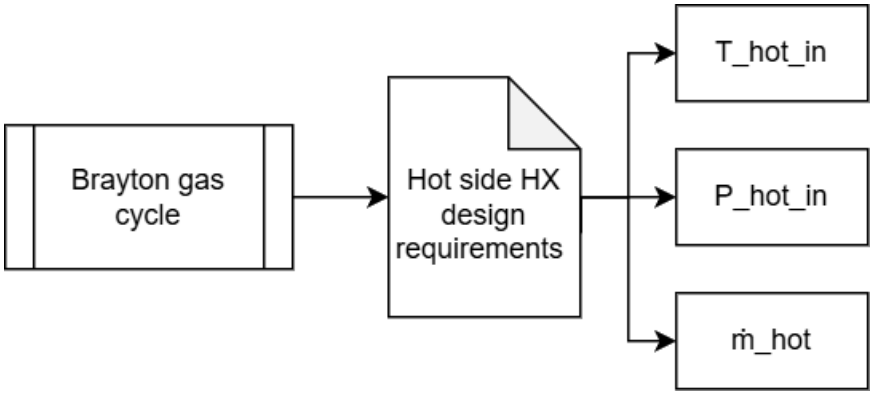

Figure 33: Hot side parameters

2. The cooling fluid for the system was assumed to be air supplied at atmospheric conditions via a set of two 150 mm 54 W axial-flow fans capable of supplying an airflow of 480m^3/h each [70]. This assumption was made because the intercooler system required an external cooling source, the design of which was deemed outside the scope of this project. From these assumptions, the inlet pressure, inlet temperature, and mass flow rate for the cold side fluid were calculated. A flow chart of this process is set out in Figure 34.

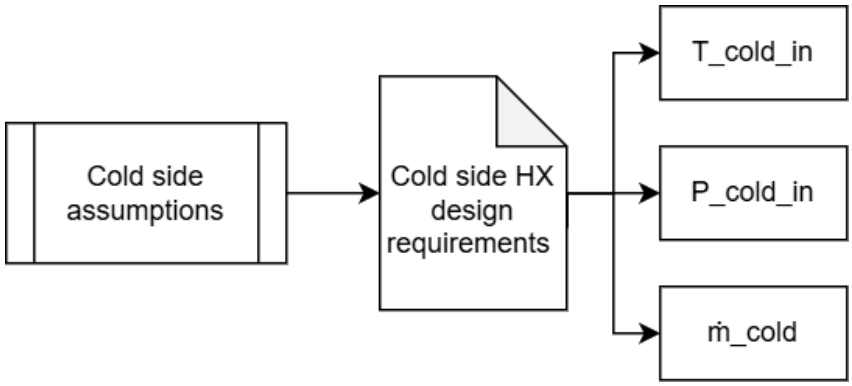

Figure 34: Cold side parameters

© Central University of Technology, Free State

Heat exchanger design

After evaluation of the unknown variables for both the hot and cold sides, a theoretical heat exchanger could be designed that would meet the requirements of this study. It was assumed that the system would consist of two separate heat exchanger units, with each being able to handle half of the total load on the system. A single unit could be designed that was capable of cooling half of the total mass flow rate from the compressor. As was discussed during the literature review, Shah and Sekulic [35] proposed an iterative process based on the prior work by Kays and London [34], which can be used to calculate the exit parameters for a specific heat exchanger using only the input parameters and size. This methodology estimates the effectiveness of the heat exchanger using collected experimental data in the form of data charts, which were then used to calculate the actual effectiveness of the heat exchanger. The estimated and actual effectiveness of the heat exchanger were compared, and if there was a variance in the estimated and actual values, a new iteration was performed using the actual efficiency obtained from the previous iteration. After several iterations were performed, the estimated and actual effectiveness were expected to converge. Once convergence had been achieved, the design phase could proceed to the pressure drop analysis stage of the process. A flowchart explaining this methodology is illustrated in Figure 35, which shows how input parameters such as temperature, pressure, and flow rate could be used to estimate the performance of the heat exchanger. Using this iterative process, the theoretical performance for the full-size heat exchanger design was obtained using the limited data available from the benchmark engine.

© Central University of Technology, Free State

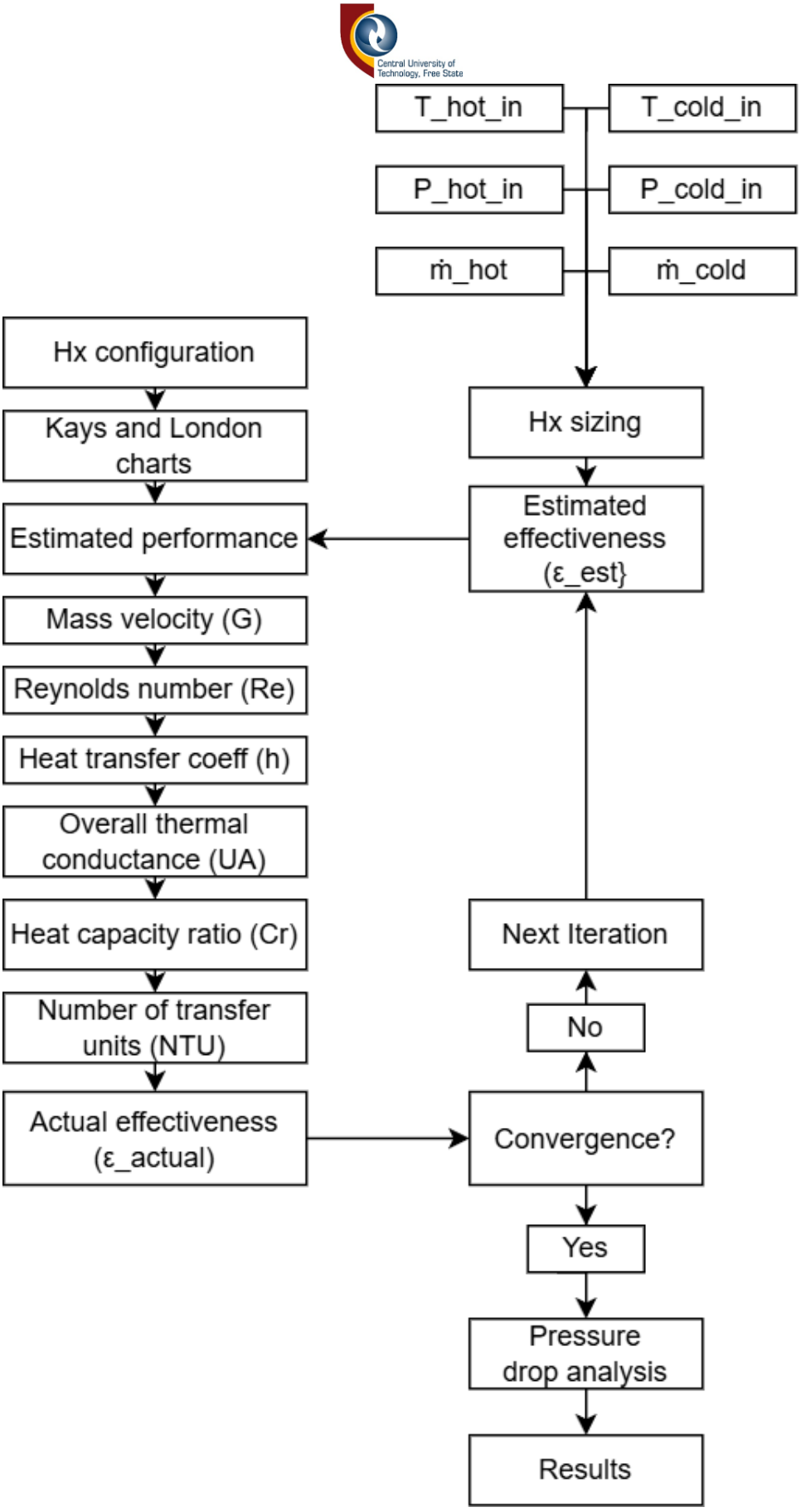

Figure 35: Shah and Sekulic iterative heat exchanger design process

© Central University of Technology, Free State

3.3 Single-passage heat exchanger design

Due to concerns regarding the potential cost involved in prototyping and experimentally testing the full-size heat exchanger system, it was decided that a single passage would be extracted from the full-size design, which could then be manufactured at the desired scale and tested using compressed air. This process is illustrated in Figure 36 showing how a segment could be extracted from a larger heat exchanger design.

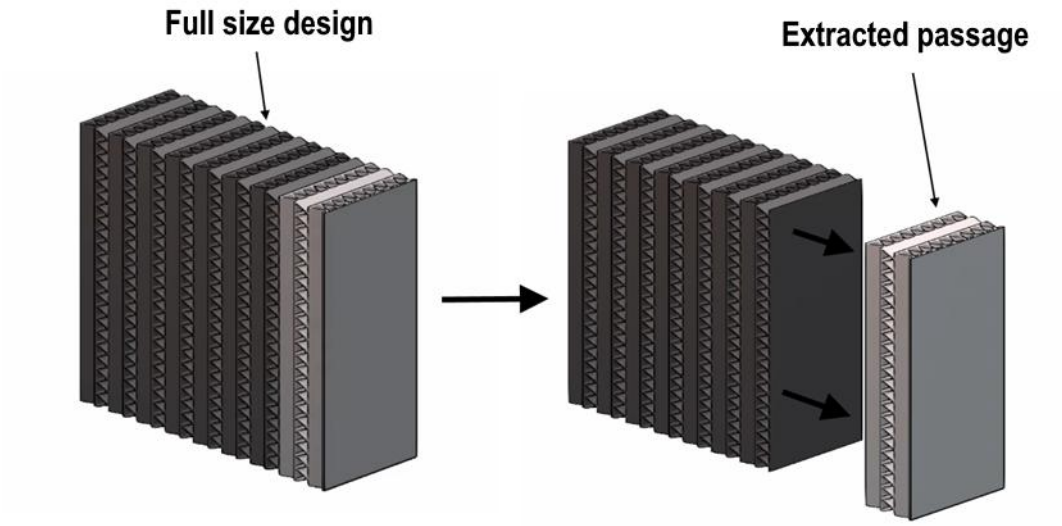

Figure 36: Single-passage segment extraction process

The proposed iterative design process for the heat exchanger was then repeated for the extracted single-passage segment, which allowed for the expected performance of the single-passage segment to be obtained. It should be noted that the testing of an extracted segment was expected to provide less accurate results compared to a full-size design; however, considering the risk of failure involved in manufacturing LPBF heat exchangers, a smaller test piece was found to be justifiable.

3.4 Test-piece heat exchanger

For the experimental testing phase of the project, the scaled test-piece heat exchanger would need to be experimentally verified using compressed air. To reduce the flow rate of air required to verify the test piece, a scale factor of 50% was selected.

© Central University of Technology, Free State

Once the parameters for the full-scale single-pass heat exchanger were calculated, it was scaled down by 50% to serve as the test piece.

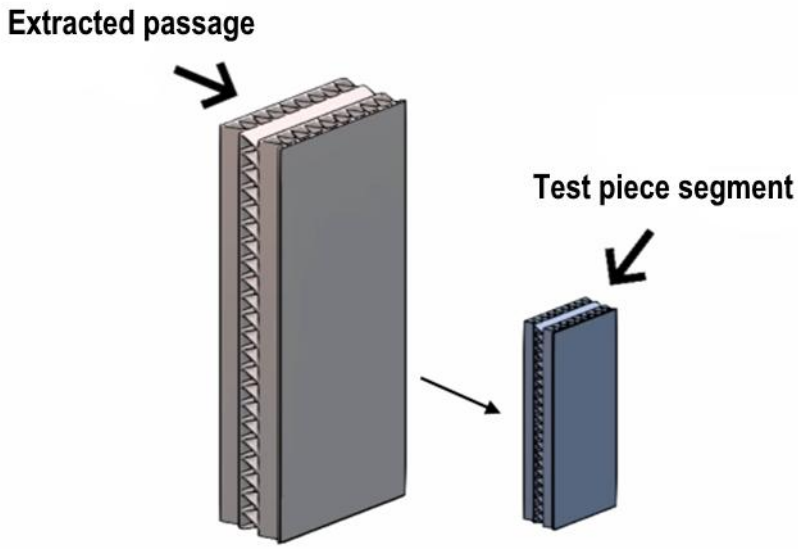

Figure 37: Scaling process

The scaling process allowed for the successful production of the test piece segment on an EOS M290 LPBF system at the Centre for Rapid Prototyping and Manufacturing (CRPM) in Bloemfontein, South Africa. The connecting manifolds were then manufactured at the Product Development Technology Station (PDTS) in Bloemfontein from an aluminium billet, with gasket seals used to seal the manifolds against the test-piece heat exchanger.

3.5 Experimental methodology

Using the DA research performed by Sánchez-Escalona et al. [37], similarity could theoretically be established between the experimental test-piece segment and the full-scale design, which allowed the project to proceed to the experimental phase. For kinematic similarity parameters to be met, the model would need to be tested under the specific conditions that were required to match DS conditions. As a result, a test bench capable of simulating the necessary conditions was fabricated.

The required test bench consisted of the following components, as indicated in Figure 38:

1. One air supply heating unit (1500 Watts).

© Central University of Technology, Free State

2. Two pressure regulation valves at the hot and side inlet (0.5-12 Bar)
3. Gas volumetric flow gauge for the hot side (300 LPM).
4. Gas volumetric flow gauge for the cold side (140 LPM).
5. Four temperature gauges to measure the temperature of the working fluids at the test-piece inlet and outlet (120 °C).
6. Four pressure gauges to measure the pressure of the working fluids at the test-piece inlet and outlet (12 Bar)
7. Flow regulation valve at hot side outlet (10 Bar).

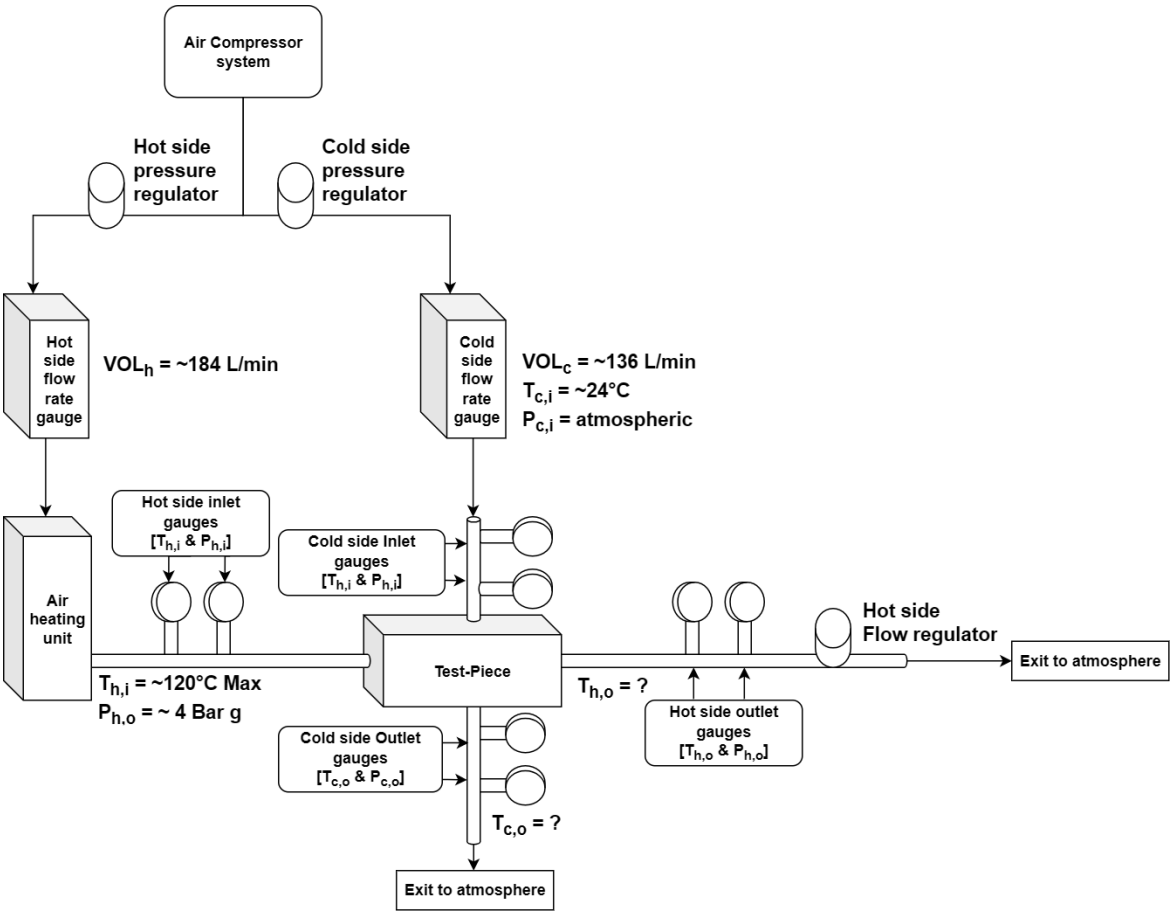

Figure 38: Test bench schematic

3.6 Results

After completion of the experimental phase of the project, the performance of the single-passage heat exchanger design was validated via the test piece. Conclusions were then made concerning the possible efficacy of the full-size design when applied to turboshaft engines. A simple flow chart of this process is illustrated in Figure 39.

© Central University of Technology, Free State

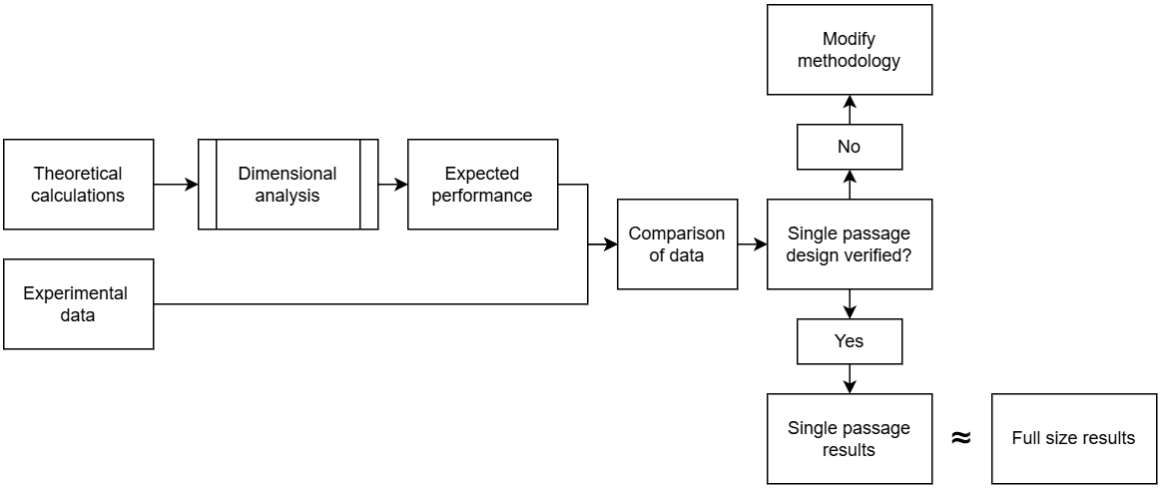

Figure 39: Process to reach results from data

3.7 Chapter Summary

In this chapter, the approach used to begin the design process for the intercooler system was laid out. Firstly, the specifications used to benchmark the turboshaft engine were selected from the literature, and the process by which the intercooler system could be feasibly installed into the benchmark engine was described. The process by which the test piece would be extracted from the full-size design and the required components for the test bench was evaluated, and the process by which the experimental results would be used to verify the efficacy of the full-scale design was laid out.

© Central University of Technology, Free State

CHAPTER 4

Benchmark Engine Characterisation

This chapter aims to address the operating characteristics of the benchmark turboshaft engine using a basic Brayton gas cycle.

4.1 Brayton cycle calculations

Before the heat exchanger unit could be designed, the unknown conditions of the air entering the combustor unit had to be determined. These results would then be used to the design requirements for the hot side of the heat exchanger.

Speed of sound

By applying Eq. 4.1, the local speed of sound was calculated from atmospheric conditions.

$$a = \sqrt{yRT_a} \qquad \text{Eq. 4.1}$$

Where:

$y = 1.4$

$R = 287.058$

$T_a = 288.15\ °K$

Thus:

$$a = \sqrt{yRT_a}$$

$$a = \sqrt{1.4 * 287.058 * 288.15}$$

$$a = 340.297\ m/s$$

Mach number

By applying Eq. 4.2, the previously calculated speed of sound was used to obtain the Mach number of the air entering the intake stage. Note that due to the engine being assumed as stationary, this effect will be zero for this data set.

$$M = \frac{c}{a} \qquad \text{Eq. 4.2}$$

Where:

© Central University of Technology, Free State

$c = 0\ km/h$

$a = 340.297\ m/s$

Thus:

$$M = \frac{c}{a}$$

$$M = \frac{0}{3.6 * 340.297}$$

$$M = 0$$

Stagnant temperature at inlet exit

Using Eq. 4.3 [11], the stagnant temperature of the air leaving the air inlet was calculated from atmospheric conditions.

$$T_{02} = T_a\left(1 + \left(\frac{y-1}{2}\right) * M^2\right) \quad \text{Eq. 4.3}$$

Where:

$M = 0$

$T_a = 288.150\ °K$

$y = 1.4$

$a = 340.297\ m/s$

Thus:

$$T_{02} = T_a\left(1 + \left(\frac{y-1}{2}\right) * M^2\right)$$

$$T_{02} = 288.150\left(1 + \left(\frac{1.4-1}{2}\right) * 0^2\right)$$

$$T_{02} = 288.150\ °K$$

Stagnant pressure at inlet exit

Using Eq. 4.4 [11], the stagnant pressure of the air leaving the air inlet was calculated using atmospheric conditions. Eq. 4.4 addresses losses through an air intake by assuming an intake efficiency for the ducts. Therefore, an intake efficiency of 92% was assumed for the air duct.

$$P_{02} = P_a\left(1 + n_d\left(\frac{y-1}{2}\right) * M^2\right)^{\frac{y}{Y-1}} \quad \text{Eq. 4.4}$$

© Central University of Technology, Free State

Where:

$P_a = 101.325\ kPa$

$y = 1.4$

$a = 340.297\ m/s$

$M = 0$

$\eta_d = intake\ efficiency = 0.92$

Thus:

$$P_{02} = P_a\left(1 + \eta_d\left(\frac{y-1}{2}\right) * M^2\right)^{\frac{y}{Y-1}}$$

$$P_{02} = 101.325\left(1 + 0.92\left(\frac{1.4-1}{2}\right) * 0^2\right)^{\frac{1.4}{1.4-1}}$$

$$P_{02} = 101.325\ kPa$$

Stagnant pressure at the compressor exit

After calculating the stagnant pressure of the air leaving the inlet, the pressure ratio of the engine was used via Eq. 4.5 to obtain the stagnant pressure of the air leaving the centrifugal compressor.

$$P_{03} = \pi_c * P_{02} \qquad \text{Eq. 4.5}$$

Where:

$\pi_c = 6.2$

$P_{02} = 101.325\ kPa$

Thus:

$$P_{03} = \pi_c * P_{02}$$

$$P_{03} = 6.2 * 101.325$$

$$P_{03} = 628.215\ kPa$$

Stagnant temperature at compressor exit

Eq. 4.6 [11], was then used to calculate the stagnant temperature of the air leaving the centrifugal compressor. Due to an adiabatic compression process having taken place, an isentropic efficiency of 84% will be assumed for the compressor stage.

© Central University of Technology, Free State

$$T_{03} = T_{02}\left(1 + \frac{\pi_c^{\frac{y_c-1}{y_c}} - 1}{\eta_c}\right) \quad \text{Eq. 4.6}$$

Where:

$\mathbf{T_{02}} = \mathbf{288.15}\ °K$

$y_c = 1.4$

$\pi_c = 6.2$

$\eta_c = 0.84$

Thus:

$$\mathbf{T_{03}} = \mathbf{T_{02}}\left(\mathbf{1} + \frac{\boldsymbol{\pi_c}^{\frac{y_c-1}{y_c}} - \mathbf{1}}{\boldsymbol{\eta_c}}\right)$$

$$\mathbf{T_{03}} = \mathbf{288.15}\left(\mathbf{1} + \frac{\mathbf{6.2}^{\frac{1.4-1}{1.4}} - \mathbf{1}}{\mathbf{0.84}}\right)$$

$$\mathbf{T_{03}} = \mathbf{522.860}\ °\boldsymbol{K}$$

Additionally, the overall temperature rise across the compressor:

$$\Delta\mathbf{T_{compressor}} = \mathbf{T_{03}} - \mathbf{T_{02}}$$

$$\Delta\mathbf{T_{compressor}} = (\mathbf{522.860} - \mathbf{273}) - (\mathbf{288.15} - \mathbf{273})$$

$$\Delta\mathbf{T_{compressor}} = \mathbf{234.710}\ °\boldsymbol{C}$$

Stagnant temperature at combustor unit exit

It was assumed that the stagnant temperature of the air leaving the combustor unit was the same as the gas temperature limitations of the gas turbine stages. For the benchmark engine, as applied in a Robinson R66 helicopter, the maximum continuous gas temperature under normal operating conditions for the turbine stages is 706 °C [69].

$$\mathbf{T_{04}} = \mathbf{706} + \mathbf{273} = \mathbf{979}\ °\mathbf{K}$$

Stagnant pressure at the combustor unit exit

For a real-world turboshaft engine, a minor pressure drop will be present across the combustor unit. Eq. 4.7 [11], was used to account for this pressure loss via an assumed 4% pressure drop across the combustor unit.

© Central University of Technology, Free State

$$P_{04} = (1 - \Delta P_{combustor}) * P_{03}$$ Eq. 4.7

Where:

$\Delta P_{combustor} = 0.04$

$P_{03} = 628.215\ kPa$

Thus:

$$P_{04} = (1 - \Delta P_{combustor}) * P_{03}$$

$$P_{04} = (1 - 0.04) * 628.215$$

$$P_{04} = 603.086\ kPa$$

Air-to-fuel ratio inside the combustor unit

Eq. 4.8 [11], could then be used to approximate the air-to-fuel ratio inside the combustor unit. In accordance with [11], a calorific value of 42.798 MJ/kg was assumed for the Jet A1 grade fuel, as well as an efficiency of 98% for the combustor unit.

$$f = \frac{(Cp_h * T_{04}) - (Cp_c * T_{03})}{(\eta_b * Q_R) - (Cp_h * T_{04})}$$ Eq. 4.8

Where:

$Cp_c = 1.005\ kJ/kg$

$Cp_h = 1.148\ kJ/kg$

$T_{04} = 979\ °K$

$T_{03} = 522.860\ °K$

$Q_R = 42.798\ MJ/kg$

$\eta_b = 0.98$

Thus:

$$f = \frac{(Cp_h * T_{04}) - (Cp_c * T_{03})}{(\eta_b * Q_R) - (Cp_h * T_{04})}$$

$$f = \frac{(1.148x10^3 * 979) - (1.005x10^3 * 522.860)}{(0.98 * 42.798x10^6) - (1.148x10^3 * 979)}$$

$$f = 14.661x10^{-3}$$

© Central University of Technology, Free State

Stagnant temperature at the HPT exit

Using Eq. 4.9 [11], the stagnant temperature of the gas leaving the HPT stage could be calculated. To account for mechanical losses, an efficiency of 95% was assumed for the compressor HPT assembly.

$$T_{05} = T_{04} - \frac{Cp_c(T_{03} - T_{02})}{\eta_m(1+f)Cp_h} \quad \text{Eq. 4.9}$$

Where:

$\mathbf{Cp_c = 1.005\ kJ/kg}$

$\mathbf{Cp_h = 1.148\ kJ/kg}$

$\mathbf{T_{04} = 979\ °K}$

$\mathbf{T_{03} = 522.860\ °K}$

$\mathbf{T_{02} = 288.15\ °K}$

$\boldsymbol{\eta_m = 0.95}$

$\boldsymbol{f = 14.661x10^{-3}}$

Thus:

$$T_{05} = T_{04} - \frac{Cp_c(T_{03} - T_{02})}{\eta_m(1+f)Cp_h}$$

$$T_{05} = 979 - \frac{1.005x10^3(522.860 - 288.15)}{0.95(1+14.661x10^{-3})1.148x10^3}$$

$$T_{05} = 765.837\ °K$$

Stagnant pressure at the HPT exit

Using Eq. 4.10 [11], the stagnant pressure of the gas leaving the HPT stage could be obtained. Due to an adiabatic expansion process having occurred, an isentropic efficiency of 86% was assumed for the stage.

$$\frac{P_{05}}{P_{04}} = \left(1 - \frac{1}{\eta_{gt}}\left(1 - \frac{T_{05}}{T_{04}}\right)\right)^{\frac{y_h}{y_h - 1}} \quad \text{Eq. 4.10}$$

Where:

$\mathbf{P_{04} = 603.086\ kPa}$

© Central University of Technology, Free State

$\mathbf{T_{04}} = \mathbf{979\ °K}$

$\mathbf{T_{05}} = \mathbf{765.837\ °K}$

$\boldsymbol{\eta_{gt}} = \mathbf{0.86}$

$\boldsymbol{y_h} = \mathbf{1.333}$

Thus:

$$\boldsymbol{P_{05} = P_{04}\left(1 - \frac{1}{\eta_{gt}}\left(1 - \frac{T_{05}}{T_{04}}\right)\right)^{\frac{y_h}{y_h - 1}}}$$

$$\boldsymbol{P_{05} = 603.086\left(1 - \frac{1}{0.86}\left(1 - \frac{765.837}{979}\right)\right)^{\frac{1.333}{1.333-1}}}$$

$$\boldsymbol{P_{05} = 187.439\ kPa}$$

Temperature at the FPT exit

Having calculated all unknown variables up to the FPT stage, Eq. 4.11 [11], was used to calculate the temperature of the exhaust gas leaving the engine.

$$\boldsymbol{T_6 = T_{05}\left(1 - \eta_{ft}\left(1 - \left(\frac{P_6}{P_{05}}\right)^{\frac{y-1}{y}}\right)\right)} \qquad \text{Eq. 4.11}$$

Where:

$\mathbf{P_6 = P_a = 101.325\ kPa}$

$\mathbf{P_{05}} = \mathbf{187.439\ \ kPa}$

$\mathbf{T_{05}} = \mathbf{765.837\ °K}$

$\boldsymbol{\eta_{ft}} = \mathbf{0.86}$

$\boldsymbol{y_h} = \mathbf{1.333}$

© Central University of Technology, Free State

Thus:

$$T_6 = T_{05}\left(1 - \eta_{ft}\left(1 - \left(\frac{P_6}{P_{05}}\right)^{\frac{y_h - 1}{y_h}}\right)\right)$$

$$T_6 = 765.837\left(1 - 0.86\left(1 - \left(\frac{101.325}{184.439}\right)^{\frac{1.333-1}{1.333}}\right)\right)$$

$$T_6 = 672.023\ °K$$

Mass flow rate of air entering combustor

Since the power output from the FPT is known, the mass flow rate of the air entering the combustor unit was calculated via Eq. 4.12 [11].

$$P_{rotor} = \dot{m}_a(1 + f)Cp_h(T_{05} - T_{06}) \qquad \text{Eq. 4.12}$$

Where:

$P_{rotor} = 179\ kW$

$f = 14.661x10^{-3}$

$T_{05} = 765.837\ °K$

$T_6 = 672.023\ °K$

$Cp_h = 1.148\ kJ/kg$

Thus:

$$P_{rotor} = \dot{m}_a(1 + f)Cp_h(T_{05} - T_{06})$$

$$\dot{m}_a = \frac{P_{rotor}}{(1 + f)Cp_h(T_{05} - T_{06})}$$

$$\dot{m}_a = \frac{179x10^3}{(1 + 14.661x10^{-3})1.148x10^3(765.837 - 672.023)}$$

$$\dot{m}_a = 1.638\ kg/s$$

© Central University of Technology, Free State

4.2 Brayton cycle results

Table 3 summarises the calculated parameters obtained from the process which will be used to fill the design requirements for the hot side of the heat exchanger.

Table 3: Brayton cycle results

Specific heat ratio of air ($\boldsymbol{y}$)	$\mathbf{1.4}$
Universal gas constant of air ($\boldsymbol{R}$)	$287.058\ J/kg \cdot K$
Speed of sound ($\boldsymbol{a}$)	$340.297\ m/s$
Intake efficiency ($\boldsymbol{\eta_d}$)	0.92
Compressor isentropic efficiency ($\boldsymbol{\eta_c}$)	0.84
Gas turbine efficiency ($\boldsymbol{\eta_{gt}}$)	0.86
Gas turbine efficiency ($\boldsymbol{\eta_m}$)	0.95
Atmospheric temperature ($\boldsymbol{T_a}$)	$288.150\ °K$
Atmospheric pressure ($\boldsymbol{P_a}$)	$101.325\ kPa$
Inlet outlet temperature ($\boldsymbol{T_{02}}$)	$288.150\ °K$
Inlet outlet pressure ($\boldsymbol{P_{02}}$)	$101.325\ kPa$
Compressor outlet temperature ($\mathbf{T_{03}}$)	$522.860\ °K$
Compressor outlet pressure ($\mathbf{P_{03}}$)	$628.215\ kPa$
Compressor temperature rise ($\Delta\mathbf{T_{compressor}}$)	$234.710\ °C$
Combustor outlet temperature ($\mathbf{T_{04}}$)	$979\ °K$
Combustor outlet pressure ($\mathbf{P_{04}}$)	$603.086\ kPa$
Air-to-fuel ratio ($\boldsymbol{f}$)	$14.661\text{x}10^{-3}$
HPT outlet temperature ($\mathbf{T_{05}}$)	$765.837\ °K$
HPT outlet pressure ($\boldsymbol{P_{05}}$)	$187.439\ kPa$
FPT outlet temperature ($\boldsymbol{T_6}$)	$672.023\ °K$
Mass flow rate of air ($\boldsymbol{\dot{m}_a}$)	$1.638\ kg/s$

The theoretical Brayton cycle, when applied to the benchmark engine, indicated that the compressor stage would cause an estimated temperature rise of 234.71 °C in the charge air at a mass flow rate of 1.638 kg/s. These were the most important parameters needed to initiate the design process for the heat exchanger. This rise in temperature corroborates the original hypothesis, which states that the temperature rise across the compressor stages of a turboshaft engine could be counteracted by a heat exchanger.

© Central University of Technology, Free State

4.3 Chapter summary

This chapter aimed to determine the required parameters to fulfil the design requirements for the hot side of the heat exchanger, with the most important being the temperature, pressure, and mass flow rate of the air supplied by the compressor stage of the benchmark engine. The simple Brayton gas cycle was successfully applied to the benchmark engine using assumptions for the compression and expansion isentropic efficiencies of the engine, which allowed for the estimated temperature rise in the charge air (234.71 °C) at the operating pressure (628.215 kPa) and mass flow rate (1.638 kg/s) to be determined.

© Central University of Technology, Free State

CHAPTER 5

Heat Exchanger Design

The aim of this chapter is to break down the steps taken to size and characterise the heat exchanger units using the ε-NTU supplemented by Kays and London for designing heat exchangers. It also describes the process of extracting the test piece from the full-size design and manufacturing using LPBF Ti64. The DS conditions necessary to verify the test piece were determined through a series of calculations and the operating conditions for the experimental test bench were taken into account.

5.1 Full-size design

The first assumption to address the design process was the driving dimensions of the heat exchanger unit, where L1 refers to the length of the hot side passages, L2 refers to the length of the cold side passages, while L3 refers to the tile width of the heat exchanger, as indicated in Figure 40. Given the limited space between the compressor and combustor unit of the benchmark engine, the size of the heat exchanger design was assumed not to exceed a total length of 270 mm and a height/width of 220 mm.

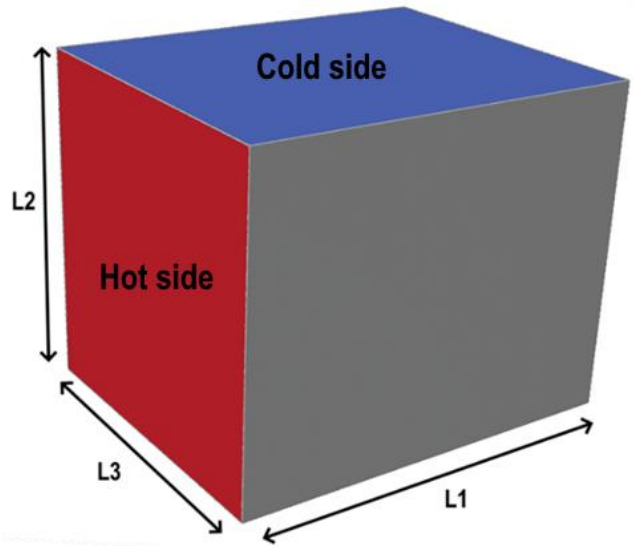

Figure 40: Full-size heat exchanger layout and orientation

For the layout of the heat exchanger, a compact hybrid flow layout was selected in the form of a multi-pass cross-flow setup wherein the cooling fluid would pass multiple times across the hot fluid in succession. This layout was primarily chosen to allow for a smaller test piece segment to be extracted from the design while

© Central University of Technology, Free State

retaining proportionality with the full-size design. Thus, to remain within the initial assumptions for the size of the heat exchanger, a series of three passes was assumed with an L1 length of 90 mm per passage, as indicated in Table 4.

Table 4: Driving dimension of the full-sized heat exchanger

	Pass 1	Pass 2	Pass 3
L1	90 mm	90 mm	90 mm
L2	220 mm	220 mm	220 mm
L3	220 mm	220 mm	220 mm

Figure 41 indicates the proposed layout where the hot side fluid passes through a long, uninterrupted channel, and the cold side fluid passes across three times in series in a collinear fashion.

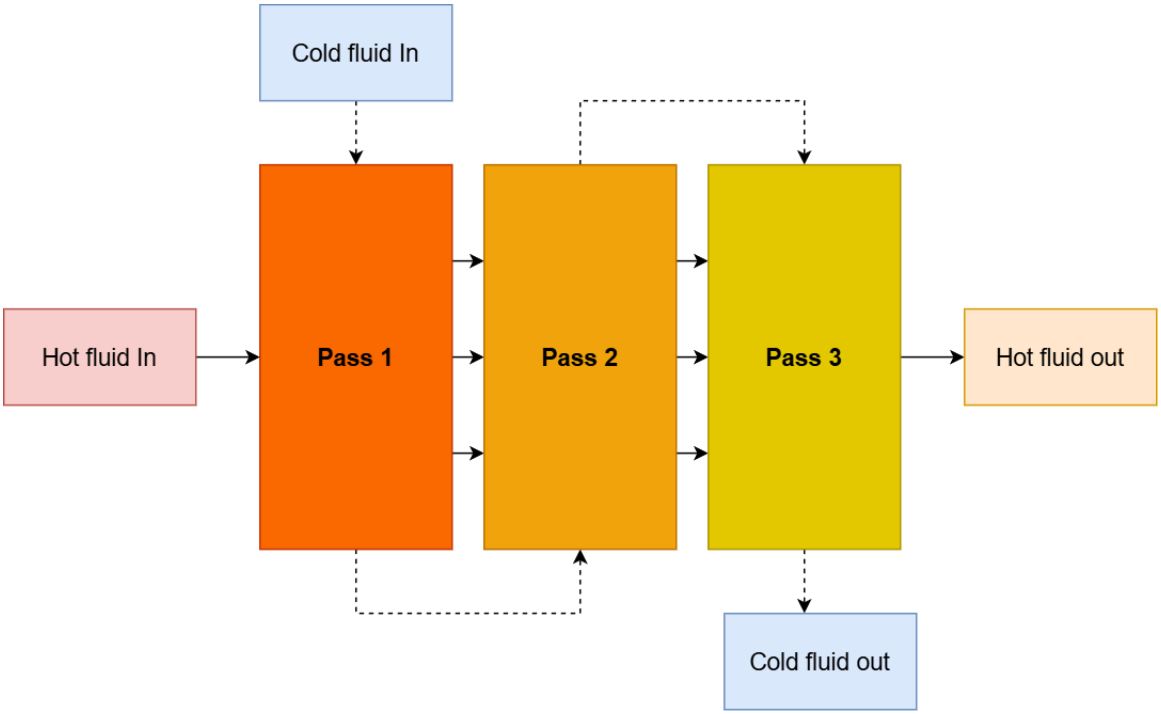

Figure 41: Full-size multi-pass heat exchanger layout

Heat exchanger geometry selection

As the study used data provided by Kays and London [34] to design the heat exchanger using the ε-NTU method, some initial choices regarding the geometry of the mesh had to be made before the design process could continue. As scalability was a primary issue to consider, a suitable mesh was determined to be the plain plate-fin surface 5.3 inch, as provided by Kays and London [34].

© Central University of Technology, Free State

Following several experiments, it was found that if optimally orientated, a heat exchanger made using this geometry on both the hot and cold sides could be manufactured on an EOS M290 LPBF system using Ti-6Al-4V (ELI) without the use of any supporting structures on the internal surfaces. The primary dimensions for the selected mesh are indicated in Figure 42, which shows a wall-to-wall spacing of 12 mm and a fin height of 10 mm.

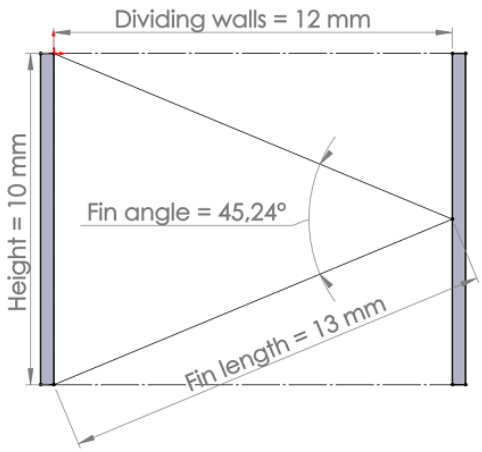

Figure 42: Plain plate-fin surface 5.3 geometry

Table 6 highlights the technical specifications of the mesh, namely the material, plate spacing, fin length, hydraulic diameter, transfer area to volume ratio, fin thickness, and fin area to total area ratio.

Table 5: Plain plate-fin surface 5.3 specifications

Material	Aluminium
Plate spacing ($\boldsymbol{b}$)	12 mm
Fin length ($\boldsymbol{l_f}$)	13 mm
Hydraulic diameter ($\boldsymbol{Dh}$)	6.147E-3 m
Transfer area to volume ratio ($\boldsymbol{B}$)	616.8
Fin thickness ($\boldsymbol{\delta_{fin}}$)	0.152 mm
Fin area to total area ratio ($\boldsymbol{Af/A}$)	0.719

Several modifications to the geometry of the mesh were required due to the original design being intended for conventional manufacturing from aluminium sheet metal and not AM. Thus, for the full-size design, the material was changed to Ti64 titanium alloy, the fin thickness was changed to 0.8 mm to allow for LPBF printing, and the thickness of the dividing walls was changed to 2 mm to prevent warping

© Central University of Technology, Free State

when printing at half scale. Additionally, CRPM recommended that 0.8 mm fillets be installed between the fins to avoid possible issues during manufacturing. As stated by Kays and London [34], any modifications made to the fin thickness or profile of a cell would also affect the hydraulic diameter and passage volume of the mesh. Therefore, these parameters were recalculated for the new geometry.

Hydraulic diameter

Utilising the information provided in Table 5, the profile for the modified 5.3 plate fin layout was designed using SolidWorks 3D modelling software, wherein the thickness of the fins was changed to 0.8 mm, and 0.8 mm fillets were added to internal angles. The resulting cell is illustrated in Figure 43, where the highlighted section indicates the available free-flow area through the cell.

Figure 43: Single cell for modified 5.3 plate fin

The new wetted perimeter and free-flow area of the modified cell were measured using the Solidworks evaluation toolset, where:

$$\mathbf{A_{cell}} = \mathbf{97.220x10^{-6}}\boldsymbol{m^2}$$

$$\mathbf{p_{cell}} = \mathbf{58.540x10^{-3}}\boldsymbol{m}$$

This was then used to calculate the new hydraulic diameter for a singular modified cell. Since the hydraulic diameter is defined as four times the area of a passage divided by the wetted perimeter [35], Eq. 5.1 was used to determine the new hydraulic diameter for the adjusted cells.

$$\boldsymbol{D_h} = \frac{\mathbf{4}(\boldsymbol{A})}{\boldsymbol{p}} \qquad \text{Eq. 5.1}$$

Where:

$\boldsymbol{D_h} = \boldsymbol{hydraulic\ diameter}$

© Central University of Technology, Free State

$\mathbf{A_{cell}} = \mathbf{97.220x10^{-6}}\boldsymbol{m^2}$

$\boldsymbol{p} = \mathbf{58.540x10^{-3}}\boldsymbol{m}$

Thus:

$$\boldsymbol{D_h} = \frac{\mathbf{4(97.220x10^{-6})}}{\mathbf{58.540x10^{-3}}}$$

$$\boldsymbol{D_h} = \mathbf{6.643\ x10^{-3}}\ \boldsymbol{m}$$

Per-passage free-flow areas

By expanding the CAD model to the driving dimensions of the hot (L2) and cold (L1) side passages, as listed in Table 4, the total number of cells across the hot and cold side cells could be calculated. Due to the individual cells having a vertical height of 10 mm, the expanded model consisted of 22 cells across the hot side and nine cells across the cold side (Figure 44).

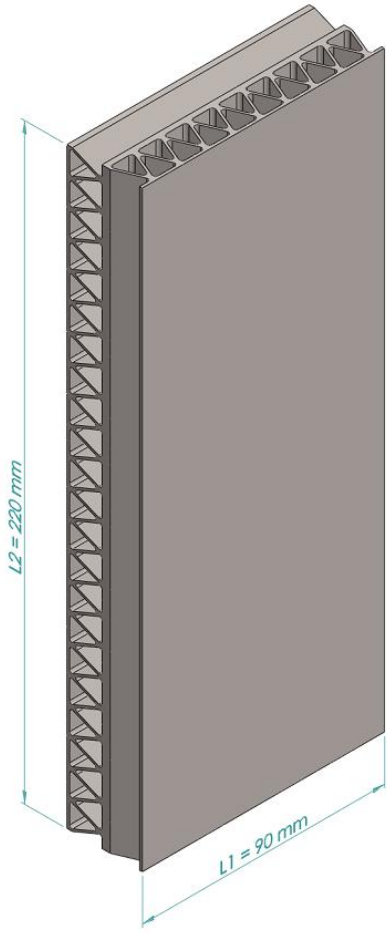

Figure 44: Full-size L1 and L2 expanded model

© Central University of Technology, Free State

To determine the free-flow area for a single passage of the hot side, the measured free-flow area of a single cell was multiplied by the total number of cells across the hot side via Eq. 5.2.

$$A_{f_{h,p}} = A_{cell} * N_{cells} \quad \text{Eq. 5.2}$$

$$\mathbf{A_{f_{h,p}} = 97.220x10^{-6} * 22}$$

$$\mathbf{A_{f_{h,p}} = 2.139x10^{-3} m^2}$$

Similarly, to determine the free-flow area for a single passage of the cold side, the passage area for a single cell was multiplied by the total number of cells across the cold side via Eq. 5.3.

$$A_{f_{c,p}} = A_{cell} * N_{cells} \quad \text{Eq. 5.3}$$

$$\mathbf{A_{f_{c,p}} = 97.220x10^{-6} * 9}$$

$$\mathbf{A_{f_{c,p}} = 0.875x10^{-3} m^2}$$

Number of parallel passages

To determine the overall width of the design, Eq. 5.4 – the method provided by Shah and Sekulic [35] was utilised to obtain the optimal number of passages needed to fulfil the area requirements.

$$N_P = \frac{L_3 - b_c + 2\delta_w}{b_h + b_c + 2\delta_w} \quad \text{Eq. 5.4}$$

Where:

$N_P = number\ of\ parallel\ passages$

$L_3 = 220x10^{-3} m = cell\ tile\ width$

$b_h = 12x10^{-3} m = hot\ side\ cell\ width$

$b_c = 12x10^{-3} m = hot\ side\ cell\ width$

$\delta_w = 2x10^{-3} m = dividing\ wall\ thickness$

Thus:

$$N_P = \frac{220x10^{-3} - 12x10^{-3} + 2(2x10^{-3})}{12x10^{-3} + 12x10^{-3} + 2}$$

$$N_{P,h} = 7.571 = 8\ passages$$

© Central University of Technology, Free State

Shah and Sekulic recommended that the total number of passages on the hot side of the heat exchanger be rounded up to an even number, which resulted in the actual width (L3) of the final heat exchanger being slightly wider than the initial estimate of 220 mm. The maximum width of the design was increased to accommodate this change. To reduce the potential heat wasted to the atmosphere from an exposed hot side passage, an additional cold side channel was added to close off the heat exchanger.

$$N_{P,c} = N_{P,h} + 1 \qquad \text{Eq. 5.5}$$

Thus, the total number of cold side passages was:

$$N_{P,c} = 8 + 1 = 9$$

Having obtained the total number of passages across the hot and cold sides of the heat exchanger, the model displayed in Figure 44 was expanded to full size, as seen in Figure 45 .

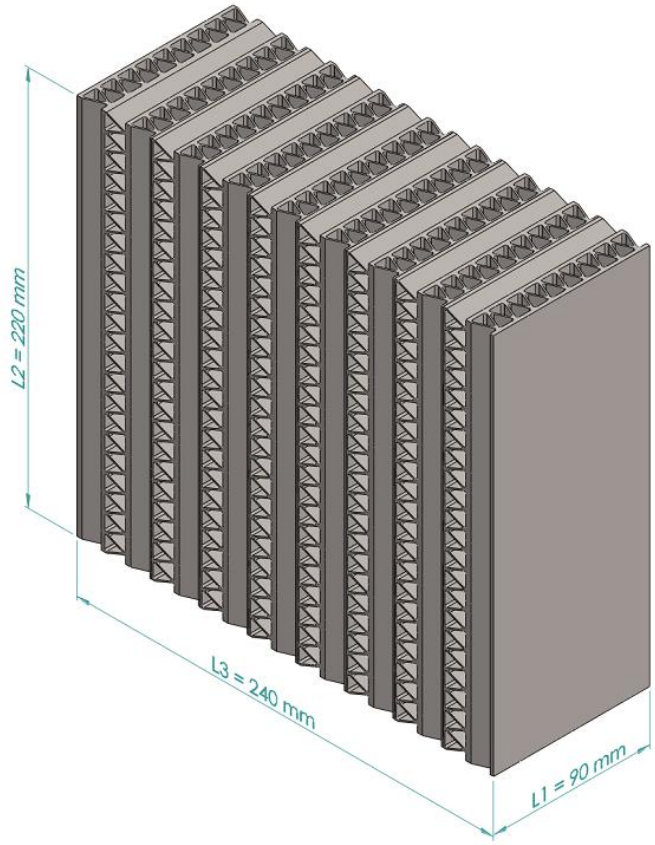

Figure 45: Full-size L1, L2, and L3 expanded model

© Central University of Technology, Free State

Full-size free-flow areas

To obtain the total free-flow areas of the hot and cold side for the full-size design, the per-passage free-flow area was multiplied by the number of passages in the mesh.

$$\mathbf{A_f} = \mathbf{A_{f_p}} * \boldsymbol{N_P} \qquad \text{Eq. 5.6}$$

From the previous heading, the number of passages for the hot side was determined to be eight, while the number of cold passages was found to be nine.

Thus:

$$\mathbf{A_{f_c}} = \mathbf{0.875x10^{-3}} * \mathbf{9} = \mathbf{7.875}\boldsymbol{x}\mathbf{10^{-3}}\boldsymbol{m^2}$$

And:

$$\mathbf{A_{f_h}} = \mathbf{2.139x10^{-3}} * \mathbf{8} = \mathbf{17.112x10^{-3}}\boldsymbol{m^2}$$

Full-size heat exchanger design

Having obtained the size and shape of the heat exchanger for the single pass in Figure 45, by expanding the CAD to include the three individual passes, the results are shown in Figure 46.

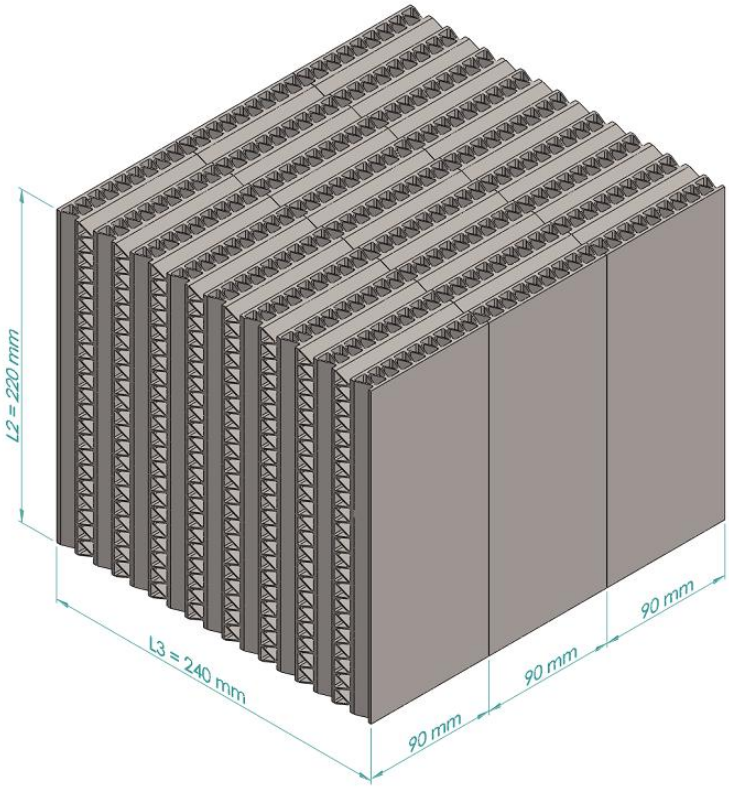

Figure 46: Three-pass full-size heat exchanger

© Central University of Technology, Free State

Full-size heat transfer analysis

Due to the iterative design process, which requires many repeating calculations, the individual formulas are presented in order of usage, accompanied by notes to guide the reader through the process. The repeating calculations were conducted using an Excel spreadsheet, and the results obtained from the process are displayed in table form. The unprocessed theoretical calculations are included for review in Appendix 1.

Hot side frontal area

To calculate the total frontal area of the hot side of the core, the hot side cell height L2 was multiplied by the estimated passage tile width L3, as shown in Eq. 5.7.

$$A_{fr_h} = L_2 L_3 \qquad \text{Eq. 5.7}$$

Where:

$A_{fr\_h} = frontal\ area\ of\ hot\ side$

$L_2 = hot\ side\ cell\ height$

$L_3 = cell\ tile\ width$

Cold side frontal area

Similarly, to calculate the frontal area of the core, the cold side passage height L1 was multiplied by the passage tile width L3, displayed as Eq. 5.8.

$$A_{fr_c} = L_1 L_3 \qquad \text{Eq. 5.8}$$

Where:

$A_{fr\_c} = frontal\ area\ of\ cold\ side$

$L_1 = cold\ side\ cell\ height$

$L_3 = passage\ tile\ width$

Hot side passage volume

To calculate the passage volume of the hot side, Eq. 5.9, as derived by [35], was used.

$$V_{p_h} = L_1 L_2 (b_h N_p) \qquad \text{Eq. 5.9}$$

Where:

$V_{p_h} = hot\ side\ passage\ volume$

© Central University of Technology, Free State

$L_1 = cold\ side\ cell\ height$

$L_2 = hot\ side\ cell\ height$

$b_h = hot\ side\ cell\ width$

$N_P = number\ of\ parallel\ passages$

Cold side passage volume

To calculate the passage volume of the cold side, Eq. 5.10 was used. In accordance with example 9.1 from Shah and Sekulic [35], the cold side was assumed to have an extra passage added to cap off the heat exchanger.

$$V_{p_c} = L_1 L_2 b_c (N_p + 1) \quad \text{Eq. 5.10}$$

Where:

$V_{p_c} = cold\ side\ passage\ volume$

$L_1 = cold\ side\ cell\ height$

$L_2 = hot\ side\ cell\ height$

$b_c = cold\ side\ cell\ width$

$N_P = number\ of\ parallel\ passages$

Heat transfer areas

To calculate the available heat transfer areas for the hot and cold sides, the total transfer area to volume ratio (β), obtained from the surface geometry tables, was multiplied with the passage volumes via Eq. 5.11.

$$A_{transfer} = \beta V_p \quad \text{Eq. 5.11}$$

Where:

$A_{transfer} = heat\ transer\ area$

$\beta = total\ transfer\ area\ to\ volume\ ratio$

$V_p = passage\ volume$

Hot side free-flow area

Ordinarily, the free-flow areas for the hot and cold sides of the heat exchanger would be calculated using Eq. 5.12 [35]. However, due to the required

© Central University of Technology, Free State

modifications to the cells, the new hydraulic diameter and free-flow areas were recalculated.

$$A_o = \frac{D_h A}{4L} \quad \text{Eq. 5.12}$$

Where:

$A_o = free\ flow\ area$

$D_h = hydraulic\ diameter$

$A = heat\ transfer\ area$

$L_1 = passage\ length$

Heat transfer ratio

To calculate the new free heat transfer ratio for the hot and cold sides, the free-flow areas were divided by the frontal areas using Eq. 5.13.

$$\sigma = \frac{A_o}{A_{fr}} \quad \text{Eq. 5.13}$$

Where:

$\sigma = heat\ transer\ ratio$

$A_o = free\ flow\ area$

$A_{fr} = frontal\ area$

Heat capacity rate ratio

To calculate the heat capacity rates of the hot and cold side fluids, the specific heat capacity of the fluids was multiplied by their relevant mass flow rates using Eq. 5.14.

$$C = \dot{m} c_p \quad \text{Eq. 5.14}$$

To obtain the heat capacity rate ratio between the hot and cold side fluids, Eq. 5.15 was used, where C_{min} is the heat transfer capacity of the cold fluid and C_{max} is the heat transfer capacity of the hot fluid.

$$C_r = \frac{C_{min}}{C_{max}} \quad \text{Eq. 5.15}$$

© Central University of Technology, Free State

Where:

$C_r = heat\ capacity\ ratio$

$c_p = specific\ heat\ capacity$

$\dot{m} = mass\ flow\ rate$

$C = heat\ capacity\ rate$

Air density

The density of the hot and cold side fluids was necessary for several calculations as the working fluid was assumed to be in ideal air conditions, and the ideal gas law was rearranged to obtain Eq. 5.16.

$$\rho = \frac{P}{\tilde{R}T} \quad \text{Eq. 5.16}$$

Estimated hot side temperature out

Using the initial estimated effectiveness in combination with the assumed inlet conditions for the heat exchanger, Eq. 5.17, as derived by Shah and Sekulic [35], was used to determine the estimated output conditions for the hot side.

$$T_{h_o} = T_{h_i} - \varepsilon_{estimated}\left(\frac{C_{min}}{C_{hot}}\right)(T_{h_i} - T_{c_i}) \quad \text{Eq. 5.17}$$

It was assumed that the specific heat capacities for the hot and cold fluids were approximate in nature. Note, this step is only applicable to heat exchangers where the working fluids across the hot and cold sides of the heat exchanger are the same fluid, which in this case is air. Thus, for a heat exchanger where this is not applicable, this assumption cannot be made. By applying Eq. 5.14, Eq. 5.17 can be rewritten in terms of the mass flow rate as Eq. 5.18.

$$T_{h_o} = T_{h_i} - \varepsilon_{estimated}\left(\frac{\dot{m}_{min}}{\dot{m}_{hot}}\right)(T_{h_i} - T_{c_i}) \quad \text{Eq. 5.18}$$

Where:

$T_{h_o} = hot\ side\ temperature\ outlet$

$T_{h_i} = hot\ side\ temperature\ inlet$

$\varepsilon = estimated\ efficiency$

© Central University of Technology, Free State

Estimated cold side temperature out

Similarly, Eq. 5.19 [35] was used to calculate the estimated output conditions for the cold side of the heat exchanger.

$$T_{c_o} = T_{c_i} - \varepsilon\left(\frac{C_{min}}{C_{cold}}\right)\left(T_{h_i} - T_{c_i}\right) \quad \text{Eq. 5.19}$$

And following the same assumptions made for the hot side, Eq. 5.19 was rewritten as Eq. 5.20.

$$T_{c_o} = T_{c_i} - \varepsilon\left(\frac{\dot{m}_{min}}{\dot{m}_{cold}}\right)\left(T_{h_i} - T_{c_i}\right) \quad \text{Eq. 5.20}$$

Where:

$T_{c_o} = cold\ side\ temperature\ outlet$

$T_{c_i} = cold\ side\ temperature\ inlet$

$\varepsilon = estimated\ effectivness$

Mean temperature

Having calculated the outlet temperatures for the hot and cold sides, the arithmetic average temperatures for both the hot and cold sides were calculated using Eq. 5.21 [35]:

$$T_m = \frac{(T_i - T_o)}{2} \quad \text{Eq. 5.21}$$

Where:

$T_m = mean\ temperature$

$T_o = outlet\ temperature$

$T_i = inlet\ temperature$

Fluid properties at the mean temperature

Due to insufficient information about the condition of the air passing through the heat exchanger, an initial estimate was necessary to initiate the iterative process. The fluid properties for air at atmospheric temperature, as provided by Holman [34], were utilised to obtain the properties of the hot and cold side fluids at the calculated mean temperatures. The tables for atmospheric air are presented in Table 27 of Appendix 2. Note that for an ideal gas, the dynamic viscosity (μ), specific heat capacity (c_p) , and Prandtl number (Pr) are assumed to be

© Central University of Technology, Free State

independent of pressure; therefore, Table 27 could be used for both the hot and cold side fluids [34], [35].

Mass velocity

To obtain the mass velocity of the hot and cold sides, the mass flow rates were divided by the relevant free-flow areas via Eq. 5.22.

$$G = \frac{\dot{m}}{A_o} \quad \text{Eq. 5.22}$$

Where:

$G = mass\ velocity$

$\dot{m} = mass\ flow\ rate$

$A_o = free\ flow\ area$

Reynolds number

$$Re = \frac{GD_h}{\mu} \quad \text{Eq. 5.23}$$

Where:

$Re = \text{Reynolds number}$

$G = mass\ velocity$

$D_h = hydraulic\ diameter$

$\mu = fluid\ viscosity$

Heat transfer coefficient

Starting with the definition of the Colburn factor and rearranging it with respect to the heat transfer coefficient, Eq. 5.24 can be used to obtain the separate heat transfer coefficients for both the hot and cold side fluids [35]. Note that the Colburn factor (j) is obtained from the lower line on the relevant Kays and London chart, shown in Figure 47.

$$h = \frac{jGc_p}{Pr^{\frac{2}{3}}} \quad \text{Eq. 5.24}$$

Where:

$h = heat\ transfer\ coefficient$

© Central University of Technology, Free State

$G = mass\ velocity$

$D_h = hydraulic\ diameter$

$\mu = fluid\ viscosity$

$j = Colburn\ factor$

Fig. 10-23 Plain plate-fin surface 5.3.

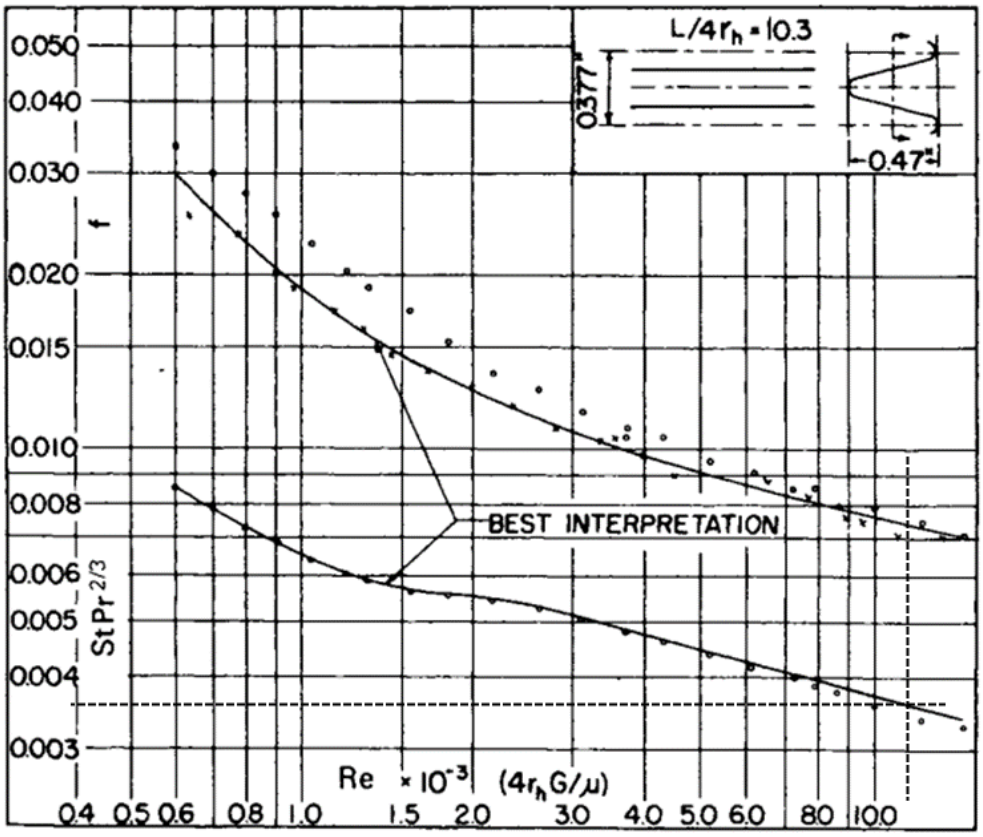

Fin pitch = 5.3 in = 208.7 per m
Plate spacing, b = 0.470 in = 11.94 x 10^{-3} m
Flow passage hydraulic diameter, $4r_h$ = 0.02016 ft = 6.147 x 10^{-3} m
Fin metal thickness = 0.006 in, aluminum = 0.152 x 10^{-3} m
Total transfer area/volume between plates, β = 188 ft^2/ft^3 = 616.8 m^2/m
Fin area/total area = 0.719

Figure 47: Plain plate-fin surface 5.3 datasheet [34]

Please note that for the design process of the full size design, the Reynolds number for the hot side was slightly higher than the label on Figure 47 indicated despite the dataset going well past that point. Thus the J factor for the hot side was estimated using the last known Re value as indicated on Figure 47.

© Central University of Technology, Free State

Fin efficiency

To estimate the fin parameter (m) of the selected fin type, Eq. 5.25 [35], was used.

$$m = \left(\frac{2h}{k_f \delta}\left(1 + \frac{\delta}{l_s}\right)\right)^{\frac{1}{2}} \quad \text{Eq. 5.25}$$

To calculate the estimated efficiency of the fins, Eq. 5.26 [35], was used.

$$\eta_f = \frac{tanh(ml_i)}{(ml_i)} \quad \text{Eq. 5.26}$$

Lastly, to estimate the fin parameter (l_i) of the selected fin type, Eq. 5.27 [35], was used.

$$l_i = \frac{l_s}{2} \quad \text{Eq. 5.27}$$

Where:

$m = fin\ parameter$

$\delta = fin\ thickness$

$l_s = strip\ length$

$h = heat\ transfer\ coefficient$

$\eta_f = fin\ efficiency$

Overall fin efficiency

To calculate the overall efficiency of the fins, Eq. 5.28, [35], was used where the fin area to total area ratio was obtained from the additional information supplied on the relevant Kays and London chart in Figure 47.

$$\eta_o = \left[1 - (1 - n_f)\left(\frac{A_f}{A}\right)\right] \quad \text{Eq. 5.28}$$

Where:

$\eta_o = overall\ fin\ efficiency$

$n_f = fin\ efficiency$

$\frac{A_f}{A} = fin\ area\ to\ total\ area\ ratio$

© Central University of Technology, Free State

Dividing wall area

In order to account for the effect that the dividing walls would have on the thermal resistivity of the mesh, the area of the dividing walls was calculated using Eq. 5.29 [35].

$$A_w = L_1 L_2 (2N_p + 2) \quad \text{Eq. 5.29}$$

Where:

$A_w = dividing\ wall\ area$

$L_2 = hot\ side\ cell\ height$

$L_1 = cold\ side\ cell\ height$

$N_P = number\ of\ parallel\ passages$

Dividing wall resistance

Having calculated the area of the dividing walls, the thermal resistivity for the selected mesh was calculated via Eq. 5.30 [35].

$$R_w = \frac{\delta_w}{k_w A_w} \quad \text{Eq. 5.30}$$

Where:

$R_w = wall\ resistance$

$\delta_w = wall\ thickness$

$k_w = wall\ heat\ transfer\ coefficient$

$A_w = wall\ resistance.$

Overall thermal conductance (UA)

Having calculated all of the unknown variables for the dataset, Eq. 5.31 was used to calculate the overall thermal conductance for the selected heat exchanger mesh [35]. Note that for this application, fouling resistances were ignored due to a lack of information.

$$UA = \left[\frac{1}{(\eta_o h A)_h} + R_w + \frac{1}{(\eta_o h A)_c}\right]^{-1} \quad \text{Eq. 5.31}$$

© Central University of Technology, Free State

Where:

$UA = overall\ thermal\ conductance$

$\eta_o = overall\ fin\ efficiency$

$h = heat\ transfer\ coefficient$

$A = heat\ transfer\ area$

$R_w = wall\ resistance$

Number of heat transfer units

Having calculated the overall UA for the selected mesh, Eq. 5.32 was used to calculate the number of transfer units [35].

$$NTU = \frac{UA}{C_{min}} \qquad \text{Eq. 5.32}$$

Where:

$NTU = number\ of\ heat\ transfer\ units$

$UA = overall\ thermal\ conductance$

$C_{min} = minimum\ heat\ transfer\ capacity$

Actual effectiveness

Next, to calculate the expected effectiveness of the heat exchanger, Eq. 5.33 as presented by Holman [7], was used, which is applicable to cross-flow heat exchangers where both fluids remain unmixed and is therefore applicable to this study.

$$\varepsilon_{actual} = 1 - exp\left[\frac{exp\left(-NTU * C_r\left(NTU^{-0.22}\right) - 1\right)}{C_r * NTU^{-0.22}}\right] \qquad \text{Eq. 5.33}$$

Where:

$\varepsilon = heat\ exchanger\ effectivness$

$C_r = heat\ transfer\ capacity\ ratio$

$NTU = number\ of\ heat\ transfer\ units$

© Central University of Technology, Free State

Heat transfer rate

Having calculated the actual effectiveness of the heat exchanger, the expected heat transfer between the working fluids was calculated using Eq. 5.34 [35].

$$\dot{q} = \varepsilon_{actual}(T_{h_i} - T_{c_i})C_{min} \quad \text{Eq. 5.34}$$

Where:

$\dot{q} = heat\ transfer\ rate$

$T_{h_i} = hot\ side\ temperature\ inlet$

$T_{c_i} = cold\ side\ temperature\ inlet$

$C_{min} = minimum\ heat\ transfer\ capacity$

Estimated vs actual effectiveness

Having calculated the actual effectiveness of the heat exchanger using the selected parameters, the actual effectiveness of the proposed heat exchanger was compared to the initial estimate. Due to the selected design methodology proposed by Shah and Sekulic [35] being based on an iterative process, where the effectiveness tends towards the correct value with each iteration, a minimum of three iterations would be required to determine the expected effectiveness for the full-size heat exchanger. Figure 48 shows how a series of three iterations were performed for each pass of the heat exchanger, with the results from each pass being used to begin the iterations for the subsequent pass until all unknowns were accounted for.

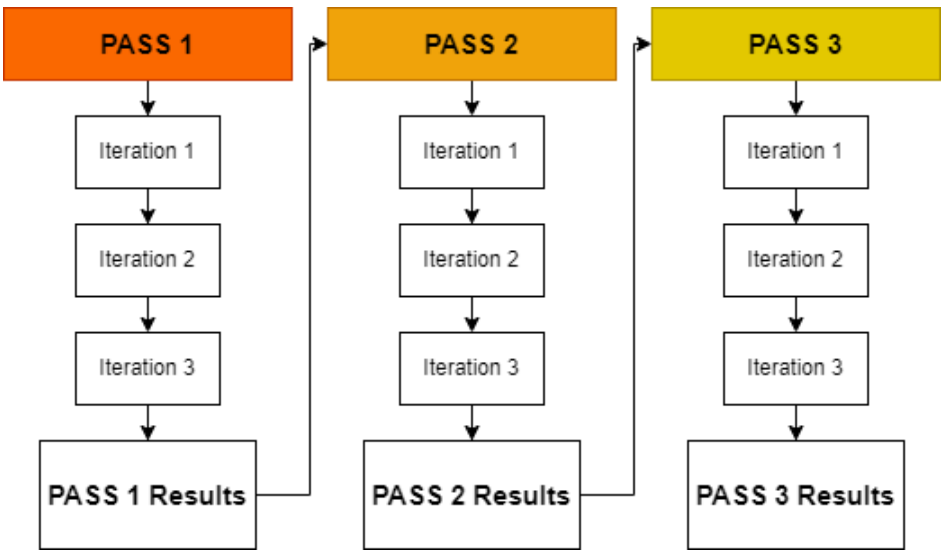

Figure 48: Iterative design process

© Central University of Technology, Free State

Pressure drop analysis

After reaching convergence for the effectiveness across all three individual passes, the pressure drop analysis process could be completed. To calculate the pressure drop across the heat exchanger core, Eq. 5.35 was used [35]. To account for the contraction (K_c) and expansion (K_e) losses experienced by the air passing though the heat exchanger, Figure 49 was used.

$$\Delta P = \frac{G^2}{2g_c\rho_i}\left[(1-\sigma^2+K_c)+2\left(\frac{\rho_i}{\rho_o}-1\right)+f\left(\frac{L}{r_h}\right)\left(\frac{\rho_i}{\rho_m}\right)-(1-\sigma^2-K_e)\left(\frac{\rho_i}{\rho_o}\right)\right] \quad \text{Eq. 5.35}$$

Where:

$\Delta p = pressure\ change$

$G = mass\ velocity$

$g_c = 1$

$\rho_i = inlet\ density$

$\rho_o = outlet\ density$

$\sigma = heat\ transfer\ ratio$

$K_c = contraction\ pressure\ loss\ coefficient$

$K_e = expansion\ \ pressure\ loss\ coefficient$

$f = fanning\ friction\ factor$

$r_h = hydraulic\ radius$

$L = length\ of\ channel$

© Central University of Technology, Free State

Fig. 5-5 Entrance and exit pressure-loss coefficients for a multiple-tri-angular-tube heat exchanger core with abrupt-contraction entrance and abrupt-expansion exit.

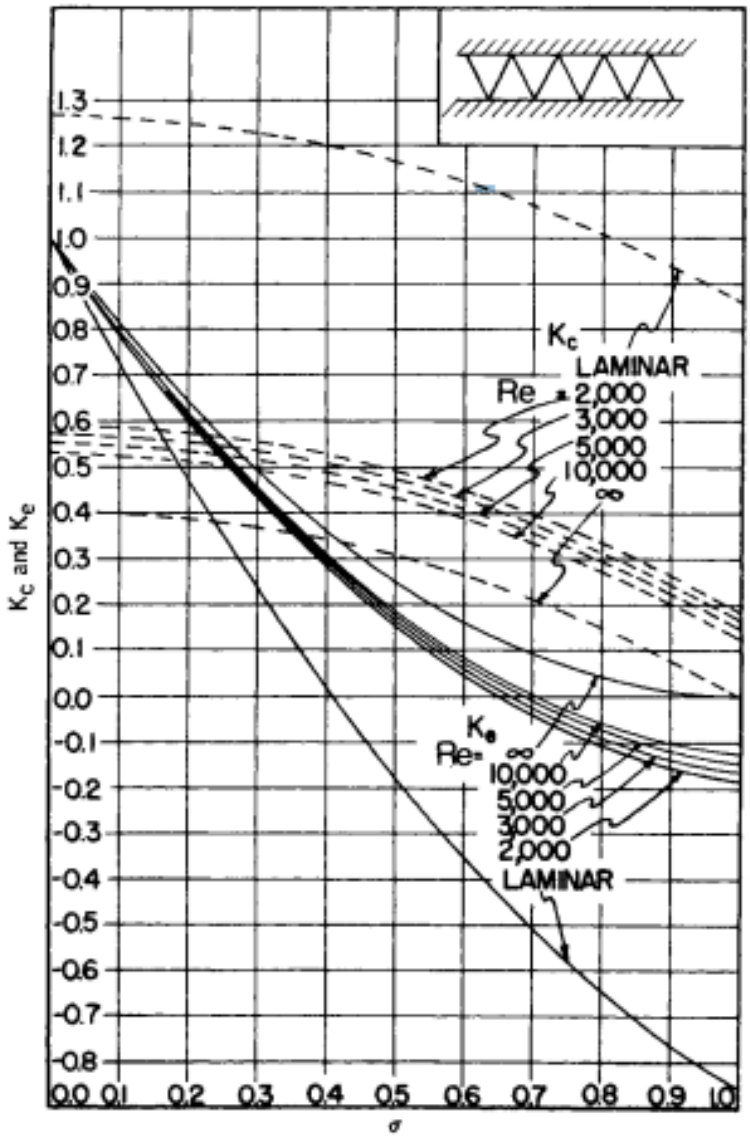

Figure 49: Entrance and exit pressure loss coefficients [34]

© Central University of Technology, Free State

5.2 Full-size results

The estimated heat transfer characteristics of the full-size multi-pass heat exchanger were calculated by using the design process previously discussed. Due to the vast number of calculations involved in characterising the selected heat exchanger, it was decided that Microsoft Excel would be used to perform the iterative calculations, with SMath Studio used to verify the individual formulas.

The results of this iterative design process for the full-size design are displayed in Table 6. The complete unprocessed calculations are available in Appendix 1.

Table 6: Full-size, heat transfer characteristics

	Pass 1	Pass 2	Pass 3
Hot side inlet temperature (T_{h_i})	249.860 °C	236.007 °C	227.064 °C
Hot side outlet temperature (T_{h_o})	236.007 °C	227.064 °C	221.318 °C
Hot side temperature change (ΔT_h)	-13.853 °C	-8.943 °C	-5.746 °C
Cold side inlet temperature (T_{c_i})	25 °C	92.848 °C	136.338 °C
Cold side outlet temperature (T_{c_o})	92.848 °C	136.338 °C	164.124 °C
Cold side temperature change (ΔT_c)	67.848 °C	43.491 °C	27.786 °C
Heat exchanger effectiveness (ε)	0.302	0.304	0.306
Heat transfer rate (Q)	11.715 kW	7.546 kW	4.842 kW
Total			
Total hot side temperature change			-28.542 °C
Total cold side temperature change			+139.124 °C

The pressure losses for the hot and cold sides of the full-size design were then calculated using Table 6 and Eq. 5.35, which resulted in the data provided in Table 7. Note that the pressure drop analysis excluded the pipe bending losses and external pipe friction, as well as assuming that the hot side passages were continuous throughout the length of the design.

© Central University of Technology, Free State

Table 7: Full-size, pressure drop

	Pass 1	Pass 2	Pass 3
Hot side inlet pressure (P_{h_i})	628.215 kPa	N/a	N/a
Hot side outlet pressure (P_{h_o})	627.683 kPa	N/a	N/a
Hot side pressure change (ΔP_h)	-532.346 Pa	N/a	N/a
Cold side inlet pressure (P_{c_i})	110 kPa	109.525 kPa	108.992 kPa
Cold side outlet pressure (P_{c_o})	109.525 kPa	108.992 kPa	108.422 kPa
Cold side pressure change (ΔP_c)	-475.309 Pa	-532.206 Pa	-470 Pa
Total			
Total hot side pressure change			-532.346 Pa
Total cold side pressure change			-1.557 kPa

5.3 Single-passage design

After completing the design process for the full-size design, a single hot side passage was extracted from the first pass of the full-size design, as indicated in Figure 36. Due to technical limitations with the methodology, two cold side passages on either side of the hot passage were required for the process to function.

Single-passage frontal areas

Starting from Figure 44, the CAD model for the single passage was expanded with an additional cold side passage to cap-off the heat exchanger, as indicated in Figure 50.

© Central University of Technology, Free State

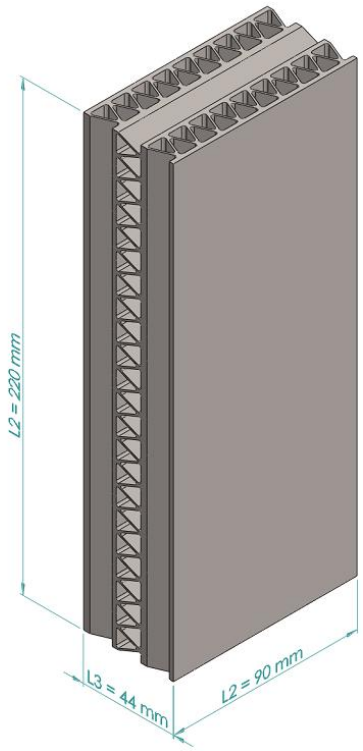

Figure 50: Single passage L1, L2, and L3 expanded model

To calculate the free-flow areas for the hot side of the single-passage design, Eq. 5.6 was reused where the total number of passages was 1.

$$\mathbf{A_{f_h}} = \mathbf{A_{f_p}} * \boldsymbol{N_P}$$

$$\mathbf{A_{f_h}} = \mathbf{2.139x10^{-3}} * \mathbf{1} = \mathbf{2.139x10^{-3}}\boldsymbol{m^2}$$

To calculate the free-flow areas for the cold side single-passage design, Eq. 5.6 was reused where the total number of passages was 2.

$$\mathbf{A_{f_c}} = \mathbf{A_{f_p}} * \boldsymbol{N_P}$$

$$\mathbf{A_{f_c}} = \mathbf{0.875x10^{-3}} * \mathbf{2} = \mathbf{1.750}\boldsymbol{x}\mathbf{10^{-3}}\boldsymbol{m^2}$$

5.4 Single-passage results

Having calculated the expected performance for the full-size heat exchanger, the iterative design process for the full-size design was repeated for the single-passage design in Figure 50, which consisted of one hot side passage between two cold side passages. To retain proportionality with the full-size design, which had eight hot side channels, the single-passage segment was assumed to have to operate on 1/8th of the mass flow rate of the full-size design. The heat transfer

© Central University of Technology, Free State

characteristics and pressure losses that were obtained for the single passage are set out in Table 8 and Table 9, respectively.

Table 8: Single passage, heat transfer characteristics

Pass 1	
Hot side inlet temperature (T_{h_i})	249.860 °C
Hot side outlet temperature (T_{h_o})	234.149 °C
Cold side inlet temperature (T_{c_i})	25 °C
Cold side outlet temperature (T_{c_o})	101.910 °C
Heat exchanger effectiveness (ε)	0.342
Heat transfer rate (Q)	1.661 kW
Total	
Hot side temperature change	-15.711 °C
Cold side temperature change	+76.910 °C

Table 9: Single passage, pressure drop

Pass 1	
Hot side inlet pressure (P_{h_i})	628.215 kPa
Hot side outlet pressure (P_{h_o})	627.888 kPa
Cold side inlet pressure (P_{c_i})	110 kPa
Cold side outlet pressure (P_{c_o})	109.841 kPa
Total	
Total hot side pressure change	-327.259 Pa
Total cold side pressure change	-159.390 Pa

© Central University of Technology, Free State

5.5 Dynamic similarity

After calculating the expected performance parameters for the single passage, the concept of DS and DA could be applied to verify the single-passage design utilising a half-scale model. From the research performed by Sánchez-Escalona et al. [37], Eq. 5.36 was used to match similarity conditions between the single-passage design and the test piece.

$$\frac{T_{c_o} - T_{c_i}}{T_{h_i} - T_{c_i}} = f\left(\frac{\dot{m}_h}{\dot{m}_c}\right) \quad \text{Eq. 5.36}$$

To meet the conditions required for DS between the single passage and test piece, geometric, kinematic, and DS conditions had to be determined. To complete the requirements for geometric similarity between the single-passage and the test-piece designs for both hot and cold sides, the test piece had to be scaled down by a constant scale factor. Note the scale factor must be squared to account for the reduction in area, which results in Eq. 5.37.

$$A_{f\_Test\ piece} = A_{f\_Single\ passage} * (SF)^2 \quad \text{Eq. 5.37}$$

Where:

$A_{f\_Test\ piece} = free\ flow\ area\ of\ test\ piece$

$A_{f\_Single\ passage} = free\ flow\ area\ of\ single\ passage$

$SF = scale\ factor\ constant$

To complete the requirements for kinematic similarity between the prototype and the test piece for both hot and cold sides, the velocities of the air passing through the heat exchanger were similarly scaled down by the same scale factor.

$$v_{Test\ piece} = v_{Single\ passage} * SF \quad \text{Eq. 5.38}$$

Where:

$v_{Test\ piece} = velocity\ of\ air\ through\ test\ piece$

$v_{Single\ passage} = velocity\ of\ air\ through\ single\ passage$

Lastly, to meet the requirements for DS between the single-passage design and the test piece, complete proportionality of internal forces was required. However, it was found that complete DS was not possible while fulfilling Eq. 5.38 because it would result in the required pressure of the cold side falling below atmospheric pressure and would need to be tested in a partial vacuum. Fortunately, having

© Central University of Technology, Free State

achieved geometric and kinematic similarity, partial DS could be achieved, which allowed for testing to continue.

Testing conditions

Starting with the specifications for the single-passage data obtained from the prior calculations presented in Table 10, the experimental conditions for the testing procedure could be calculated.

Table 10: Single-passage data

	Hot side	Cold side
Inlet density (ρ)	$4.184\ kg/m^3$	$1.184\ kg/m^3$
Mass flow rate ($\dot{m}$)	$102.375x10^{-3}\ kg/s$	$21.417x10^{-3}\ kg/s$
Free flow area (A)	$2.139x10^{-3}\ m^2$	$1.750x10^{-3}\ m^2$
Inlet temperature (T_i)	$522.860\ °C$	$298.000\ °C$
Outlet temperature (T_o)	$507.149\ °C$	$374.910\ °C$

Single-passage velocities

Having calculated the mass flow rate, free-flow area, and inlet densities for both the hot and cold sides of the single-passage design, the velocity of the air across the hot and cold sides were approximated using Eq. 5.30.

$$v = \frac{\dot{m}}{A_f * \rho} \qquad \text{Eq. 5.39}$$

Where the velocity for the hot side fluid:

$$(v_h)_{Single\ passage} = \frac{\dot{m}_h}{A_{f_h} * \rho_h}$$

$$(v_h)_{Single\ passage} = \frac{102.375x10^{-3}}{2.139x10^{-3} * 4.184}$$

$$(v_h)_{Single\ passage} = 11.439\ m/s$$

And the velocity for the cold side fluid:

$$(v_c)_{Single\ passage} = \frac{\dot{m}_c}{A_{o_c} * \rho_c}$$

$$(v_c)_{Single\ passage} = \frac{21.417x10^{-3}}{1.750x10^{-3} * 1.184}$$

$$(v_c)_{Single\ passage} = 10.336\ m/s$$

© Central University of Technology, Free State

Test piece velocities

Having calculated the velocities for the single-passage design, Eq. 5.38 was used to calculate the velocities of the hot and cold fluids through the test piece.

Where the velocity for the hot side fluid:

$$(v_h)_{Test\ piece} = (v_h)_{Single\ passage} * SF$$

$$(v_h)_{Test\ piece} = 11.439 * 0.5$$

$$(v_h)_{Test\ piece} = 5.719\ m/s$$

And the velocity for the cold side fluid:

$$(v_c)_{Test\ piece} = (v_h)_{Single\ passage} * SF$$

$$(v_c)_{Test\ piece} = 10.336 * 0.5$$

$$(v_c)_{Test\ piece} = 5.168\ m/s$$

Test piece free-flow areas

To calculate the new free-flow areas of the test piece, Eq. 5.37 was used.

Where the free-flow area of the hot side was:

$$\left(A_{f_h}\right)_{Test\ piece} = \left(A_{f_h}\right)_{Single\ passage} * (SF)^2$$

$$\left(A_{f_h}\right)_{Test\ piece} = 2.139x10^{-3} * (0.5)^2$$

$$\left(A_{f_h}\right)_{Test\ piece} = 534.750x10^{-6}\ m^2$$

And the free-flow area across the cold side was:

$$\left(A_{f_c}\right)_{Test\ piece} = \left(A_{f_c}\right)_{Single\ passage} * (SF)^2$$

$$\left(A_{f_c}\right)_{Test\ piece} = 1,750x10^{-3} * (0.5)^2$$

$$\left(A_{f_c}\right)_{Test\ piece} = 437.5x10^{-6}\ m^2$$

© Central University of Technology, Free State

Test piece volumetric flow rates

After calculating the velocities of the hot and cold side fluids alongside the free-flow areas, the required volumetric flow rates were calculated using Eq. 5.40.

$$\dot{VOL} = A * v \qquad \text{Eq. 5.40}$$

Where:

$\dot{VOL} = volumetric\ flow\ rate$

$A = free\ flow\ area$

$v = velocity$

Thus, the volumetric flow rate of the hot side:

$$(\dot{VOL}_h)_{Test\ piece} = (A_{f_h} * v_c)_{Test\ piece}$$

$$(\dot{VOL}_h)_{Test\ piece} = 534.750x10^{-6} * 5.719$$

$$(\dot{VOL}_h)_{Test\ piece} = 3.058x10^{-3}\ m^3/s$$

And the volumetric flow rate of the cold side:

$$(\dot{VOL}_c)_{Test\ piece} = (A_{f_c} * v_c)_{Test-Piece}$$

$$(\dot{VOL}_c)_{Test\ piece} = 437.5x10^{-6} * 5.168$$

$$(\dot{VOL}_c)_{Test\ piece} = 2.261x10^{-3}\ m^3/s$$

Test piece mass flow rates

To obtain the mass flow rates on the hot and cold sides for the test piece, while fulfilling the requirements for Eq. 5.36, the ratio between the mass flow rates across the hot and cold sides should remain proportional to one another, as displayed in Eq. 5.41.

$$\left(\frac{\dot{m}_h}{\dot{m}_c}\right)_{Test\ piece} = \left(\frac{\dot{m}_h}{\dot{m}_c}\right)_{Single\ passage} \qquad \text{Eq. 5.41}$$

Where:

$\dot{m} = mass\ flow\ rate$

By assuming the pressure of the air passing through the cold side was open to atmosphere and was supplied at a starting temperature of 17 °C for this iteration,

© Central University of Technology, Free State

the density of the cold side fluid could be calculated using the ideal gas law Eq. 5.16.

$$P = \rho \tilde{R} T$$

$$\rho = \frac{P}{\tilde{R} T_{c,i}}$$

$$\rho = \frac{101.325x10^3}{287.04 * 290}$$

$$\rho = 1.216\ kg/m^3$$

Thus, the required mass flow rate for the cold side fluid through the test piece could be calculated using Eq. 5.42.

$$(\dot{m}_c)_{Test\ piece} = (A_c v_c \rho_c)_{Test\ piece} \quad \text{Eq. 5.42}$$

$$(\dot{m}_c)_{Test\ piece} = 437.5x10^{-6} * 5.168 * 1.216$$

$$(\dot{m}_c)_{Test\ piece} = 2.749x10^{-3}\ kg/s$$

Having calculated the mass flow rate for the air passing through the cold side of the test piece, Eq. 5.41 and Table 10 were then used to obtain the required mass flow rate through the hot side.

$$\left(\frac{\dot{m}_h}{\dot{m}_c}\right)_{Test\ piece} = \left(\frac{\dot{m}_h}{\dot{m}_c}\right)_{Single\ passage}$$

$$\left(\frac{\dot{m}_h}{2.749x10^{-3}}\right)_{Test\ piece} = \left(\frac{102.375x10^{-3}}{21.417x10^{-3}}\right)_{Single\ passage}$$

$$(\dot{m}_h)_{Test\ piece} = \frac{102.375x10^{-3}}{21.417x10^{-3}} * 2.749x10^{-3}$$

$$(\dot{m}_h)_{Test\ piece} = 13.143x10^{-3}\ kg/s$$

Test piece testing pressure

After calculating the mass flow rates for both the hot and cold sides of the test piece, the testing pressure for the hot side was required to finalise the testing conditions. This was achieved by estimating the density of air passing through the hot side of the test piece under the required mass flow rate via Eq. 5.43.

© Central University of Technology, Free State

$$(\rho_h)_{Test\ piece} = \left(\frac{\dot{m}_h}{A_h v_h}\right)_{Test\ piece} \quad \text{Eq. 5.43}$$

$$(\rho_h)_{Test\ piece} = \left(\frac{13.143x10^{-3}}{534.750x10^{-6} * 5.719}\right)$$

$$(\rho_h)_{Test\ piece} = 4.297\ kg/m^3$$

By using Eq. 5.16, the required testing pressure for the hot side of the test piece was then calculated. For this specific measurement, the temperature of the air entering the hot side of the test piece ($T_{h,i}$) was assumed to be 30 °C at the entrance since that was the lowest value expected during testing due to the concerns that the temperature gauges on the test bench would not be able to measure lower temperatures accurately. The variable $T_{h,i}$ would then be changed as needed for each calculation to match the required temperature target.

$$P_{h,i} = \rho \tilde{R} T_{h,i}$$

$$P_{h,i} = 4.297 * 287.04 * 303°K$$

$$P_{h,i} = 373.723x10^3\ Pa$$

Expected performance

Having fulfilled all the requirements for Eq. 5.36, the expected heat transfer capacity for the test piece was estimated using Eq. 5.44.

$$\left(\frac{T_{c,o} - T_{c,i}}{T_{h,i} - T_{c,i}}\right)_{Test\ piece} = \left(\frac{T_{c,o} - T_{c,i}}{T_{h,i} - T_{c,i}}\right)_{Single\ passage} \quad \text{Eq. 5.44}$$

$$\left(\frac{T_{c,o} - 290}{303 - 290}\right)_{Test\ piece} = \left(\frac{374.509 - 298}{522.860 - 298}\right)_{Single\ passage}$$

$$T_{c,o} = 294.423\ °K$$

Thus, for this dataset, which assumed that the inlet temperature on the hot side was 30 °C and the inlet temperature of the cold side was 17 °C, when all similarity constraints were met a temperature increase of 21.423 °C was expected across the cold side of the heat exchanger. This increase in temperature can then be contrasted against the experimental data collected to verify the effectiveness of the single-passage design. To vary the dataset, it was determined that each test run would require at least eight readings between 30 °C and 120 °C, with the process

© Central University of Technology, Free State

described in this heading being repeated for each of the selected temperature targets.

5.6 Test piece manufacturing

After determining the test conditions necessary to achieve DS between the single passage and the test piece, the test piece was modelled at a scale of 0.5 factor, shown in Figure 51.

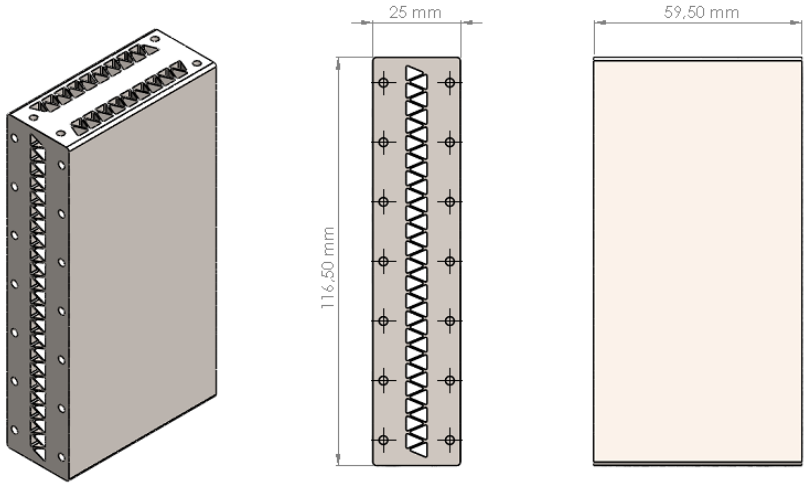

Figure 51: Test piece model

The test piece heat exchanger was then orientated in such a way that the finned internal geometry of the core could be printed without any internal supporting structures on an EOS M290 LPBF system using EOS brand Ti64 Grade 23 40 µm powder. Solid supporting structures were placed on external faces to assist in the build process as well as prevent deformation from occurring during heat treatment, as illustrated in Figure 52.

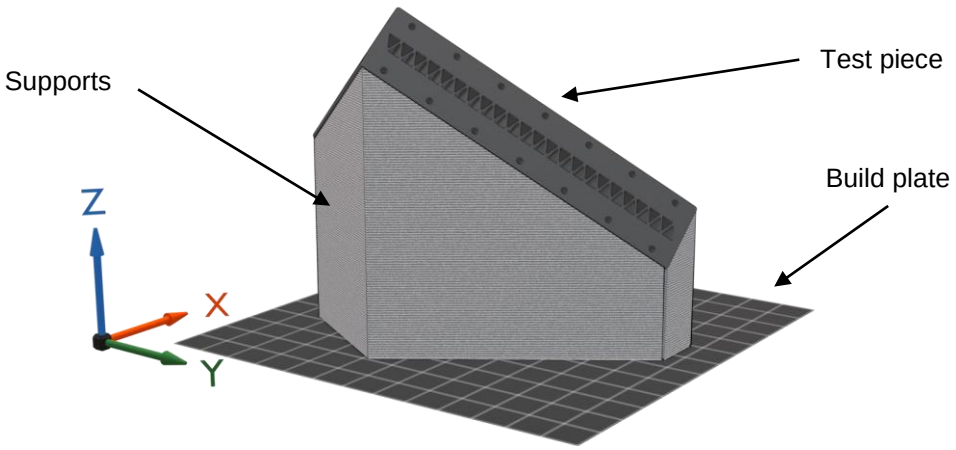

© Central University of Technology, Free State

Figure 52: Test piece build orientation

The test piece was successfully manufactured by CRPM, and the internal geometry was found to be free of any imperfections or warping during the build and heat-treatment processes. For this piece, the heat treatment consisted of heating under vacuum at 650 °C for three hours, followed by an immediate annealing cycle of 941 °C for two hours. A basic pressure test of the mock-up assembly of the as-built test piece found the assembly to be airtight across both the hot sides and cold side channels, with the front and side as-built test piece without supports shown in Figure 53, the hot side channel in Figure 54, and the cold side channels in Figure 55.

Figure 53: Test piece front and side views

Figure 54: Test piece hot side channels

© Central University of Technology, Free State

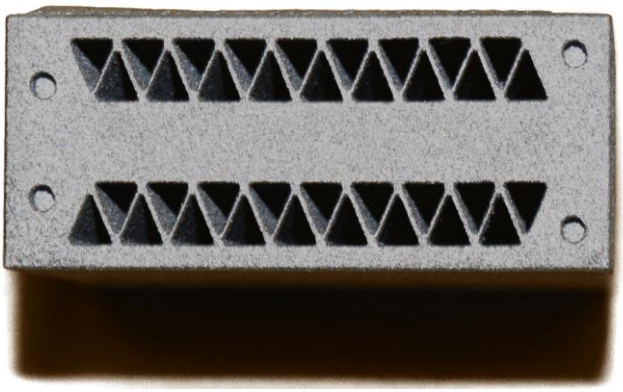

Figure 55: Test piece cold side channels

5.7 Test bench design and assembly

Based on the manufacture of the test piece, the set of manifolds seen in Figure 56 were designed and manufactured using nylon and processed on an EOS P110 Formiga SLS system.

Figure 56: SLS nylon printed manifolds

However, this choice turned out to be a poor one, as the manufactured nylon manifolds experienced a greater degree of deflection than initially anticipated based on the data provided in the material datasheets. Consequently, the assembly of the test piece failed under the required testing pressures. (Figure 57).

© Central University of Technology, Free State

Figure 57: SLS test piece assembly mock-up

New manifolds were designed to bolt over the test piece using 1 mm rubber gaskets and were manufactured on a CNC 3-axis milling machine from billet aluminium. The resulting manifolds for the hot side are shown in Figure 58, and the manifolds for the cold side in Figure 59.

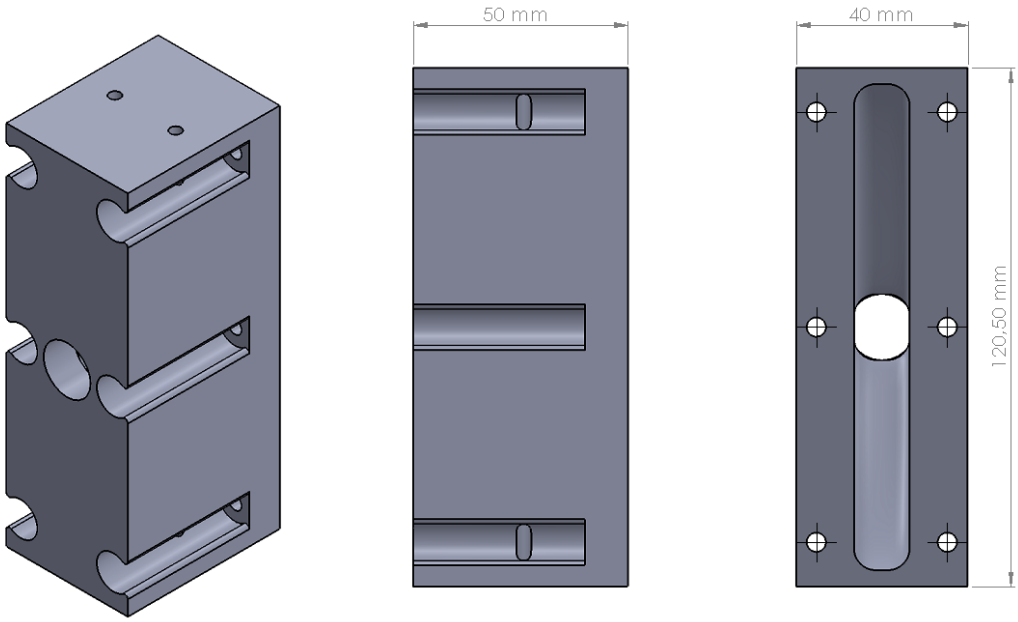

Figure 58: Hot side aluminium manifold

© Central University of Technology, Free State

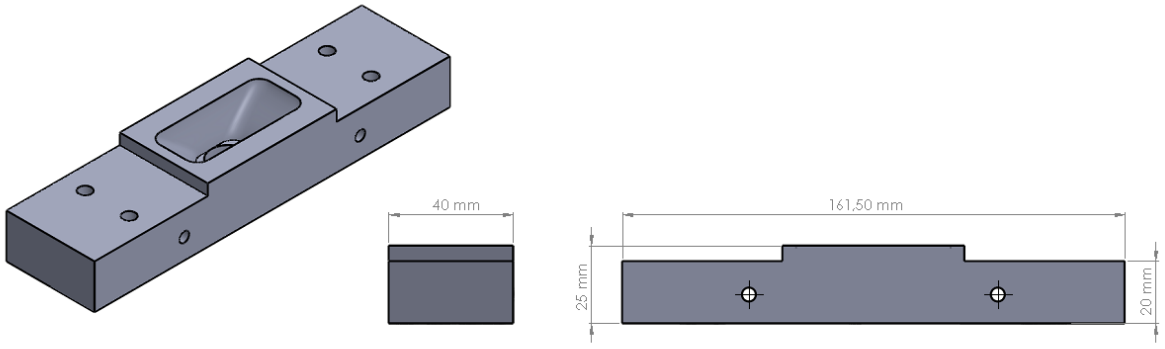

Figure 59: Cold side aluminium manifold

Figure 60 indicates the process of securing the aluminium manifolds onto the test piece with the gasket material.

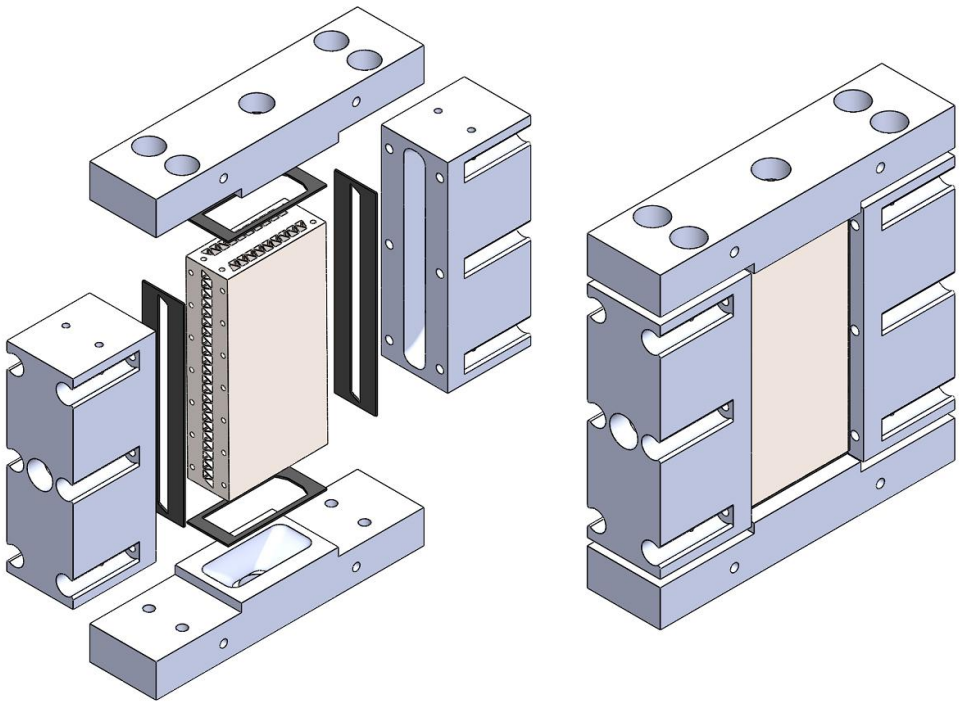

Figure 60: Test piece with manifold assembly

After successful manufacturing, the final test piece assembly displayed in Figure 61 was briefly pressure tested up to a pressure ceiling of 800 kPa to ensure there were no leaks or cross-contamination between the hot and cold side channels.

© Central University of Technology, Free State

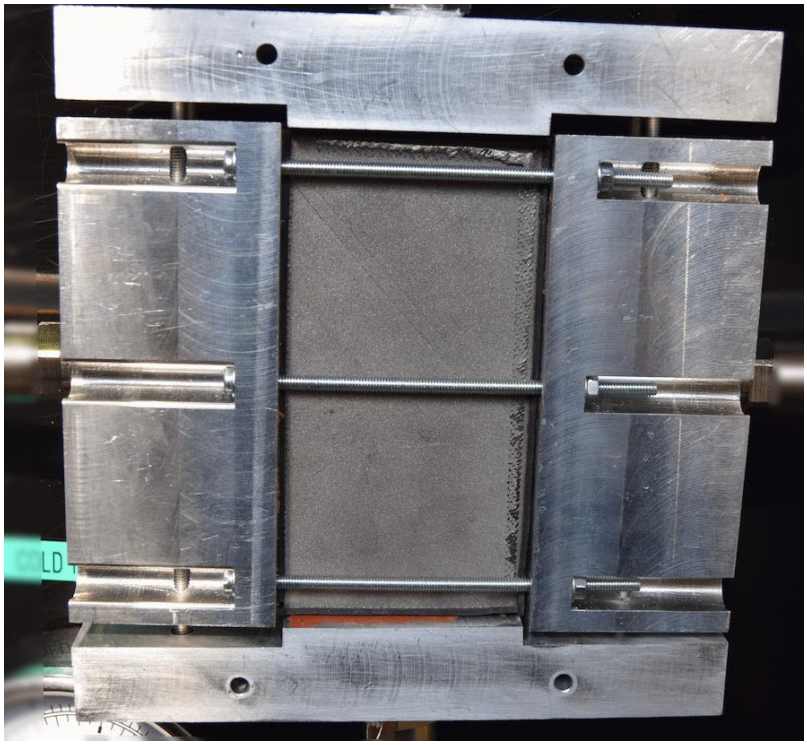

Figure 61: Test piece manifolds

Air supply

The compressed air supply for the test bench was provided by the compressor systems at the PDTS, with the compressor network consisting of two primary compressors seen in Figure 62 and Figure 63.

Figure 62: Compressor one

© Central University of Technology, Free State

Figure 63: Compressor two

The air supply provided by the two compressors was then piped to an aftercooler unit and an air dryer (Figure 64), which served to cool down the air supply to atmospheric conditions as well as reduce the humidity.

Figure 64: After-cooler unit (left) and air dryer unit (right)

The air compressor network was able to reliably supply an airflow of 190 l/min at a gauge pressure of 400 kPa during minimum load conditions. An issue that arose during testing was that, under high-stress conditions, the compressor networks would enter a deficit, leading to insufficient air production and draining the tanks. To prevent this issue, the testing process was limited to off-peak hours in the morning.

© Central University of Technology, Free State

Test bench

The completed test bench, which was designed and built in collaboration with PDTS, consisted of two separate airflow harnesses capable of independently varying pressure, flow rate, and temperature for both the hot and cold sides. Temperature and pressure gauges were mounted at the inlets and outlets of the hot and cold sides of the test piece, as presented in Figure 65, which shows the completed assembly.

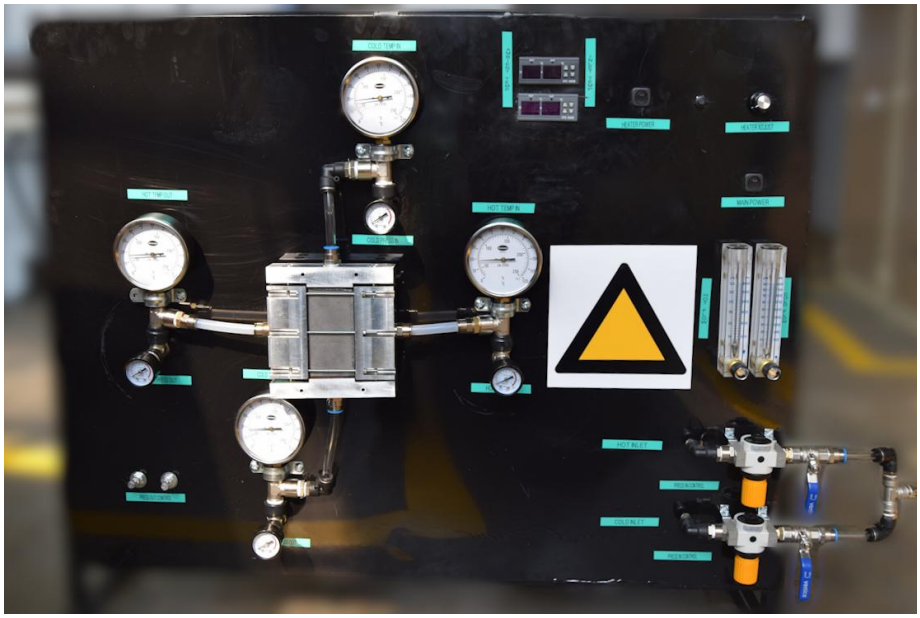

Figure 65: Test bench layout

The hot and cold side airlines were connected to the test piece via the aluminium manifolds, which were internally lined with silicone to reduce unwanted heat transfer through the manifolds. The test piece assembly, consisting of the test piece, aluminium manifolds, and pneumatic tubing, was then tightly wrapped in several layers of polyester insulation, as indicated in Figure 66, to prevent heat from escaping from the system. Additionally, a series of four thermistors connected to digital displays were installed inside the manifolds to assist the user in the operation of the test bench.

© Central University of Technology, Free State

Figure 66: Insulated manifolds

The hot side of the test bench was stepped down from the 1 MPa compressor airline using an inline pressure regulator to the gauge pressure required for each individual test, and the flow rate was then limited via two exit flow regulators indicated in Figure 67.

Figure 67: Exit flow regulators (right) and inlet pressure regulators (left)

The cold side of the test bench was allowed to vent into the atmosphere and was controlled by adjusting the flow regulator on the cold side flow meter shown in Figure 68.

© Central University of Technology, Free State

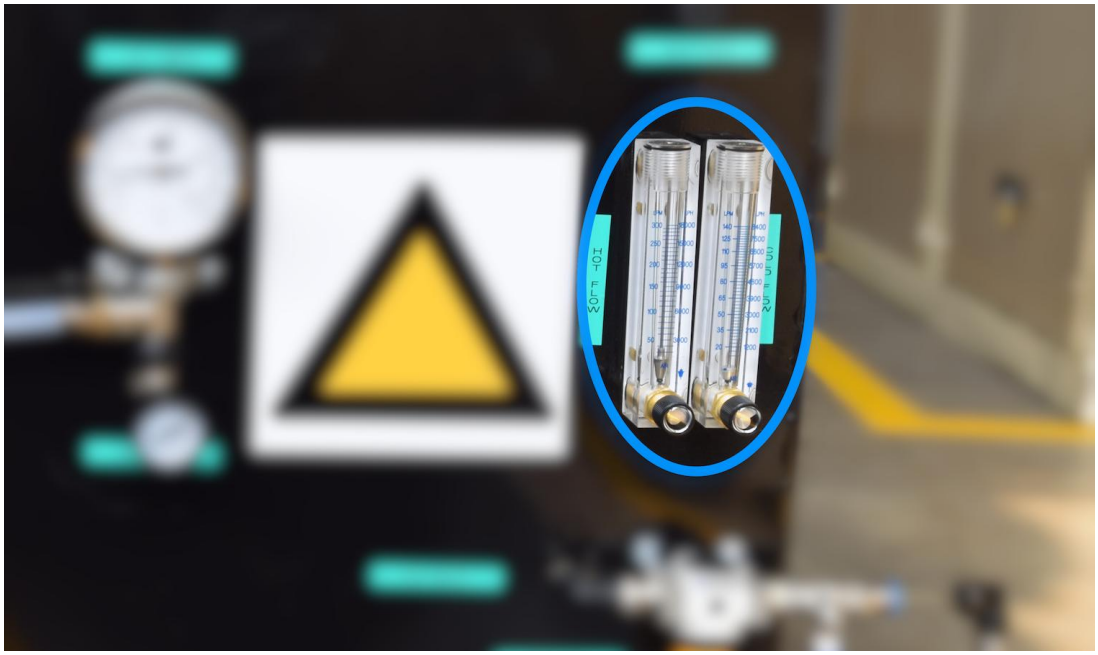

Figure 68: Hot and cold side flow meters/regulators

The hot side airline was heated by passing the pressurised air from the supply through a chamber containing a 1 kW air heating element regulated by a 4 kW silicon-controlled rectifier (SCR), as indicated in Figure 69. Due to heat escaping from the system, the air heating unit was also wrapped in polyester insulation, which also helped to prevent the possibility of injury caused by accidentally touching the heating chamber.

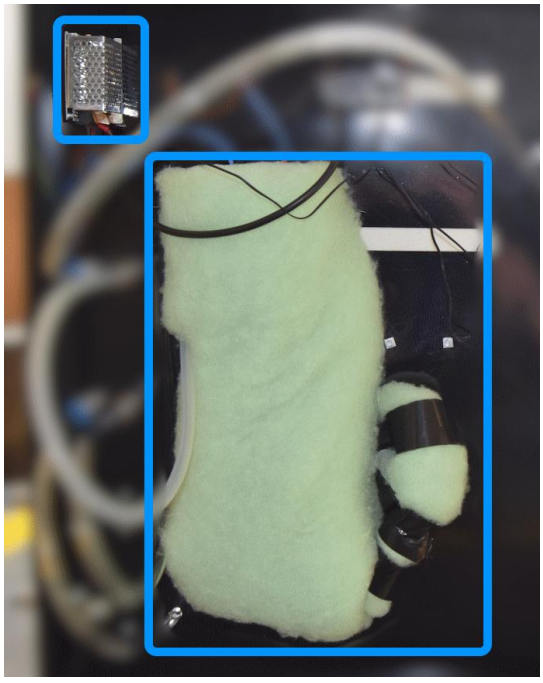

Figure 69: SCR unit (right) and air heating chamber (left)

© Central University of Technology, Free State

Initially, the testing process required that the pressure drop across the test piece be measured to evaluate results; however, in practice, it was discovered that the pressure drop across the test piece was too small to be accurately measured using the pressure gauges. Thus, the pressure drop measurements were removed from the testing methodology due to the DA methodology only covering temperature measurements. During initial testing and calibration, the test bench successfully reached a maximum temperature output in excess of 120 °C at the maximum testing conditions of 4 bar gauge pressure 190 l/min for the hot side. The cold side was ventilated into the atmosphere at a temperature of 17 °C up to a flow rate of 140 l/min.

5.8 Chapter summary

This chapter discussed the process followed to design a full-size multi-pass heat exchanger unit using the ε-NTU and Kays and London method. A single-passage design was then extracted from the full-size design and a Ti64 test piece was designed which would fulfil the requirements to verify the design. Dynamic similarity techniques based on dimensionless numbers was then utilised to obtain a series of equations which could be used to calculate the experimental testing conditions required to verify the test piece.

© Central University of Technology, Free State

CHAPTER 6

Experimental Results and Discussion

The aim of this chapter is to highlight the methodology by which the experimental test bench was used to match dynamic similarity constraints between the single passage and test piece designs.

6.1 Testing methodology

The experimental testing process required that the test bench be capable of matching DS constraints between the test piece and single-passage designs for a set period. Due to technical challenges experienced with maintaining the necessary flow rate for an extended period, a set of eight readings per test run was determined to be sufficient to plot the performance characteristics of the test piece. Following several trial runs of the test bench on the PDTS compressor system, a cool-down period of five minutes was implemented between data readings to minimise heat leakage caused by the bolts connecting the hot and cold side manifolds.

The testing procedure for each dataset was as follows:

1. Compressed air was supplied to both the hot and cold sides.
2. The required pressure and flow rate through the hot side was set by adjusting the input pressure regulator and the outlet flow rate regulators.
3. The required flow rate at atmospheric pressure through the cold side was set by adjusting the inlet flow regulator.
4. The heating element was powered on and set to the estimated power output required to obtain the desired temperature across the hot side.
5. The test bench was allowed to run uninterrupted for a minimum of 18 minutes allowing for thermal equilibrium to be reached between the hot and cold sides.
6. Temperature readings across at the inlet and outlets were recorded for both the hot and cold sides of the heat exchanger.
7. Heating element was shut off for five minutes to allow for test piece manifolds to cool.
8. Testing procedure was then repeated for subsequent temperature reading.

© Central University of Technology, Free State

6.2 Experimental results

6.2.1 Test scheduling

Due to the operational needs of the PDTS, all experimental testing was scheduled from 8h00 to 13h00 when the compressor network was at minimum draw and the air tanks were full.

6.2.2 Dynamic similarity targets

Please note that the expected heat transfer across the scaled test piece were obtained via the DA process indicated under heading 5.5 and are not obtained directly from the design methodology for the full size and single passage heat exchanger designs.

From the DA process explained under heading 5.5, it was found that to match similarity constraints between the single-passage design and the test piece, the test piece would need to be run at a consistent volumetric flow rate of 184 l/min on the hot side, and 136 l/min on the cold side. These parameters remained unaffected by either temperature or pressure and remained the same across the individual temperature targets for the datasets. However, the pressure of the hot side airline was found to be directly affected by temperature, thus the pressure of the hot side was recalculated for each measurement based on the temperature required for that particular measurement.

6.2.3 Temperature variance

Initially, the operating procedure for the test bench required that testing occur in increments of 5 °C from 30 °C up to 120 °C. However, in practice it was found to be difficult to get precise temperature readings due to the manual adjustments required to set the temperature. To counteract this effect, an initial estimate would be run at the required flow rates and pressures and the temperature of the hot side would be allowed to equalise. The process explained under heading 5.5 would then be repeated using the equalised temperatures to obtain the theoretically expected heat transfer across the test piece which could be compared to the experimentally measured temperature at the outlet of the cold side.

© Central University of Technology, Free State

6.2.4 Test 1 results

The first test was performed on the 9th of August 2024 between 08h00 and 13h00. The ambient temperature increased from 7.2 °C at 08h00 to 15.3 °C at 13h00. The results for the individual measurements recorded in Test 1 are listed in Table 11, with the experimental and theoretical cold side outlet temperatures plotted in Figure 70. The test proceeded well without any unforeseen issues, with minimum draw noted on the compressors, which allowed for steady flow rates and temperature readings across measurements.

Table 11: Test 1 data

Measurement number	1	2	3	4	5	6	7	8
$\dot{VOL}_h$ (l/min)	184	184	184	184	184	184	184	184
$\dot{VOL}_c$ (l/min)	136	136	136	136	136	136	136	136
$P_{h,i}$ (gauge) (bar)	2.913	2.987	3.073	3.271	3.382	3.505	3.579	3.702
$T_{h,i}$ (C°)	46	52	59	75	84	94	100	110
$T_{h,o}$ (C°)	41	46	52	65	73	81	87	97
$T_{c,i}$ (C°)	17	17	17	17.5	17.5	17.5	18	18.5
$T_{c,o}$ (Experimental) (C°)	27	28.5	31.5	36.5	39.5	43.5	46	50
$T_{c,o}$ (Theoretical) (C°)	26.867	28.909	31.290	37.064	40.127	43.529	45.900	49.633
% Error	-0.49%	1.41%	-0.67%	1.52%	1.56%	0.07%	-0.22%	-0.74%

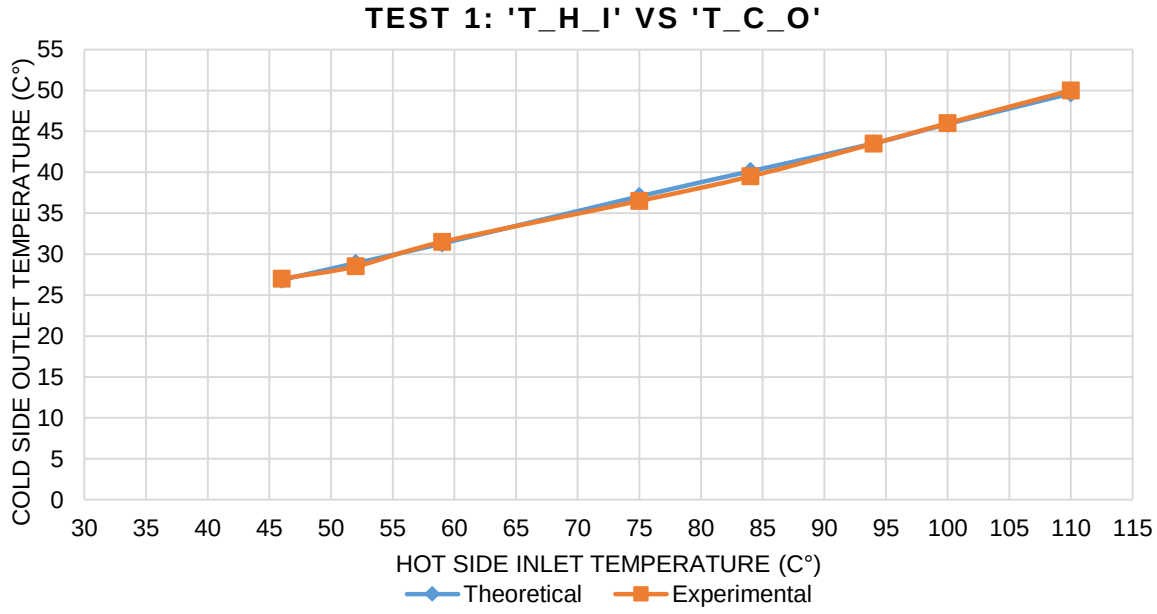

Figure 70: Test 1, cold side outlet temperature vs hot side inlet temperature

© Central University of Technology, Free State

6.2.5 Test 2 results

The second test was performed on the 12th of August 2024 between 09h00 and 13h00. The ambient temperature increased from 11.4 °C at 09h00 to 17.8°C at 13h00. The results for the individual measurements recorded in Test 2 are set out in Table 12, with the experimental and theoretical cold side outlet temperatures plotted in Figure 71.

Following completion of the test, it was discovered that the muffler unit used to reduce the noise emitted by the test bench had malfunctioned and was preventing the exhaust heat from being correctly expelled. The malfunctioning muffler was subsequently repaired and testing resumed.

Table 12: Test 2 data

Measurement number	**1**	**2**	**3**	**4**	**5**	**6**	**7**	**8**
$\dot{VOL}_h$ **(l/min)**	184	184	184	184	184	184	184	184
$\dot{VOL}_c$ **(l/min)**	136	136	136	136	136	136	136	136
$P_{h,i}$ **(gauge) (bar)**	2.740	2.950	3.135	3.258	3.332	3.419	3.456	3.517
$T_{h,i}$ **(C°)**	32	49	64	74	80	87	90	95
$T_{h,o}$ **(C°)**	31	44.5	56	65.5	70	77	80	84
$T_{c,i}$ **(C°)**	18	18	18	18	18	18.5	19	19
$T_{c,o}$ **(Experimental) (C°)**	24	30	35	38.5	41	43.5	45	46.54
$T_{c,o}$ **(Theoretical) (C°)**	22.763	28.548	33.651	37.054	39.095	41.807	43.158	44.859
% Error	-5.43%	-5.09%	-4.01%	-3.90%	-4.87%	-4.05%	-4.27%	-3.75%

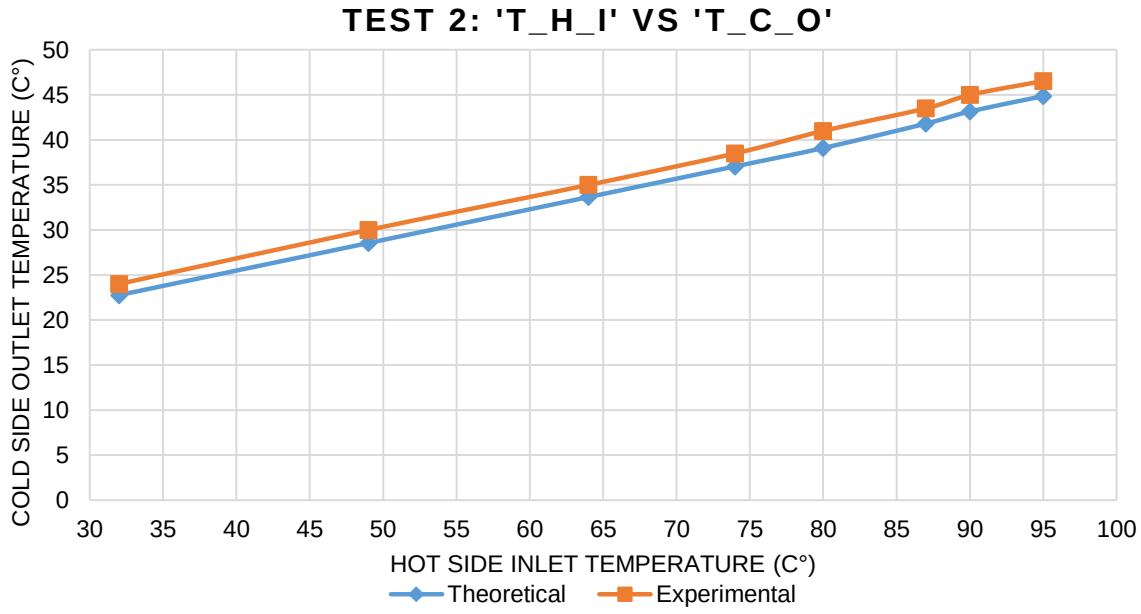

Figure 71: Test 2, cold side outlet temperature vs hot side inlet temperature

© Central University of Technology, Free State

6.2.6 Test 3 results

The third test was performed on the 13th of August 2024 between 07h30 and 13h00. The ambient temperature increased from 8.8 °C at 07h30 to 21.8 °C at 13h00. The results for the individual measurements recorded in Test 3 are recorded in Table 13, with the experimental and theoretical cold side outlet temperatures plotted in Figure 72.

During the test, fluctuations in the temperature of the compressors' air were noted compared to the previous two tests due to high airflow consumption from PDTS manufacturing equipment.

Table 13: Test 3 data

Measurement number	**1**	**2**	**3**	**4**	**5**	**6**	**7**	**8**
$\dot{VOL}_h$ **(l/min)**	184	184	184	184	184	184	184	184
$\dot{VOL}_c$ **(l/min)**	136	136	136	136	136	136	136	136
$P_{h,i}$ **(gauge) (bar)**	2.777	2.864	2.993	3.147	3.221	3.345	3.456	3.665
$T_{h,i}$ **(C°)**	35	42	52.5	65	71	81	90	107
$T_{h,o}$ **(C°)**	32	39	47	57	63	71	80	94
$T_{c,i}$ **(C°)**	17	17	17.5	18	18	18	18.5	19
$T_{c,o}$ **(Experimental) (C°)**	24	26	29.5	34.5	36.5	40	44	50
$T_{c,o}$ **(Theoretical) (C°)**	23.124	25.506	29.409	33.992	36.033	39.436	42.828	48.942
% Error	-3.79%	-1.94%	-0.31%	-1.50%	-1.30%	-1.43%	-2.74%	-2.16%

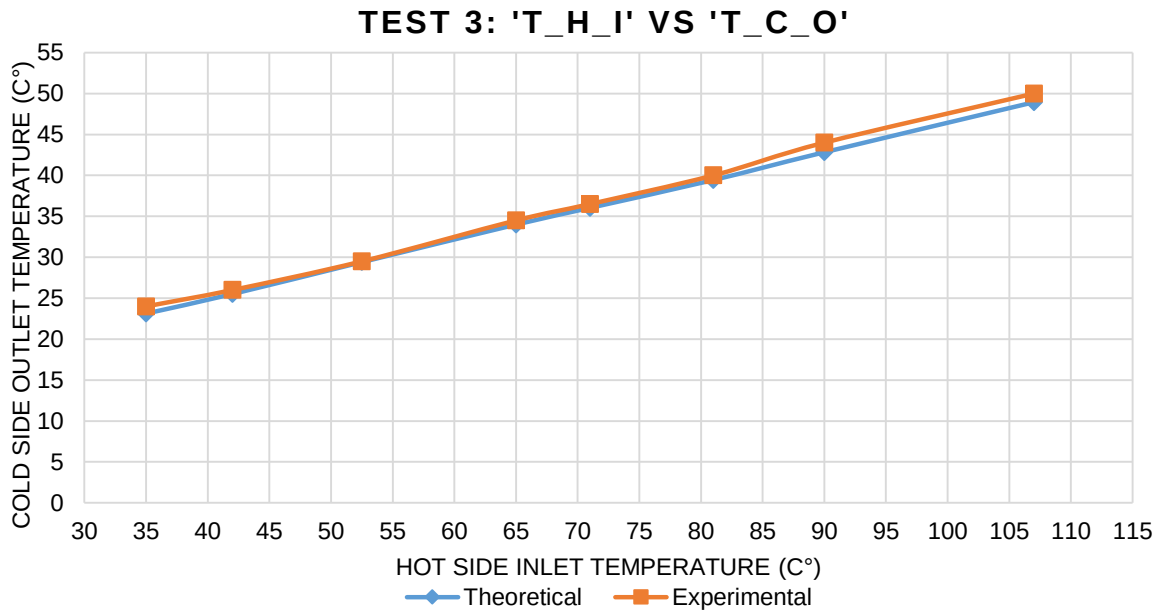

Figure 72: Test 3, cold side outlet temperature vs hot side inlet temperature

© Central University of Technology, Free State

6.2.7 Test 4 results

The fourth test was performed on the 14th of August 2024 between 09h00 and 13h00. The ambient temperature increased from 8.5 °C at 09h00 to 15.6 °C at 13h00. The results for the individual measurements recorded in Test 4 are indicated in Table 14, with the experimental and theoretical cold side outlet temperatures plotted in Figure 73.

Due to delays in getting the compressor lines up to the required testing pressure, the procedure was accelerated to finish in the allotted time. This resulted in less time to equalise between individual readings which affected the overall accuracy of results.

Table 14: Test 4 data

Measurement Number	**1**	**2**	**3**	**4**	**5**	**6**	**7**	**8**
$\dot{VOL}_h$ **(l/min)**	184	184	184	184	184	184	184	184
$\dot{VOL}_c$ **(l/min)**	136	136	136	136	136	136	136	136
$P_{h,i}$ **(gauge) (bar)**	2.765	2.999	3.160	3.308	3.456	3.542	3.678	3.764
$T_{h,i}$ **(C°)**	34	53	66	78	90	97	108	115
$T_{h,o}$ **(C°)**	32	47	58	69	80	85	95	100
$T_{c,i}$ **(C°)**	18	18	18	18	18	18	18	18
$T_{c,o}$ **(Experimental) (C°)**	24	29	34.5	39.5	43.5	45.5	49.5	52
$T_{c,o}$ **(Theoretical) (C°)**	23.444	29.909	34.332	38.415	42.498	44.880	48.622	51.004
% Error	-2.37%	3.04%	-0.49%	-2.82%	-2.36%	-1.38%	-1.80%	-1.95%

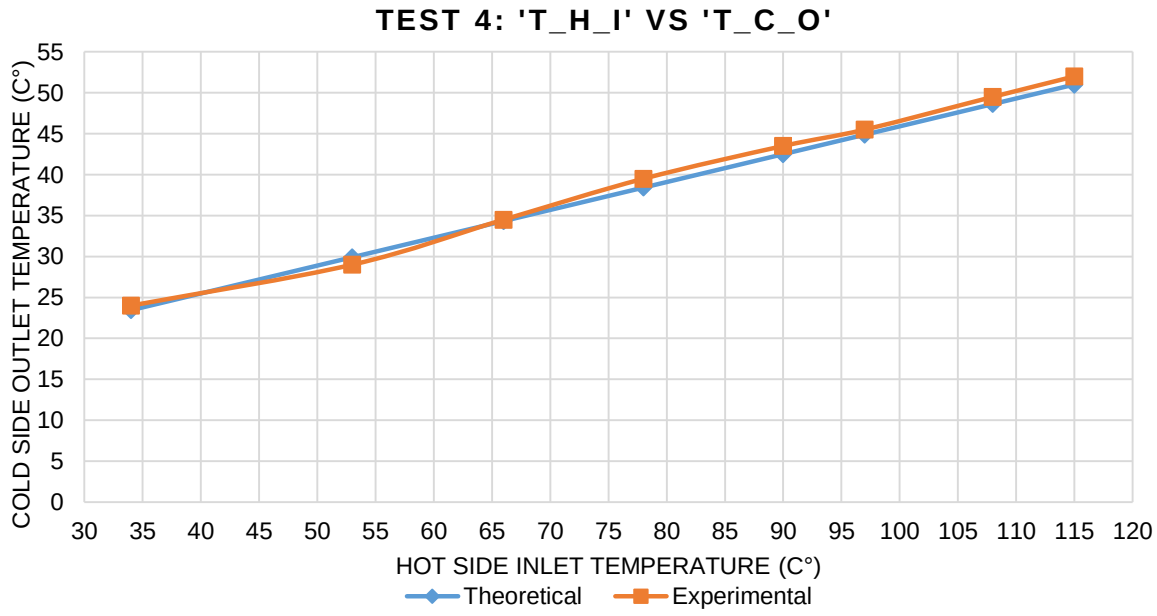

Figure 73: Test 4, cold side outlet temperature vs hot side inlet temperature

© Central University of Technology, Free State

6.2.8 Test 5 results

The fifth test was performed on the 15th of August 2024 between 09h30 and 13h45. The ambient temperature increased from 12 °C at 09h30 to 15.6 °C at 13h45. The results for the individual measurements recorded in Test 5 are shown in Table 15, with the experimental and theoretical cold side outlet temperatures plotted in Figure 74.

Due to scheduling issues, the test was run later than previous ones which caused high flow demand on the compressors. The air tanks were fully draining at approximately 12h00 causing the compressors to intermittently start and stop to maintain the required airline pressure, which significantly affected the consistency of the airflow rates.

Table 15: Test 5 data

Measurement number	**1**	**2**	**3**	**4**	**5**	**6**	**7**	**8**
$\dot{VOL}_h$ **(l/min)**	184	184	184	184	184	184	184	184
$\dot{VOL}_c$ **(l/min)**	136	136	136	136	136	136	136	136
$P_{h,i}$ **(gauge) (bar)**	2.802	3.012	3.197	3.295	3.443	3.530	3.628	3.801
$T_{h,i}$ **(C°)**	37.00	54.00	69.00	77.00	89.00	96.00	104.00	118.00
$T_{h,o}$ **(C°)**	35.00	47.00	60.00	68.00	79.00	85.00	91.00	103.00
$T_{c,i}$ **(C°)**	17	17	17	17.5	18	18	18	18
$T_{c,o}$ **(Experimental) (C°)**	25	29.5	35	38	43	46	49	54
$T_{c,o}$ **(Theoretical) (C°)**	23.805	29.589	34.693	37.745	42.158	44.539	47.261	52.025
% Error	-5.02%	0.30%	-0.88%	-0.68%	-2.00%	-3.28%	-3.68%	-3.80%

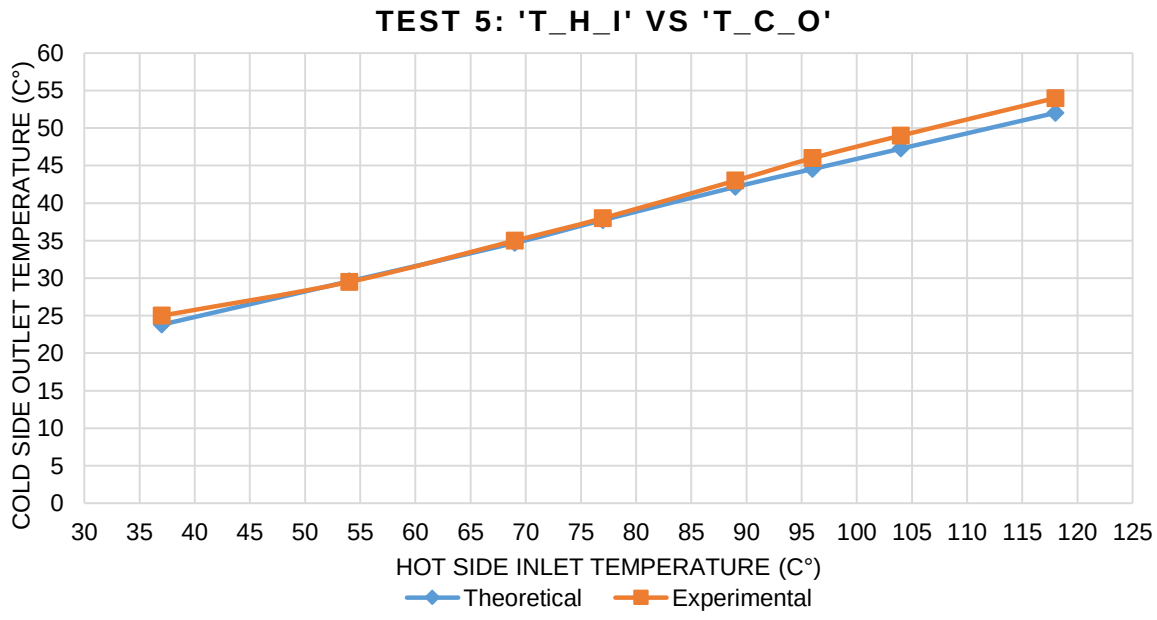

Figure 74: Test 5, cold side outlet temperature vs hot side inlet temperature

© Central University of Technology, Free State

6.2.9 Test 6 results

The sixth test was performed on the 19th of August 2024 between 07h30 and 11h30. The ambient temperature increased from 13 °C at 07h30 to 23 °C at 11h30. The results for the individual measurements recorded in Test 5 are indicated in Table 16, with the experimental and theoretical cold side outlet temperatures plotted in Figure 75.

The accuracy of the results was affected by an increase in the ambient air temperature as it was the only test where the air supplied from the compressors reached a temperature of 20 °C.

Table 16: Test 6 data

Measurement number	1	2	3	4	5	6	7	8
$\dot{VOL}_h$ (l/min)	184	184	184	184	184	184	184	184
$\dot{VOL}_c$ (l/min)	136	136	136	136	136	136	136	136
$P_{h,i}$ (gauge) (bar)	2.765	3.024	3.221	3.394	3.493	3.542	3.628	3.826
$T_{h,i}$ (C°)	34	55	71	85	93	97	104	120
$T_{h,o}$ (C°)	32	47	60	72	81	87	90	104
$T_{c,i}$ (C°)	18	18	18	18	18.5	19	19.5	20
$T_{c,o}$ (Experimental) (C°)	24.5	30	36	42	45.5	47.5	50	58
$T_{c,o}$ (Theoretical) (C°)	23.444	30.589	36.033	40.797	43.849	45.539	48.251	54.025
% Error	-4.50%	1.93%	0.09%	-2.95%	-3.77%	-4.31%	-3.62%	-7.36%

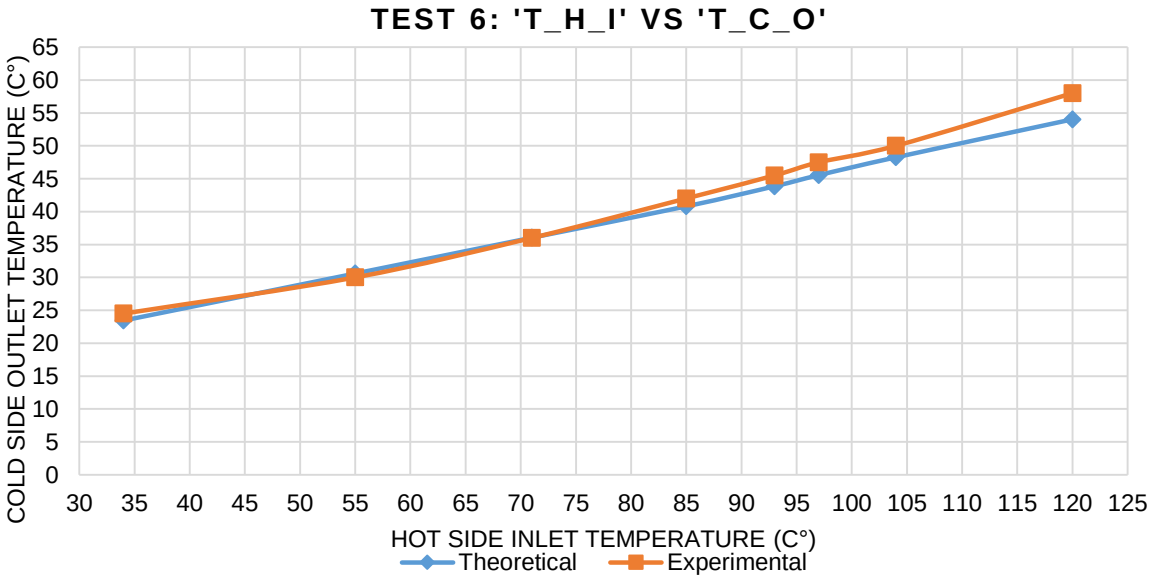

Figure 75: Test 6, cold side outlet temperature vs hot side inlet temperature

© Central University of Technology, Free State

6.3 Combined results

The combined readings for all six tests were then plotted on a single graph supported by trend lines to ascertain the effectiveness of the experimental testing methodology. This combined graph is shown in Figure 76.

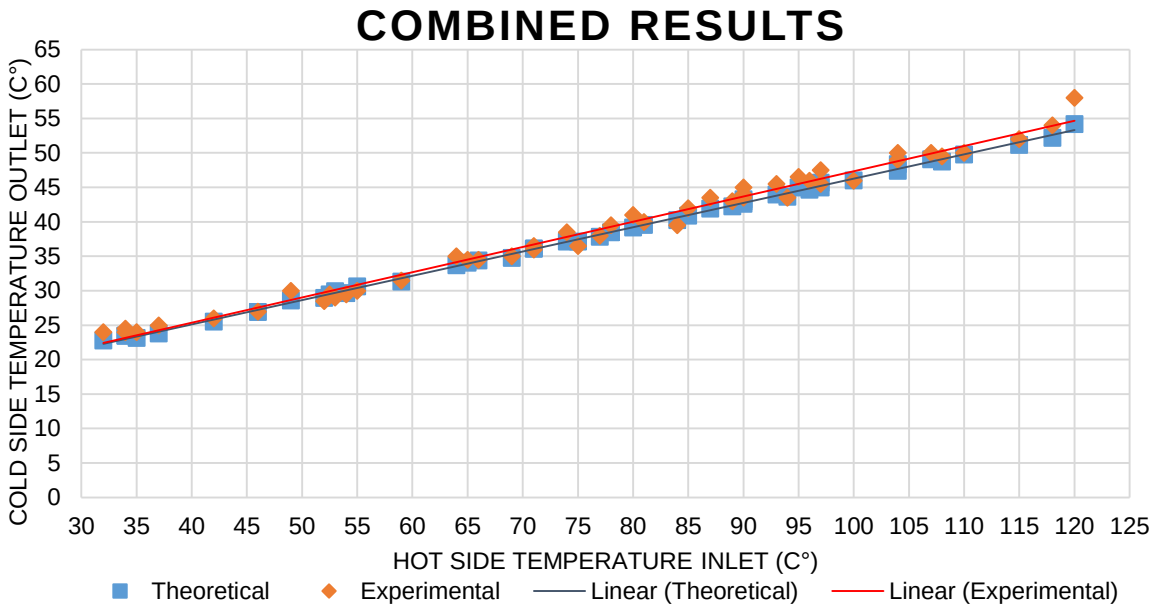

Figure 76: Combined cold side outlet temperatures vs hot side inlet temperatures

6.4 Discussion

During the test phase of the study, several observations were made, which were deemed to be of enough importance to merit additional discussion.

Flow rate measurements

The measurement of the flow rates proved to be significantly more difficult than initially expected due to the sensitivity of the test bench, with the pressure and temperature of the air passing through the hot side harness causing substantial changes in the volumetric flow rate of the air. Thus, the pressures and flow rates had to be continually recalibrated to achieve the correct flow rates, which posed a risk of human error in the data. Future attempts need to more effectively account for flow variations to achieve consistent results.

© Central University of Technology, Free State

Effect of surface roughness on heat transfer

Due to the selected design methodology utilising the Kays and London method to design the heat exchangers, several technical limitations were present, which were initially unaccounted for. Of note was the exact effect the surface roughness would have on the effectiveness of the heat exchanger.

Due to the test piece being tested in an as-built state, the internal channels had a much higher surface roughness than expected, which resulted in a larger heat transfer area than the theoretical model. This effect could possibly explain why the testing process consistently recorded slightly higher heat transfer rates than expected at higher temperatures across the hot side.

Effect of humidity on testing methodology

A topic that was raised during the development of the test bench was the effect that the humidity of the air in the compressor airlines would have on the performance characteristics of the test piece. Since humidity is defined as the amount of water vapour present in a particular quantity of air, it stands to reason that humid air affects the specific heat capacities of the hot and cold sides.

One of the limitations of the testing methodology by Sánchez-Escalona et al. [37] is the specific heat capacity for both the hot and cold side fluids of the heat exchanger were assumed to remain constant. However, during testing, the humidity of the air in the compressed airline was dependent on and greatly affected by the amount of strain being placed on the air drying unit and the aftercooler connected to the air compressors at PDTS. The variation could theoretically have impeded the accuracy of the results.

Evaluation of dynamic similarity

As was mentioned in the previous chapter, complete DS was not possible between the single-passage and test-piece designs due to issues obtaining exact force-scale equivalence within the model. However, geometric and kinematic similarity conditions were met, which allowed for testing conditions at specific flow rates to be obtained for temperatures ranging from 30 °C to 120 °C.

© Central University of Technology, Free State

Evaluation of experimental data

From the data for Test 1 in Figure 70, a similar curve was observed between the expected theoretical and measured experimental results. The curve for Test 1 remained constant between readings and is considered the most accurate dataset obtained from the testing process. The accuracy of these results may be attributed to the lower ambient temperature as well as a lower flow rate of air being drawn from the compressors.

From the data for Test 2 in Figure 71, a constant curve was observed between the expected and measured results. However, the experimental readings were all out by an error margin of approximately 5% higher than expected. This difference was attributed to the noise muffler unit, which failed under higher testing temperatures, resulting in excess heat being retained by the system. Once the failed muffler was replaced with an alternative design, the quality of the results returned to the expected levels.

From the data for Test 3 in Figure 72, a constant curve was observed between the expected and measured results. Unlike the previous two tests, PDTS had resumed normal manufacturing which caused additional load to be placed on the compressor system, the effect of which was a larger variation in the inlet temperature of the air supplied by the compressors.

From the data for Test 4 in Figure 73, an approximate curve was observed between the expected and measured results. Test 4 constituted the poorest data set with the largest variation in the fit of the curve. The hypothesised reason for this variation was due to the shorter testing period for the dataset, which resulted in complete equilibrium between the hot and cold sides not being reached for some temperature readings.

From the data for Test 5 in Figure 74, an approximate curve was observed between the expected and measured results. Test 5 turned out to be the most difficult dataset to record because the compressor lines were overstressed on that day. The effect of this was a minor fluctuation in the flow rate through the airlines caused by the compressor motors turning on intermittently to maintain the pressure in the system.

© Central University of Technology, Free State

From the data for Test 6 in Figure 75, the curve showed the highest deviation between the expected and measured results. Test 6 constituted the warmest day during the testing period, with the ambient temperature reaching 23 °C by 11h30 and the temperature in the airlines rising to 20 °C, which resulted in a larger error variance at hotter temperature readings.

6.5 Chapter summary

By comparing the results for Tests 1 through 6 in Figure 76, it can be concluded that there is a substantial correlation between the theoretical results obtained via calculations and the experimental results obtained from the testing process. This shows that the proposed DA methodology successfully predicted the performance characteristics of the test-piece and single-passage designs using DS constraints, thereby approximating the performance characteristics of the full-scale design.

© Central University of Technology, Free State

CHAPTER 7

Conclusions

The aim of this chapter is to reflect on the findings of the study and provide conclusions as well as recommending future work on the topic of applying intercooling modifications into turboshaft engines.

7.1 Conclusion

The aim of this study was achieved wherein an LPBF-manufactured heat exchanger was successfully designed for use in a benchmark aeronautical turboshaft engine. To this end, the Brayton gas cycle utilised in the study was able to characterise the benchmark engine and provide the unknown parameters required to complete the design process for the heat exchangers. The Kays and London method for designing heat exchangers was then used to design and size the conceptualised heat exchanger units, which would have the capacity to cool the charge air supplied by the compressor stage of the benchmark engine by an estimated 29 °C using the assumed cooling source. Then an EOS M290 LPBF system was used to successfully manufacture an extracted test-piece segment at half scale using Ti64, and a test bench was designed to experimentally verify the test-piece segment. The test bench was found to be capable of reaching the desired testing temperatures, pressures, and flow rates required to match DS constraints between the single passage design and the test piece. The experimental testing procedure applied in this study was found more effective than initially expected, with a notable correspondence between the theoretical and experimental data, which was then used to draw conclusions on the efficacy of the full-size design. However, the inefficiency of AM-based heat exchangers compared to traditionally manufactured ones is noted due to the inherent difficulty of using materials with high thermal conductance in the LPBF process. Therefore, future AM heat exchangers will need to either utilise a different material or adopt a design methodology optimised for the LPBF process.

While there are benefits to be gained by installing AM-based intercooling modifications in turboshaft engines, such as an increase in power output and lower running temperatures, it was also found that improperly applying these

© Central University of Technology, Free State

modifications could lead to an increase in fuel consumption and emissions. To reduce the negative effects, such an intercooler system should have the capability to turn off when not needed, thereby enhancing fuel efficiency.

From the research conducted during this study, there is potential for AM-based heat exchangers in aeronautical turboshaft engines, but further research into the topic outside the scope of this study will be required.

7.2 Addressed objectives

The aim of the study was to design an LPBF-manufactured Ti64 heat exchanger that could remove heat produced by the compressor stage of a turboshaft engine. To achieve this aim, a set of objectives was drawn up in the introduction to break down the challenges involved into several smaller topics that could be individually investigated and addressed.

1. Characterisation of a benchmark turboshaft engine using Brayton gas cycle.

A basic Brayton gas cycle was applied for use in characterising the performance characteristics of the selected benchmark engine. The approach used was applicable to the twin-spool layout, wherein the compressor stage of the engine was connected to a separate high-power turbine used in the benchmark engine. It should be noted that if the same approach were to be applied to other turboshaft engine layouts, the Brayton gas cycle would need to be adjusted accordingly. From Chapter 3, it was found that charge air supplied by the compressor of the benchmark engine would theoretically undergo an estimated 234.7 °C increase in temperature at the operating flow rate of 1.638 kg/s and operating pressure of 628.215 kPa.

2. Design and fabrication of a scaled test-piece heat exchanger manufactured using Ti64.

Due to several limitations imposed on the study, the mesh for the full-size design had to be capable of being manufactured at half scale to reduce costs. To fulfil this requirement, a larger mesh was selected for the core of the heat exchanger, which

© Central University of Technology, Free State

ultimately resulted in a less effective heat exchanger when compared to more compact designs. Adjustments were then made to the Kays and London method to account for the change in material, an increase in wall thickness, and the modified profile for the individual cells of the heat exchanger to enhance the accuracy of the theoretical results. A set of two identical heat exchanger units was then sized to fill the available space between the compressor and combustor units of the benchmark engine, with each unit being able to handle half of the total mass flow rate through the benchmark engine. The resulting heat exchanger units obtained from the design process would be theoretically able to cool the charge air supplied by the compressor by approximately 29 °C at a mass flow rate of 0.819 kg/s.

3. Experimental verification of test piece using DA and DS techniques.

A test-piece segment was extracted from the full-size design and manufactured at the required scale using Ti64. Splitting the test piece assembly into individual components was the right choice, as it enabled modifications on individual parts without reprinting the entire assembly. The test bench was then designed to replicate the testing conditions required to experimentally verify the test piece using DA and DS principles. The testing process indicated a strong correspondence between the theoretical results and the collected experimental data, revealing an average error margin of 1.5%. The conclusion was drawn that the full-scale design would have similar performance characteristics to the verified single-passage designs.

4. Analysis of potential benefits and drawbacks to installing the designed intercooler in turboshaft cycles.

Although the exact effects the hypothesised system would have on the benchmark engine requires additional research, several observations can be made. The full-size multi-pass intercooler design consisting of the two separate units could theoretically result in an approximate 12% reduction in the temperature of the charge air supplied to the combustor unit. The reduced temperature would result in an improvement in the quality of air being supplied to the engine, as well as

© Central University of Technology, Free State

improving the cooling effects within the combustor lining. Unfortunately, due to the scope limitations of the project, this study cannot investigate the exact effects the desired system would have on a real-world engine.

Although AM techniques have numerous advantages when it comes to rapid prototyping, additively manufactured Ti64 is not an optimal material for heat exchangers due to high manufacturing costs, low thermal conductivity, and the inherent challenges involved in printing parts with complex internal overhangs. Therefore, a more efficient heat exchanger could be designed utilising a more compact conventionally manufactured heat exchanger, and a thermally conductive material such as aluminium or copper could significantly enhance the overall efficacy of the intercooler system.

A negative aspect that was highlighted in this study was the effect that an intercooler could have on the fuel economics of a turboshaft engine; specifically, a reduction in the temperature of the air entering the combustor unit would reduce the thermal efficiency of the engine. Thus, the engine would have a higher power output and better performance, but at the cost of fuel economy, as well as an increase in greenhouse emissions caused by an incomplete combustion process.

5. Hypothesis of an optimised modification using data that could be applied to turboshaft engines.

Because the hypothesised intercooler design would increase performance at the cost of fuel economy, it stands to reason that the intercooler design would be most beneficial under short-term, high-power output circumstances such as those that are present during the take-off of a helicopter. Thus, any intercooler modifications applied to aeronautical turboshaft engines would require the capability to turn off when not in use, which would greatly affect the versatility of the system. Further research will be required to address these issues before the concept can be feasibly applied to existing turboshaft engines.

© Central University of Technology, Free State

7.3 Recommendations for future work

The study indicated potential for the use of heat exchangers in aeronautical turboshaft engines. However, several important points were highlighted that are crucial for future work on the topic.

1. Although the Kays and London method has proved to be a reliable method in the design of heat exchangers, it is a poor choice for AM since it does not properly leverage the potential of modern manufacturing techniques such as LPBF. The primary example is the emphasis on straight channels, which are very vulnerable to warping during the LPBF process [5]. Therefore, using an updated design methodology for heat exchangers, which is specifically optimised for the LPBF process, is recommended.
2. The experimental methodology based on the Buckingham-Pi method was successfully able to predict the performance of the test piece using DS constraints; however, the limiting constraint was that both the test-piece segment and single-passage designs had to be made of the same material. An expanded methodology could account for the thermal conductivity of the material, which will allow for heat exchangers made using non-metallic processes such as SLS to verify metal.
3. Due to the conclusion that an intercooler system alone would not be beneficial over long-term use, such a system would need to be combined with a waste heat recuperation system to offset the negative effects. An optimised system that could attain this is an intercooler-recuperator hybrid system, wherein a set of heat exchangers act as intercoolers while the turboshaft engine is grounded during take-off, then switches to a waste heat recuperator when at altitude.
4. The effect of the surface roughness of AM Ti64 was not quantified in this study and would have a notable effect on the performance characteristics of heat exchangers in a practical setting. Thus a future study on this topic is recommended.

© Central University of Technology, Free State

BIBLIOGRAPHY

[1] H. Aygun, “Effects of air to fuel ratio on parameters of combustor used for gas turbine engines: Applications of turbojet, turbofan, turboprop and turboshaft,” *Energy*, vol. 305, p. 132346, Oct. 2024, doi: 10.1016/J.ENERGY.2024.132346.

[2] O. Balli and H. Caliskan, “Investigating renewable and sustainable biofuel and biofuel/diesel blends utilizations in a turboshaft engine used on helicopters,” *Energy*, vol. 306, p. 132424, Oct. 2024, doi: 10.1016/J.ENERGY.2024.132424.

[3] R. Andriani, F. Gamma, and U. Ghezzi, “Regeneration and intercooling in gas turbine engines for propulsion systems,” in *44th AIAA/ASME/SAE/ASEE Joint Propulsion Conference and Exhibit*, 2008, p. doi: 10.2514/6.2008-4899.

[4] A. P. Mattos and W. L. R. Gallo, “A study of the influence of the intercooled turbocharger and cooled exhaust gas recirculation on the performance parameters of an ethanol-fueled engine,” *Int. J. Thermodyn.*, vol. 22, no. 3, pp. 149–157, 2019, doi: 10.5541/ijot.499892.

[5] S. Venter and G. Jacobs, “Development and characterisation of a ti6al4v additive manufactured compact counter-flow heat exchanger for application in organic rankine cycles,” in *RAPDASA 2019 Conference Proceedings*, 2019, pp. 262–275.

[6] ROLLS-ROYCE, *The Jet Engine*, 6th ed. Wiley, 2019.

[7] J. P. Holman, *Heat Transfer*, 10th ed. New York: McGraw-Hill Education Pvt Limited, 2010.

[8] S. L. Dixon and C. A. Hall, *Fluid mechanics and thermodynamics of turbomachinery, 7th edition*, 7th ed. Elsevier Inc., 2013. doi: 10.1016/C2011-0-05059-7.

[9] M. T. Schobeiri, “Turbomachinery Flow Physics and Dynamic Performance,” *Turbomach. Flow Phys. Dyn. Perform.*, 2012, doi: 10.1007/978-3-642-24675-3.

[10] G. Jacquet-Richardet *et al.*, “Rotor to stator contacts in turbomachines.

© Central University of Technology, Free State

Review and application," *Mech. Syst. Signal Process.*, vol. 40, no. 2, pp. 401–420, 2013, doi: 10.1016/j.ymssp.2013.05.010.

[11] A. F. El-Sayed, *Fundamentals of aircraft and rocket propulsion*, 1st ed. London: Springer-Verlag, 2016. doi: 10.1007/978-1-4471-6796-9.

[12] A. Fakhre, V. Pachidis, I. Goulos, M. Tashfeen, and P. Pilidis, "Helicopter mission analysis for a regenerated turboshaft," in *Proceedings of the ASME Turbo Expo*, 2013. doi: 10.1115/GT2013-94971.

[13] Rolls-Royce Corporation, "RR300 Turboshaft Factsheet," Rolls-Royce Corporation, 2016. [Online]. Available: https://www.rollsroycefirstnetwork.com/product-and-brochure-information

[14] J. Lebre and F. Brójo, "Performance of a turbofan engine with intercooling and regeneration," *World Acad. Sci. Eng. Technol.*, vol. 78, no. 6, pp. 359–363, 2011, doi: 10.5281/zenodo.1332144.

[15] C. Keerthana, D. Preethi, M. T. Anbarasan, M. Tech, and M. N. Vairamuthu, "Design and Analysis of a Combustion Chamber in a Gas Turbine," 2019. Accessed: Apr. 29, 2021. [Online]. Available: www.ijert.org

[16] P. Sravan Kumar and P. P. Rao, "Design and Analysis of Gas Turbine Combustion Chamber," *Int. J. Comput. Eng. Res.*, vol. 03, no. 1, pp. 444–447, 2013.

[17] R. Marudhappan, U. Chandrasekhar, and K. H. Reddy, "No Reaction Flow Analysis of Aero-Derivative Annular Combustor of a Turbo-Shaft Engine," *Int. J. Adv. Res. Eng. Technol. (IJARET*, vol. 9, no. 4, pp. 102–112, 2018, Accessed: May 12, 2021. [Online]. Available: http://www.iaeme.com/IJARET/index.asp102

[18] P. Jiang and X. He, "Ignition characteristics of a novel mixed-flow trapped vortex combustor for turboshaft engine," *Fuel*, vol. 261, p. 116430, Feb. 2020, doi: 10.1016/j.fuel.2019.116430.

[19] M. J. Kroes and T. W. Wild, *Aircraft powerplants*, 8th ed. McGraw-Hill Education Pvt Limited, 1994.

[20] B. Nkoi, P. Pilidis, and T. Nikolaidis, "Performance assessment of simple and modified cycle turboshaft gas turbines," *Propuls. Power Res.*, vol. 2, no. 2,

© Central University of Technology, Free State

pp. 96–106, 2013, doi: 10.1016/j.jppr.2013.04.009.

[21] L. S. Langston, “Turbines, Gas,” in *Reference Module in Earth Systems and Environmental Sciences*, Elsevier, 2014. doi: 10.1016/b978-0-12-409548-9.09044-8.

[22] T. D. Eastop and A. McConkey, *Applied Thermodynamics: For Engineering Technologists*, 5th ed., vol. 18, no. 3. Essex: Pearson, 1993. doi: 10.1080/03043799308923249.

[23] B. K. Hodge and R. P. Taylor, *Analysis and design of energy systems*, 3rd ed. Prentice Hall, 1999. [Online]. Available: https://www.osti.gov/biblio/6625781

[24] J. Moon, Y. H. Jeong, and Y. Addad, “Design of air-cooled waste heat removal system with string type direct contact heat exchanger and investigation of oil film instability,” *Nucl. Eng. Technol.*, vol. 52, no. 4, pp. 734–741, 2020, doi: 10.1016/j.net.2019.10.010.

[25] R. Ronquillo, “Understanding Heat Exchangers - Types, Designs, Applications and Selection Guide,” Thomasnet.Com. Accessed: Apr. 07, 2021. [Online]. Available: https://www.thomasnet.com/articles/process-equipment/understanding-heat-exchangers/

[26] R. A. Parisher and R. A. Rhea, “Chapter 6 - Mechanical Equipment,” in *Pipe Drafting and Design (Fourth Edition)*, Fourth Edi., R. A. Parisher and R. A. Rhea, Eds., Boston: Gulf Professional Publishing, 2022, pp. 119–153. doi: https://doi.org/10.1016/B978-0-12-822047-4.00011-X.

[27] F-Chart Software, “Compact Heat Exchanger: Basic Information.” Accessed: May 08, 2022. [Online]. Available: http://fchart.com/ees/heat_transfer_library/compact_hx/hs100.htm

[28] B. Nkoi, P. Pilidis, and T. Nikolaidis, “Performance of small-scale aero-derivative industrial gas turbines derived from helicopter engines,” *Propuls. Power Res.*, vol. 2, no. 4, pp. 243–253, Dec. 2013, doi: 10.1016/j.jppr.2013.11.001.

[29] C. Zhang and V. Gümmer, “High temperature heat exchangers for recuperated rotorcraft powerplants,” *Appl. Therm. Eng.*, vol. 154, pp. 548–

© Central University of Technology, Free State

561, May 2019, doi: 10.1016/J.APPLTHERMALENG.2019.03.119.

[30] J. H. Horlock, *Advanced gas turbine cycles: a brief review of power generation thermodynamics*, 1st ed. Elsevier, 2013.

[31] J. Jiang *et al.*, “Performance evaluation of supercritical CO2 Brayton cycle with two-stage compression and intercooling,” *Case Stud. Therm. Eng.*, vol. 64, p. 105503, Dec. 2024, doi: 10.1016/J.CSITE.2024.105503.

[32] T. Nada, “Performance characterization of different configurations of gas turbine engines,” *Propuls. Power Res.*, vol. 3, no. 3, pp. 121–132, 2014, doi: https://doi.org/10.1016/j.jppr.2014.07.005.

[33] G. B. Ariemma, G. Langella, P. Sabia, G. Sorrentino, M. de Joannon, and R. Ragucci, “Combustion stage configurations for intercooled regenerative reheat gas turbine systems,” *Appl. Therm. Eng.*, vol. 246, p. 122942, 2024, doi: https://doi.org/10.1016/j.applthermaleng.2024.122942.

[34] W. M. Kays and A. L. London, *Compact Heat Exchangers*, 3rd ed. Stanford: Scientific International, 2018.

[35] R. K. Shah and D. P. Sekulic, *Fundamentals of Heat Exchanger Design*, 1st ed. New Jersey: JOHN WILEY & SONS, INC., 2003.

[36] Y. A. Çengel and J. M. Cimbala, *Fluid Mechanics: Fundamentals and Applications*, 4rd ed. New York: McGraw-Hill Education, 2024.

[37] A. A. Sánchez-Escalona, E. Góngora-Leyva, and Y. Camaraza-Medina, “Monoethanolamine heat exchangers modeling using the Buckingham Pi theorem,” *Math. Model. Eng. Probl.*, vol. 6, no. 2, pp. 197–202, 2019, doi: 10.18280/mmep.060207.

[38] B. E. Anderson, G. Chen, and D. R. Blake, “Hydrocarbon emissions from a modern commercial airliner,” *Atmos. Environ.*, vol. 40, no. 19, pp. 3601–3612, Jun. 2006, doi: 10.1016/J.ATMOSENV.2005.09.072.

[39] D. J. Sutkus, S. L. Baughcum, and D. P. DuBois, “Scheduled civil aircraft emission inventories for 1999: Database development and analysis,” *NASA Contract. Rep. - NAS 1.26 211216*, 2001.

[40] M. Masiol and R. M. Harrison, “Aircraft engine exhaust emissions and other

© Central University of Technology, Free State

airport-related contributions to ambient air pollution: A review," *Atmos. Environ.*, vol. 95, pp. 409–455, Oct. 2014, doi: 10.1016/j.atmosenv.2014.05.070.

[41] ASTM, "Global Leader in Additive Manufacturing Standards," 2017. Accessed: Apr. 09, 2021. [Online]. Available: www.astm.org

[42] Gokhare Vinod G., Raut D. N., and Shinde D. K., "A Review paper on 3D-Printing Aspects and Various Processes Used in the 3D-Printing ," *Int. J. Eng. Res. Technol.*, 2017.

[43] A. Oluwajobi, "Development of a Low-Cost Fused Filament Fabrication (FFF) 3-D Desktop Printer," *Niger. J. Mater. Sci. Eng.*, vol. 10(2), no. March, pp. 81–90, 2021.

[44] X. Zhang, G. Xiong, Z. Shen, Y. Zhao, C. Guo, and X. Dong, "A GPU-based parallel slicer for 3D printing," in *IEEE International Conference on Automation Science and Engineering*, 2017, pp. 55–60. doi: 10.1109/COASE.2017.8256075.

[45] M. Palmer and J. Laliberte, "Effects of non-planar slicing techniques and carbon fibre material additives on the mechanical properties of 3D-printed drone propellers," *Drone Syst. Appl.*, vol. 11, pp. 1–11, Aug. 2023, doi: 10.1139/DSA-2023-0007.

[46] J. McPherson and W. Zhou, "A chunk-based slicer for cooperative 3D printing," *Rapid Prototyp. J.*, vol. 24, no. 9, pp. 1436–1446, 2018, doi: 10.1108/RPJ-07-2017-0150.

[47] K. V. Wong and A. Hernandez, "A Review of Additive Manufacturing," *ISRN Mech. Eng.*, vol. 2012, pp. 1–10, 2012, doi: 10.5402/2012/208760.

[48] C. Industrial, "Design guidelines for Direct Metal Laser Sintering (DMLS)," 2014. [Online]. Available: www.crucibledesign.co.uk%2Fimages%2Fuploaded%2Fguides%2Fbs7000-part-2-a-management-guide-download-original.pdf

[49] D. Manfredi *et al.*, "Direct Metal Laser Sintering: An additive manufacturing technology ready to produce lightweight structural parts for robotic applications," *Metall. Ital.*, vol. 105, no. 10, pp. 15–24, 2013.

© Central University of Technology, Free State

[50] Loughborough University, “Powder Bed Fusion.” Accessed: Jan. 15, 2025. [Online]. Available: https://www.lboro.ac.uk/research/amrg/about/the7categoriesofadditivemanufacturing/powderbedfusion/

[51] P. D. Anderson, L. C. A. Van Breemen, P. Hejmady, and R. Cardinaels, “Selective laser sintering of polymer particles,” 2020. Accessed: Apr. 01, 2021. [Online]. Available: https://www.researchgate.net/publication/345175895_Selective_laser_sintering_of_polymer_particles

[52] R. Singh, S. Singh, and M. S. J. Hashmi, “Implant Materials and Their Processing Technologies,” *Ref. Modul. Mater. Sci. Mater. Eng.*, Jan. 2016, doi: 10.1016/b978-0-12-803581-8.04156-4.

[53] M. Ashraf, I. Gibson, M. G. Rashed, and M. G. Rashed, “CHALLENGES AND PROSPECTS OF 3D PRINTING IN STRUCTURAL ENGINEERING,” in *13th International Conference on Steel, Space and Composite Structures*, 2018, pp. 1–10. [Online]. Available: https://www.researchgate.net/publication/320943125

[54] A. P. S. V. R. Subrahmanyam, P. S. Rao, and K. S. Prasad, “Critical Review on Chracterization of DMLS Materials,” *J. Xi’an Univ. Archit. Technol.*, vol. XII, no. IV, pp. 665–668, 2020.

[55] P. Hanzl, M. Zetek, T. Bakša, and T. Kroupa, “The influence of processing parameters on the mechanical properties of SLM parts,” in *Procedia Engineering*, Elsevier Ltd, Jan. 2015, pp. 1405–1413. doi: 10.1016/j.proeng.2015.01.510.

[56] A. Patterson, S. Messimer, and P. Farrington, “Overhanging Features and the SLM/DMLS Residual Stresses Problem: Review and Future Research Need,” 2017. doi: 10.20944/preprints201703.0202.v1.

[57] J. T. Black and R. A. Kohser, *DeGarmo’s Materials and Processes in Manufacturing*. Wiley, 1967.

[58] L. Mugwagwa, “Investigation and management of residual stresses in selective laser melting of maraging steel,” 2019. Accessed: Apr. 11, 2021.

© Central University of Technology, Free State

[Online]. Available: https://scholar.sun.ac.za

[59] EOS GmbH, “PA 2200 Balance,” Electro Optical Systems, 2024. Accessed: May 22, 2024. [Online]. Available: https://www.eos.info/en-us/polymer-solutions/polymer-materials/data-sheets/mds-pa-2200-balance?topdf

[60] J. Everaerts, E. Salvati, F. Uzun, L. Romano Brandt, H. Zhang, and A. M. Korsunsky, “Separating macro- (Type I) and micro- (Type II+III) residual stresses by ring-core FIB-DIC milling and eigenstrain modelling of a plastically bent titanium alloy bar,” *Acta Mater.*, vol. 156, pp. 43–51, 2018, doi: 10.1016/j.actamat.2018.06.035.

[61] I. S. Kim *et al.*, “Accelerating globularization in additively manufactured Ti-6Al-4V by exploiting martensitic laths,” *J. Mater. Res. Technol.*, vol. 12, pp. 304–315, 2021, doi: 10.1016/j.jmrt.2021.02.088.

[62] T. Lee, D. S. Shih, Y. Lee, and C. S. Lee, “Manufacturing ultrafine-grained Ti-6Al-4V bulk rod using multi-pass caliber-rolling,” *Metals (Basel).*, vol. 5, no. 2, pp. 777–789, 2015, doi: 10.3390/met5020777.

[63] J. Li, F. Cao, W. Hou, and Y. Shen, “Self-consumption friction plug spot welding of Ti–6Al–4V plates,” *J. Mater. Res. Technol.*, vol. 9, no. 6, pp. 14283–14293, 2020, doi: 10.1016/j.jmrt.2020.10.029.

[64] EOS GmbH, “EOS Titanium Ti64 - Material data sheet,” 2022, *Electro Optical Systems EOS*. [Online]. Available: https://uk.eos.info/03_system-related-assets/material-related-contents/metal-materials-and-examples/metal-material-datasheet/titan/ti64/material_datasheet_eos_titanium_ti64_grade23_premium_en_web.pdf

[65] S. Cao, Y. Zou, C. V. S. Lim, and X. Wu, “Review of laser powder bed fusion (LPBF) fabricated Ti-6Al-4V: process, post-process treatment, microstructure, and property,” *Light Adv. Manuf.*, vol. 2, no. 3, pp. 313–332, 2021, doi: 10.37188/lam.2021.020.

[66] H. Khalid Rafi., N. V. Karthik, T. L. Starr, and B. E. Stucker, “Mechanical property evaluation of Ti-6Al-4V parts made using Electron Beam Melting,” 2012.

© Central University of Technology, Free State

[67] S. Venter and G. Jacobs, “Development and characterisation of Ti-6Al-4V additively manufactured compact counter-flow heat exchangers,” in *2024 RAPDASA-RobMech-PRASA-AMI Conference*, 2024. doi: https://doi.org/10.1051/matecconf/202440601003.

[68] Robinson Helicopter Company, “R66 Turbine.” Accessed: Jan. 16, 2025. [Online]. Available: https://www.robinsonheli.com/api/files/791/r66-turbine-brochure.pdf

[69] Robinson, “Robinson Model R66: Section 2 - Limitations,” 2016. Accessed: May 06, 2021. [Online]. Available: https://robinsonheli.com/wp-content/uploads/2020/04/r66-poh-2.pdf

[70] Rapid Air Movement, “Mixed-Flow.” Accessed: Jan. 16, 2025. [Online]. Available: https://rapidairmovement.co.uk/products/mixed-flow/

© Central University of Technology, Free State

APPENDIX 1

Heat Exchanger Calculations

7.4 Inlet conditions

Table 17: Full-size, inlet conditions

	Hot side	Cold side	Units
m	0.819	0.157	kg/s
P	628.215	140	kPa
Ti	522.860	298	K

7.5 Full-size configuration

Table 18: Full-size, configuration

	Hot side	Cold side	Units
b	12	12	mm
l_f	13	13	mm
Dh	6.643E-3	6.643E-3	m
B	616.8	616.8	
δ_fin	0.8	0.8	mm
Af/A	0.719	0.719	

7.6 Full-size calculations

Table 19: Full-size, Pass 1

	Iteration 1	Iteration 2	Iteration 3	Units
ε	0.4	0.303	0.302	
δ_plate	2.000E-3	2.000E-3	2.000E-3	m
kf	7.47	7.47	7.47	W/mK
L1	90.00E-3	90.00E-3	90.00E-3	m
L2	220.00E-3	220.00E-3	220.00E-3	m
L3	220.00E-3	220.00E-3	220.00E-3	m
Np	8	8	8	
A_fr_h	48.400E-3	48.400E-3	48.400E-3	m^2
A_fr_c	19.800E-3	19.800E-3	19.800E-3	m^2
V_fr_h	1.901E-3	1.901E-3	1.901E-3	m^3

© Central University of Technology, Free State

V_fr_c	2.138E-3	2.138E-3	2.138E-3	m^3
A_h	1.17241	1.172	1.172	m^2
A_c	1.31897	1.319	1.319	m^2
A_o_h	17.112E-3	17.112E-3	17.112E-3	m^2
A_o_c	7.875E-3	7.875E-3	7.875E-3	m^2
σ_h	353.554E-3	353.554E-3	353.554E-3	
σ_c	397.727E-3	397.727E-3	397.727E-3	
T_h_o	504.04388	508.607	508.654	K
T_c_o	387.94400	366.133	365.908	K
T_h_m	513.45194	515.733	515.757	K
T_c_m	342.97200	332.066	331.954	K
μ_h	27.186E-6	27.267E-6	27.268E-6	Pa * s
μ_c	20.428E-6	19.929E-6	19.924E-6	Pa * s
Cp_h	1.0321E+0	1.0326E+0	1.0326E+0	kJ/kg*K
Cp_c	1.0085E+0	1.0078E+0	1.0078E+0	kJ/kg*K
Pr_h	680.000E-3	680.000E-3	680.000E-3	
Pr_c	698.546E-3	700.945E-3	700.970E-3	
Pr^2/3_h	0.773	0.773	0.773	
Pr^2/3_c	0.787	0.789	0.789	
G_h	47.861	47.861	47.861	kg/m^2*s
G_c	21.757	21.757	21.757	kg/m^2*s
Re_h	11694.964	11660.324	11659.968	
Re_c	7074.915	7252.076	7253.949	
j_h	0.0037	0.0037	0.0037	
j_c	0.0040	0.0040	0.0040	
h_h	236.359	233.265	233.266	W/m^2*K
h_c	111.484	111.150	111.147	W/m^2*K

© Central University of Technology, Free State

m_h	289.777	287.874	287.874	m^-1
m_c	199.014	198.716	198.713	m^-1
l_h	6.500E-3	6.500E-3	6.500E-3	m
l_c	6.500E-3	6.500E-3	6.500E-3	m
nf_h	0.507	0.510	0.510	
nf_c	0.665	0.665	0.665	
no_h	0.645	0.647	0.647	
no_c	0.759	0.759	0.759	
A_wall	356.400E-3	356.400E-3	356.400E-3	m^2
R_wall	751.228E-6	751.228E-6	751.228E-6	K/W
UA	65.353	65.019	65.018	W/K
C_h	845.298	845.660	845.664	W/K
C_c	172.796	172.673	172.671	W/K
Cr	0.204	0.204	0.204	
NTU	0.378	0.377	0.377	
ε_actual	0.303	0.302	0.302	
q	11.765E+3	11.715E+3	11.715E+3	W
T_h_o_real	508.942	509.006	509.007	K
T_c_o_real	366.085	365.848	365.848	K

Table 20: Full-size, Pass 2

	Iteration 1	**Iteration 2**	**Iteration 3**	**Units**
ε	0.3	0.304	0.304	
δ_plate	2.000E-3	2.000E-3	2.000E-3	m
kf	7.47	7.47	7.47	W/mK
L1	90.00E-3	90.00E-3	90.00E-3	m
L2	220.00E-3	220.00E-3	220.00E-3	m
L3	220.00E-3	220.00E-3	220.00E-3	m

© Central University of Technology, Free State

Np	8	8	8	
A_fr_h	48.40E-3	48.40E-3	48.40E-3	m^2
A_fr_c	19.80E-3	19.80E-3	19.80E-3	m^2
V_fr_h	1.90E-3	1.90E-3	1.90E-3	m^3
V_fr_c	2.14E-3	2.14E-3	2.14E-3	m^3
A_h	1.172	1.172	1.172	m^2
A_c	1.319	1.319	1.319	m^2
A_o_h	17.11E-3	17.11E-3	17.11E-3	m^2
A_o_c	7.88E-3	7.88E-3	7.88E-3	m^2
σ_h	0.354	0.354	0.354	
σ_c	0.398	0.398	0.398	
T_h_o	500.02199	499.902	499.902	K
T_c_o	408.79540	409.368	409.368	K
T_h_m	504.514	504.454	504.454	K
T_c_m	387.322	387.608	387.608	K
μ_h	26.870E-6	26.868E-6	26.868E-6	Pa * s
μ_c	22.325E-6	22.337E-6	22.337E-6	Pa * s
Cp_h	1.0304	1.0304	1.0304	kJ/kg*K
Cp_c	1.0127	1.0128	1.0128	kJ/kg*K
Pr_h	680.000E-3	680.000E-3	680.000E-3	
Pr_c	691.029E-3	690.983E-3	690.983E-3	
Pr^2/3_h	0.773	0.773	0.773	
Pr^2/3_c	0.782	0.782	0.782	
G_h	47.861	47.861	47.861	kg/m^2*s
G_c	21.757	21.757	21.757	kg/m^2*s
Re_h	11832.673	11833.607	11833.607	
Re_c	6473.880	6470.378	6470.378	
j_h	0.0036	0.0036	0.0036	

© Central University of Technology, Free State

j_c	0.0041	0.0041	0.0041	
h_h	229.584	229.582	229.582	W/m^2*K
h_c	115.577	115.586	115.586	W/m^2*K
m_h	285.594	285.592	285.592	m^-1
m_c	202.635	202.642	202.642	m^-1
l_h	6.500E-3	6.500E-3	6.500E-3	m
l_c	6.500E-3	6.500E-3	6.500E-3	m
nf_h	0.513	0.513	0.513	
nf_c	0.658	0.658	0.658	
no_h	0.650	0.650	0.650	
no_c	0.754	0.754	0.754	
A_wall	356.400E-3	356.400E-3	356.400E-3	m^2
R_wall	751.228E-6	751.228E-6	751.228E-6	K/W
UA	65.916	65.918	65.918	W/K
C_h	843.878	843.868	843.868	W/K
C_c	173.515	173.520	173.520	W/K
Cr	0.206	0.206	0.206	
NTU	0.380	0.380	0.380	
ε_actual	0.304	0.304	0.304	
q	7.546E+3	7.546E+3	7.546E+3	W
T_h_o_real	500.064	500.064	500.064	K
T_c_o_real	409.338	409.338	409.338	K

Table 21: Full-size, Pass 3

	Iteration 1	**Iteration 2**	**Iteration 3**	**Units**
ε	0.3	0.306	0.306	

© Central University of Technology, Free State

δ_plate	2.000E-3	2.000E-3	2.000E-3	m
kf	7.47	7.47	7.47	W/mK
L1	90.00E-3	90.00E-3	90.00E-3	m
L2	220.00E-3	220.00E-3	220.00E-3	m
L3	220.00E-3	220.00E-3	220.00E-3	m
Np	8	8	8	
A_fr_h	48.40E-3	48.40E-3	48.40E-3	m^2
A_fr_c	19.80E-3	19.80E-3	19.80E-3	m^2
V_fr_h	1.90E-3	1.90E-3	1.90E-3	m^3
V_fr_c	2.14E-3	2.14E-3	2.14E-3	m^3
A_h	1.172	1.172	1.172	m^2
A_c	1.319	1.319	1.319	m^2
A_o_h	17.11E-3	17.11E-3	17.11E-3	m^2
A_o_c	7.88E-3	7.88E-3	7.88E-3	m^2
σ_h	0.354	0.354	0.354	
σ_c	0.398	0.398	0.398	
T_h_o	494.36996	494.256	494.256	K
T_c_o	436.55600	437.100	437.100	K
T_h_m	497.217	497.160	497.160	K
T_c_m	422.947	423.219	423.219	K
μ_h	26.606E-6	26.604E-6	26.604E-6	Pa * s
μ_c	23.769E-6	23.779E-6	23.779E-6	Pa * s
Cp_h	1.0290	1.0290	1.0290	kJ/kg*K
Cp_c	1.0171	1.0171	1.0171	kJ/kg*K
Pr_h	680.167E-3	680.170E-3	680.170E-3	
Pr_c	686.246E-3	686.214E-3	686.214E-3	
Pr^2/3_h	0.773	0.773	0.773	
Pr^2/3_c	0.778	0.778	0.778	
G_h	47.861	47.861	47.861	kg/m^2*s
G_c	21.757	21.757	21.757	kg/m^2*s

© Central University of Technology, Free State

Re_h	11950.036	11950.993	11950.993	
Re_c	6080.650	6077.893	6077.893	
j_h	0.0036	0.0036	0.0036	
j_c	0.0042	0.0042	0.0042	
h_h	229.242	229.239	229.239	W/m^2*K
h_c	119.456	119.464	119.464	W/m^2*K
m_h	285.381	285.379	285.379	m^-1
m_c	206.007	206.013	206.013	m^-1
l_h	6.500E-3	6.500E-3	6.500E-3	m
l_c	6.500E-3	6.500E-3	6.500E-3	m
nf_h	0.513	0.513	0.513	
nf_c	0.651	0.651	0.651	
no_h	0.650	0.650	0.650	
no_c	0.749	0.749	0.749	
A_wall	356.400E-3	356.400E-3	356.400E-3	m^2
R_wall	751.228E-6	751.228E-6	751.228E-6	K/W
UA	66.893	66.894	66.894	W/K
C_h	842.759	842.751	842.751	W/K
C_c	174.259	174.265	174.265	W/K
Cr	0.207	0.207	0.207	
NTU	0.384	0.384	0.384	
ε_actual	0.306	0.306	0.306	
q	4.842E+3	4.842E+3	4.842E+3	W
T_h_o_real	494.319	494.318	494.318	K
T_c_o_real	437.124	437.124	437.124	K

© Central University of Technology, Free State

Table 22: Full-size, pressure drop analysis

	Hot side	Cold Pass 1	Cold Pass 2	Cold Pass 3	Units
f	7.500E-3	8.500E-3	8.500E-3	8.500E-3	
D_h	6.643E-3	6.643E-3	6.643E-3	6.643E-3	m
G	47.861	21.757	21.757	21.757	kg/m^2*s
l	0.270	0.220	0.220	0.220	m
k_c	0.490	0.500	0.500	0.500	
k_e	0.350	0.460	0.460	0.460	
T_i	522.860	298.000	365.848	409.338	K
T_o	494.318	365.848	409.338	437.124	K
T_m	508.589	331.924	387.593	423.231	K
P_i	628.215	110.000	109.525	108.992	kPa
ρ_i	4.186	1.286	1.043	0.928	kg/m^3
ρ_o	4.428	1.047	0.932	0.869	kg/m^3
ρ_m	4.303	1.155	0.984	0.897	kg/m^3
σ	0.354	0.398	0.398	0.398	
ΔP	532.346	475.309	532.206	570	Pa

© Central University of Technology, Free State

7.7 Single-passage inlet conditions

Table 23: Full-size, inlet conditions

	Hot side	Cold side	Units
m	0.819	0.157	kg/s
P	628.215	140	kPa
Ti	522.860	298	K

7.8 Single-passage configuration

Table 24: Single-passage, full-size configuration

	Hot side	Cold side	Units
b	12	12	mm
l_f	13	13	mm
Dh	6.643E-3	6.643E-3	m
B	616.8	616.8	
δ_fin	0.8	0.8	mm
Af/A	0.719	0.719	

7.9 Single-passage calculations

Table 25: Single-passage, Pass 1

	Iteration 1	Iteration 2	Iteration 3	Units:
ε	0.3	0.341	0.342	
δ_plate	2.000E-3	2.000E-3	2.000E-3	m
kf	7.47	7.47	7.47	W/m*K
L1	90.00E-3	90.00E-3	90.00E-3	m
L2	220.00E-3	220.00E-3	220.00E-3	m
L3	27.50E-3	27.50E-3	27.50E-3	m
Np	1	1	1	
A_fr_h	6.050E-3	6.050E-3	6.050E-3	m^2
A_fr_c	2.475E-3	2.475E-3	2.475E-3	m^2
V_fr_h	237.600E-6	237.600E-6	237.600E-6	m^3
V_fr_c	475.200E-6	475.200E-6	475.200E-6	m^3
A_h	146.552E-3	146.552E-3	146.552E-3	m^2
A_c	293.103E-3	293.103E-3	293.103E-3	m^2

© Central University of Technology, Free State

A_o_h	2.139E-3	2.139E-3	2.139E-3	m^2
A_o_c	1.750E-3	1.750E-3	1.750E-3	m^2
σ_h	353.554E-3	353.554E-3	353.554E-3	
σ_c	707.071E-3	707.071E-3	707.071E-3	
T_h_o	508.74791	506.819	506.772	K
T_c_o	365.45800	374.677	374.902	K
T_h_m	515.80395	514.840	514.816	K
T_c_m	331.72900	336.339	336.451	K
μ_h	27.27E-6	27.24E-6	27.23E-6	Pa * s
μ_c	19.91E-6	20.12E-6	20.13E-6	Pa * s
Cp_h	1.0326	1.0324	1.0324	kJ/kg*K
Cp_c	1.0078	1.0081	1.0081	kJ/kg*K
Pr_h	0.68	0.68	0.68	
Pr_c	0.70	0.70	0.70	
Pr^2/3_h	0.773	0.773	0.773	
Pr^2/3_c	0.789	0.788	0.788	
G_h	47.861	47.861	47.861	kg/m^2*s
G_c	12.238	12.238	12.238	kg/m^2*s
Re_h	11659.256	11673.870	11674.227	
Re_c	4082.454	4039.665	4038.632	
j_h	0.0036	0.0036	0.0036	
j_c	0.0048	0.0048	0.0048	
h_h	230.072	230.031	230.030	W/m^2*K
h_c	74.238	75.114	75.117	W/m^2*K
m_h	285.897	285.871	285.871	m^-1
m_c	162.402	163.358	163.360	m^-1
l_h	6.500E-3	6.500E-3	6.500E-3	m
l_c	6.500E-3	6.500E-3	6.500E-3	m

© Central University of Technology, Free State

nf_h	0.513	0.513	0.513	
nf_c	0.743	0.741	0.741	
no_h	0.650	0.650	0.650	
no_c	0.815	0.813	0.813	
Awall	0.079	0.079	0.079	m^2
Rwall	3.381E-3	3.381E-3	3.381E-3	K/W
UA	9.485	9.534	9.535	W/K
C_h	105.709	105.690	105.689	W/K
C_c	21.584	21.590	21.590	W/K
Cr	0.204	0.204	0.204	
NTU	0.439	0.442	0.442	
ε_actual	0.341	0.342	0.342	
q	1.654E+3	1.660E+3	1.661E+3	W
T_h_o_real	507.216	507.149	507.149	K
T_c_o_real	374.620	374.910	374.910	K
ΔT_h	15.644	15.711	15.711	K
ΔT_c	76.620	76.910	76.910	K

Table 26: Full-size pressure drop analysis

	Hot side	**Cold Pass 3**	**Units**
f	7.500E-3	8.500E-3	
D_h	6.643E-3	6.643E-3	m
G	47.861	12.238	kg/m^2*s
l	0.090	0.220	m
k_c	0.490	0.500	
k_e	0.350	0.460	
T_i	522.860	298.000	K
T_o	507.149	374.910	K

© Central University of Technology, Free State

T_m	515.004	336.455	K
P_i	628.215	110.000	kPa
ρ_i	4.186	1.286	kg/m^3
ρ_o	4.315	1.022	kg/m^3
ρ_m	4.250	1.139	kg/m^3
σ	0.354	0.707	
ΔP	327.259	159.390	Pa

© Central University of Technology, Free State

APPENDIX 2

Supporting Documents

Table 27: Properties of air at atmospheric pressure [7]

Table A-5 | Properties of air at atmospheric pressure.†

The values of μ, k, c_p, and Pr are not strongly pressure-dependent and may be used over a fairly wide range of pressures							
T, K	ρ kg/m^3	c_p kJ/kg · °C	$\mu \times 10^5$ kg/m· s	$\nu \times 10^6$ m^2/s	k W/m · °C	$\alpha \times 10^4$ m^2/s	Pr
100	3.6010	1.0266	0.6924	1.923	0.009246	0.02501	0.770
150	2.3675	1.0099	1.0283	4.343	0.013735	0.05745	0.753
200	1.7684	1.0061	1.3289	7.490	0.01809	0.10165	0.739
250	1.4128	1.0053	1.5990	11.31	0.02227	0.15675	0.722
300	1.1774	1.0057	1.8462	15.69	0.02624	0.22160	0.708
350	0.9980	1.0090	2.075	20.76	0.03003	0.2983	0.697
400	0.8826	1.0140	2.286	25.90	0.03365	0.3760	0.689
450	0.7833	1.0207	2.484	31.71	0.03707	0.4222	0.683
500	0.7048	1.0295	2.671	37.90	0.04038	0.5564	0.680
550	0.6423	1.0392	2.848	44.34	0.04360	0.6532	0.680
600	0.5879	1.0551	3.018	51.34	0.04659	0.7512	0.680
650	0.5430	1.0635	3.177	58.51	0.04953	0.8578	0.682
700	0.5030	1.0752	3.332	66.25	0.05230	0.9672	0.684
750	0.4709	1.0856	3.481	73.91	0.05509	1.0774	0.686
800	0.4405	1.0978	3.625	82.29	0.05779	1.1951	0.689
850	0.4149	1.1095	3.765	90.75	0.06028	1.3097	0.692
900	0.3925	1.1212	3.899	99.3	0.06279	1.4271	0.696
950	0.3716	1.1321	4.023	108.2	0.06525	1.5510	0.699
1000	0.3524	1.1417	4.152	117.8	0.06752	1.6779	0.702
1100	0.3204	1.160	4.44	138.6	0.0732	1.969	0.704
1200	0.2947	1.179	4.69	159.1	0.0782	2.251	0.707
1300	0.2707	1.197	4.93	182.1	0.0837	2.583	0.705
1400	0.2515	1.214	5.17	205.5	0.0891	2.920	0.705
1500	0.2355	1.230	5.40	229.1	0.0946	3.262	0.705
1600	0.2211	1.248	5.63	254.5	0.100	3.609	0.705
1700	0.2082	1.267	5.85	280.5	0.105	3.977	0.705
1800	0.1970	1.287	6.07	308.1	0.111	4.379	0.704
1900	0.1858	1.309	6.29	338.5	0.117	4.811	0.704
2000	0.1762	1.338	6.50	369.0	0.124	5.260	0.702
2100	0.1682	1.372	6.72	399.6	0.131	5.715	0.700
2200	0.1602	1.419	6.93	432.6	0.139	6.120	0.707
2300	0.1538	1.482	7.14	464.0	0.149	6.540	0.710
2400	0.1458	1.574	7.35	504.0	0.161	7.020	0.718
2500	0.1394	1.688	7.57	543.5	0.175	7.441	0.730

© Central University of Technology, Free State